Florian Pixner, BSc

Rotary Friction Welding (RFW) of Molybdenum

MASTER'S THESIS

to achieve the university degree of

Diplom-Ingenieur

Master's degree programme: Mechanical Engineering and Business Economics

submitted to

Graz University of Technology

Supervisor

Assoc.Prof. Dipl.-Ing. Dr.techn. Norbert Enzinger
Dipl.-Ing. Markus Stütz

Institute of Materials Science, Joining and Forming

Graz, May 2018

AFFIDAVIT

I declare that I have authored this thesis independently, that I have not used other than the declared sources/resources, and that I have explicitly indicated all material which has been quoted either literally or by content from the sources used. The text document uploaded to TUGRAZonline is identical to the present master‘s thesis dissertation.

Date

Signature

Ich weiß, dass ich nichts weiß

— Sokrates

Abstract

Molybdenum belongs to the group of refractory metals and is characterized by its high melting point of 2623 °C. As a result, common arc welding technologies are not feasible anymore and do not deliver satisfying results. Solid state welding technologies offer an interesting alternative and produce bonding at temperatures essentially below the melting point. Latest studies have shown that rotary friction welding of commercially pure molybdenum is challenging and providing a sufficient drive power, extensive plastic deformation and rapid upset rates are only selected challenges to deal with. A further study for a better understanding of the behavior, especially the plasticization process of molybdenum and its alloys during friction welding is required to develop a stable and capable general process design.

In this work, rotary friction welding is performed in commercially pure molybdenum, the carbide stabilized molybdenum alloy Titanium-Zirconium-Molybdenum and a reference low-carbon steel by the means of a friction stir welding device providing comprehensive parameter recording. Molybdenum and Titanium-Zirconium-Molybdenum reveal a completely different plasticization behavior compared to the reference low-carbon steel. The molybdenum metals require a general re-design of the process in order to keep the plasticization behavior manageable and to generate sound joints. The evolved microstructure in the weld zone displays the for friction welding representative weld sections and the presence of an equiaxed, fine grained fully plasticized zone. The hardness profiles of the molybdenum metals reveal no major difference between the base material and the weld zone, only a slight increase in the fully plasticized zone for TZM is notable. The recorded typical thermal cycles during rotary friction welding reflect molybdenum's unique thermophysical properties. The specific heat capacity c and thermal conductivity λ determine the distribution of the formed transient temperature field and reveal the necessity of short process times to oppose the heat dissipation.

Kurzfassung

Molybdän zählt zu den Refraktärmetallen und zeichnet sich durch seinen hohen Schmelzpunkt von 2623 °C aus. Konventionelle Lichtbogenschweißverfahren sind nur bedingt geeignet und liefern keine zufriedenstellenden Ergebnisse. Festkörperschweißverfahren hingegen bieten eine interessante Alternative zu den etablierten Schmelzschweißverfahren und ermöglichen ein Fügen bei maximaler Temperatur unterhalb der Liquiduslinie. Aktuelle Veröffentlichungen zeigen zum einen ein sehr herausforderndes Materialverhalten von Molybdän beim Reibschweißen und zum anderen die Notwendigkeit einer hohen Maschinenleistung zur Aufrechterhaltung des Prozesses. Während des Schweißzyklus wurde eine starke Materialplastifizierung mit hohen Verkürzungsraten beobachtet. Für ein besseres Verständnis über das Materialverhalten von Molybdän beim Reibschweißen und um einen stabilen Prozess zu definieren, sind zusätzliche Untersuchungen erforderlich.

Im Zuge dieser Masterarbeit sind auf einer Reibrührschweißanlage die Materialen reines Molybdän, die Molybdänlegierung Titanium-Zirkonium-Molybdän und ein unlegierter Referenzstahl rotationsreibgeschweißt geworden. Es zeigte sich, dass die Molybdänmetalle ein gänzlich anderes Plastifizierungsverhalten aufweisen als der Referenzstahl. Die grundsätzliche Umgestaltung des Prozessdesigns war daher erforderlich, um das auftretende Verkürzungsverhalten zu kompensieren und um eine fehlerfreie Verschweißung zu erzielen. Die auftretende Mikrostruktur weist die für das Reibschweißen typische Zonen auf, inklusive einer gleichmäßigen und feinkörnigen, vollständig plastifizierten Zone. Die Härteverteilungen der Molybdänschweißungen zeigen keine große Abweichung vom unbeeinflussten Grundwerkstoff und der vollständig plastifizierten Zone. Es ist lediglich ein kleiner Härteanstieg in der vollständig plastifizierten Zone für TZM erkennbar. Die aufgezeichneten Temperaturzyklen während des Rotationsreibschweißens spiegeln die speziellen thermophysikalischen Eigenschaften von Molybdän wieder. Die spezifische Wärmekapazität c und die Wärmeleitfähigkeit λ von Molybdän bestimmen die Ausbreitung des instationären Temperaturfeldes und zeigen die absolute Notwendigkeit von kurzen Prozesszeiten, um der erhöhten Wärmeabfuhr entgegenzuwirken.

Contents

Abbreviations

ADM	Ammonium molybdate
c	Specific heat capacity [J/g K]
DBTT	Ductile-brittle transition temperature [K]
δ_x	Relative error
$\overline{\delta_x}$	Mean relative error
DDFW	Direct drive friction welding
DoE	Design of experiments
E	Energy input [J]
EB	Electron beam
EBW	Electron beam welding
η	Mechanical efficiency
FFD	Full factorial design
FSW	Friction stir welding
FW	Friction welding
FZ	Fusion zone
HAZ	Heat affected zone
HV	Hardness Vickers
IFW	Inertia friction welding
J	Joule
λ	Thermal conductivity [W/m K]
LCS	Low-carbon steel
LFW	Linear friction welding
MHC	Molybdenum-Hafnium-Carbon
ML	Molybdenum-Lanthanum oxide
mm	Millimeter
MY	Molybdenum-Yttrium-Cerium oxide
N	Newton
NC	Numerical control
ODS	Oxide dispersion strengthened
P	Power input [W]
Pa	Pascal
PM	Powder metallurgy
PSN	Particle stimulated nucleation

PWHT	Post weld heat treatment
RFW	Rotary friction welding
ρ	Density [g/cm^3]
rpm	Revolutions per minute
RT	Room temperature [K]
s	Second
SEM	Scanning electron microscope
SSW	Solid state welding
t	Time [s]
T	Temperature [K]
T_{load}	Torque loaded condition [Nm]
T_{unload}	Torque unloaded condition [Nm]
TEM	Transmission electron microscopy
TIG	Tungsten inert-gas welding
T_m	Melting temperature [K]
TMAZ	Thermomechanically affected zone
TZM	Titanium-Zirconium-Molybdenum
UTS	Ultimate tensile strength [MPa]
W	Watt
z	Upset [mm]
$\dot{z}$	Upset-rate [mm/s]

1 Introduction

The introduction of this thesis focuses on the background of the topic and leads to the issues behind this work. Moreover, the purpose and the objectives of this thesis are presented.

1.1 Motivation

Molybdenum belongs to the group of refractory metals, which are characterized by their high melting point. Molybdenum's melting point of 2623 °C, the embrittlement of the crystal caused by impurities, grain coarsening, and the tendency to form molybdenum(VI)-trioxide (MoO_3) at elevated temperature complicates fusion welding. Common arc welding technologies, e.g. tungsten inert gas (TIG) welding, do not deliver satisfying results. Solid state welding (SSW) technologies offer an interesting alternative and produce bonding at temperatures essentially below the melting point. In friction welding, the welded joint is generated by the combination of heat input obtained by the relative movement of the weld specimens and the simultaneously applied friction pressure.

Friction welding processes are significantly faster compared to more conventional welding methods. Rapid welding cycles linked with a concentrated heat input at the weld interface results in a narrow heat-affected zones (HAZ). More uniform properties, higher joint efficiencies, and stronger welds can be achieved. Further, the joint preparation for rotary friction welding requires a minimial machining effort, saw-cutted and even sheared surfaces are weldable. Friction welding also features a natural self-cleaning effect, this means that after starting plasticizing the initial surface-oxides and impurities are extruded into the flash and provide a clean metal-to-metal contact in the weld interface. From a methodological point of view, solid state welding techniques, including rotary frcition welding, seem suited for welding molybdenum and can overcome previously mentioned challenges.

The weldability of molybdenum, especially by electron beam (EB) and by tungsten inert gas (TIG) welding, has been studied in the past. However, industrial applications of friction welding of commercially pure molybdenum are so far not known and scientific research is limited in certain field. Therefore, the publicly co-funded project *JOIN Moly M1*, in co-operation with the industrial partners *Plansee SE*, *Raiser GmbH & Co KG* and *voestalpine Böhler Welding Austria GmbH*, was launched in September 2014 at the *Graz University of Technology*. The aim is to establish a fundamental understanding of the processes and to investigate the capability to generate integral structures from semi-finished molybdenum parts.

First, rotary friction welding attempts of commercially pure molybdenum, and for comparison low-carbon steel (LCS) with large cross-sections (4,400 mm^2) were carried out on a heavy-duty direct drive friction welding (DDFW) machine. The conducted welding attempts of molybdenum and low-carbon steel revealed a completly different

process- and plasticization behavior of the welded materials. For commercially pure molybdenum, a much more sudden and steeper increase of the upset in the friction phase (molybdenum 7.0 mm/s and low-carbon steel 0.1 mm/s), as well as an increased power demand were observed. The large plasticized zone, the fast upset-rate and the high power demand are the identified key challenges and complicate setting up a stable process design for rotary friction welding of molybdenum. A more basic study for a better understanding of the behavior, especially the plasticization process of molybdenum and its alloys during friction welding is required to further develop a stable and capable general process design.

1.2 Objectives

Basic direct drive friction welding trials, with adapted cross-sections and more accurate process control and monitoring will be performed under laboratory conditions at the institute's friction stir welding (FSW) machine. Feasible parameter configurations should be identified and a general process design should be established. Further, the recorded typical thermal cycles during rotary friction welding linked with the applied pressure levels should provide a better understanding of the complex relations between thermophysical-, thermomechanical properties and material softening during friction welding.

The objectives are summarized as follows:

1. Adjustment of the friction stir welding (FSW) machine and the experimental set-up for direct drive friction welding (DDFW)
2. Determination of input parameter configurations for RFW of molybdenum
3. Detailed knowledge about the influence of input parameter configurations on the output parameters (e.g. torque, upset, upset-rate, etc.)
4. Detailed knowledge about typical RFW thermal cycles of molybdenum
5. Comparison of the upset behavior of molybdenum and carbide stabilized Titanium-Zirconium-Molybdenum (TZM) to a low-carbon Steel (LCS)

2 State-of-the-Art

This chapter provides a basic theoretical background of the applied materials including its unique properties and the fundamentals of the rotary friction welding process.

2.1 Molybdenum and Molybdenum Based Alloys

Molybdenum has a body-centred cubic lattice and belongs to the group of refractory metals as for instance tungsten and niobium. It is characterized by its high interatomic bond, hence it possesses an excellent high-temperature strength, heat resistance, and a melting point of 2623 °C [1]. Further, molybdenum combines unique physical properties, e.g. high thermal conductivity and low coefficient of thermal-expansion, and is therefore widely applied in lighting technologies, high-performance electronics, high-temperature furnace constructions and as sputter targets for the coating technology [2, 3]. Due to molybdenum's high melting point and oxidation behavior, semi-finished parts of molybdenum are nowadays mainly produced by powder metallurgy (PM) (fig. 1) [4, 5]. A minimized amount of interstitial impurities in the raw material combined with continuous improvement of the powder metallurgic process leads to more uniform and improved properties [6].

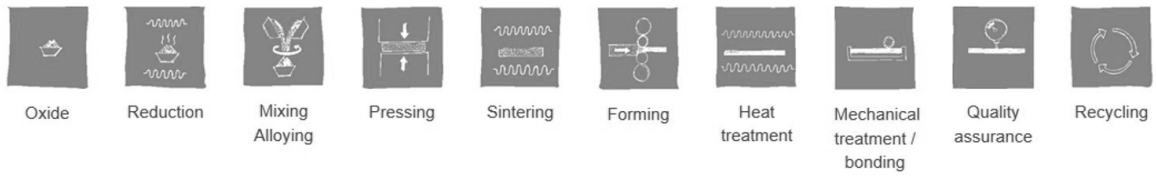

Figure 1: Process chain of powder metallurgy (PM) to produce semi-finshed molybdenum components [4]

The for the molybdenum powder production required molybdenum(IV)-sulphide (MoS_2) is extracted from the initial ore in a series of grinding and separation steps. The isolated material is roasted under atmospheric condition to gain molybdenum(VI)-trioxide (MoO_3) and the by-product sulphur(IV)-oxide (SO_2). MoO_3. The technical oxide, contains about 57% molybdenum and less than 0.1% sulphur. However, the technical oxide needs to be purified by further steps, e.g. by dissolvent in ammonium hydroxide and filtration/solvent extraction, to dispose it from its impurities. The received high-purity ammonium molybdate (ADM) is the starting material for molybdenum powder production and is heated up to high temperatures (calcination) for the production of a high-purity molybdenum(VI)-trioxide. A subsequent two staged hydrogen reduction of the purified MoO_3 (eq. 1 & 2) creates the pure molybdenum metal powder (>99.97 wt%) [2, 4, 5].

$$MoO_3 + H_2 \longrightarrow MoO_2 + H_2O \tag{1}$$

$$MoO_2 + 2\,H_2 \longrightarrow Mo + 2\,H_2O \tag{2}$$

With respect to the final material applications and the therefore required properties, e.g. recrystallization behavior, selected alloying elements are added. Beside commercially pure molybdenum, a wide variety of available molybdenum alloys exist, providing tailored properties. In general, they can be classified as substitutional solid solution-, carbide stabilized-, and oxide dispersion strengthened-alloys [7].

2.1.1 Strengthening Mechanisms of Molybdenum Based Alloys

Solid solution strengthening is an applied method to improve the mechanical properties of molybdenum [8]. Substitutional solid solution is formed (fig. 2b) by adding additional alloying elements (e.g. rhenium) to the crystalline lattice of the solvent. Some alloying elements are only soluble in small amounts, whereas molybdenum in combination with some other solutes (e.g. tungsten), a continuous solid solution at all temperatures and concentrations form (fig. 2a) [9].

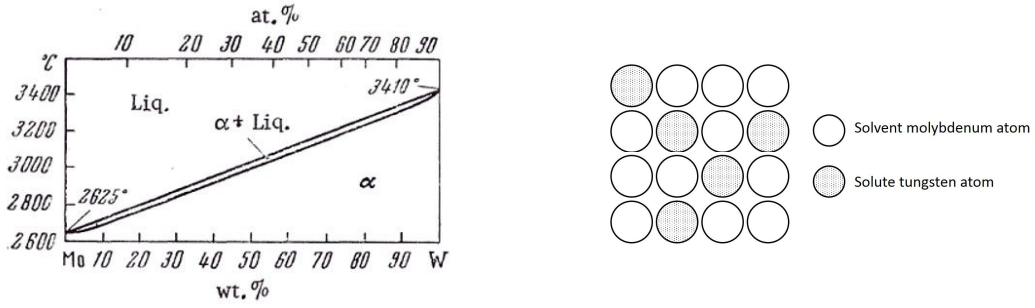

(a) (b)

Figure 2: (a) Equilibrium phase diagram molybdenum-tungsten [1] and (b) schematic illustration disordered substitutional solid solution

Considering the Hume-Rothery rules, maximum substitutional solubility can be achieved if: 1) The relative difference between the atomic radii of the solvent and solute is less than 15%, 2) the crystal structure of the involved elements is identical, 3) the solute and solvent atoms have the same valence, and 4) the electronegativity potential is close to zero [10, 11]. The transition metals of group Va (vanadium, niobium, tantalum) and VIa (chromium, tungsten) have a body-centered cubic lattice too and further sufficiently fulfill the previously mentioned requirements for substitutional solubility [1]. The solute atoms replace the molybdenum atoms in their lattice position, thereby the lattice gets locally distorted and the material's yield strength is increased [2]. Substitutionally solid solution strengthened molybdenum-tantalum (MT11), molybdenum-niobium (MoNb10), and molybdenum-tungsten (MW20, MW30, MW50) are commercially produced, sold and applied in coating technologies [4].

Beside solid solution strengthening, molybdenum is primarily strengthened by work hardening [12]. After pressing and sintering, the material is further processed and mechanical deformed by thermomechanical processes (e.g. rolling, forging). During hot deformation, molybdenum evolves dislocation networks and forms a distinct subgrain structure (fig. 3) [13–16]. The developed subgrain boundaries in combination with the actual grain boundaries act as barriers and hinder the dislocation movement [17]. However, highest degrees of deformation can only be achieved by annealing which weakens the effects of work hardening. The occurring primary recrystallization decreases the material strength as a result of the annihilation of subgrains and recovers the unworked properties. Consequently, recrystallization limits the achievable working/service temperatures, hence to provide high-temperature strength a different alloying approach is needed [18].

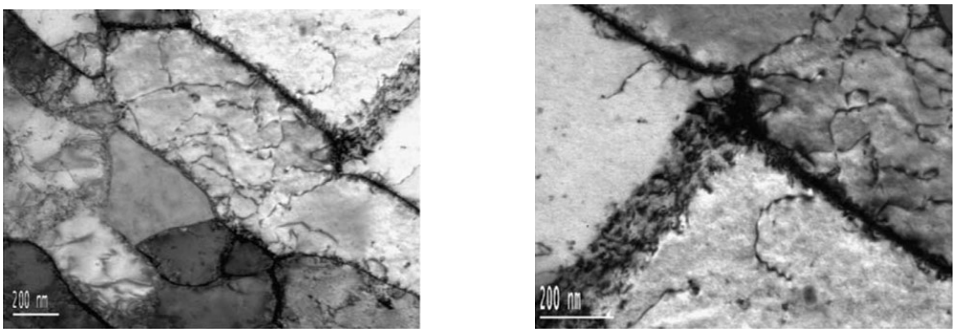

(a) (b)

Figure 3: Formation of dislocation networks (subgrains, cell walls) in "as-worked" molybdenum alloy TZM (TEM) [18]

By adding fine particles of reactive metal carbides to molybdenum, precipitated finely distributed carbides (fig .4) act as recrystallization inhibitors, and recrystallization temperature of pure molybdenum (1000–1200 °C) and hence high-temperature strength can be increased significantly [19]. Earlier studies [20, 21] attributed carbide stabilized alloys a combination of several strengthening mechanisms included: 1) Precipitation and dispersion hardening by carbide and oxide particles, 2) the preservation of the mechanically deformed structure and work hardening properties, and 3) a interstitial/substitional solid solution strengthening by alloying elements not contained in the carbide particles. Recent studies [22, 23] supplement earlier perceptions, no direct-strengthening (Orowan-strengthening) by the fine distributed carbide particles, which act as barriers to dislocation motion during deformation, was observed. Instead it is assumed that the carbides pin the grain boundaries and subgrain boundaries and lead to a more fine-grained structure (indirect strengthening). The fine-grained microstructure further improves the mechanical properties ductility and fracture toughness.
Commercially produced carbide stabilized strengthened molybdenum alloys are e.g. Titanium-Zirconium-Molybdenum (TZM) or Molybdenum-Hafnium-Carbon (MHC). These alloys are applied in high-tempearature applications with demanding loading conditions such as forging tools, extrusion dies or rotating anodes in X-ray tubes [4].

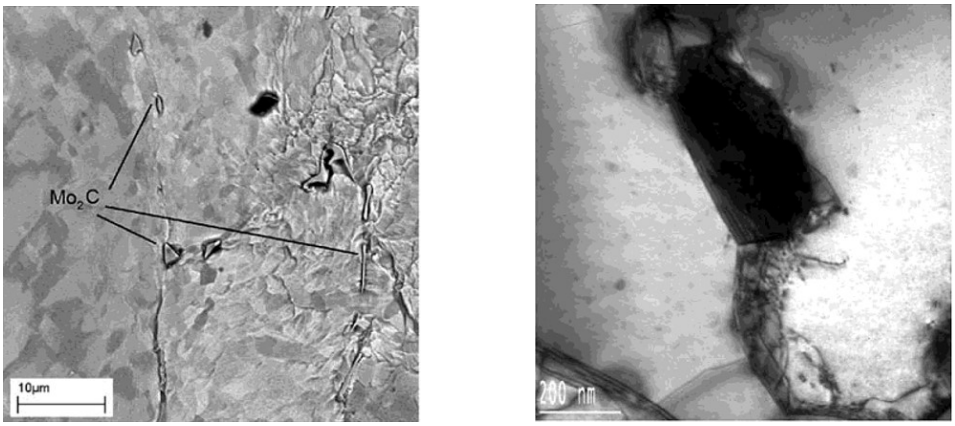

(a) (b)

Figure 4: Carbide precipitations in TZM: (a) Mo_2C at grain boundaries (SEM) and (b) $(Mo,Ti)_xC_y$ at subgrain wall (TEM) [18]

Indirect strengthened carbide stabilized molybdenum alloys (e.g. TZM and MHC) possess a high recrystallization temperature and high-temperature strength. However, the suitability of certain alloys for long-term service applications at elevated temperatures above $0.5 \cdot T_m$ are limited. During service, the carbide precipitations are not stable at the high temperature exposure and will coarse or dissolve into solution. Thereby, the strength by carbide stabilization is lost and the material does not provide a sufficient level of creep/tensile strength anymore [21, 24, 26]. Due to molybdenum's very low solubility of oxygen and the moderate affinity to form oxides, oxide dispersion strengthening (ODS) offers an interesting alternative to carbide strengthening of molybdenum [25, 26].

By adding molybdenum-oxides to a liquid rare-earth solution (S-L wet doping), oxide dispersion strengthened (ODS) molybdenum alloys containing fine dispersed rare-earth oxides (e.g. La_2O_3, Y_2O_3) can be produced [26–28]. To improve the mechanical properties, these alloys are further processed and work hardened to achieve final degrees of deformation up to 99%. TEM studies focusing on the oxide shapes and the interface between particles and molybdenum matrix revealed a different deformation behavior of the processed oxide particles. During mechanical processing a distinction can be drawn between the rigid and non-deformable particles (e.g. Y_2O_3) causing microvoids at the interface, and the softer deformed particles (e.g. La_2O_3) [29]. The created microstructure of Mo-La ODS consists of high aspect ratio pancake-like shaped grains and fine dispersed oxides. The fine dispersed oxides are presented as ribbons or stringers (fig.5) and aligned along the working direction and the grain boundaries [30]. For ODS molybdenum alloys, the recrystallization temperature is determined by 1) the oxides size, 2) their distribution, and 3) volume content. While large particles tend to particle stimulated nucleation (PSN) of recrystallization and decrease the recrystallization temperature, smaller ones are able to pin subgrain boundaries, retard nucleation and thus shifts recrystallization

to elevated temperatures (e.g. ODS Mo - 0.3wt% La $_2O_3$ -1800 °C) [31, 32].
Commercially produced and sold oxide dispersion strengthened molybdenum alloys are e.g. Molybdenum-Lanthanum-Oxide (ML) and Molybdenum-Yttrium-Cerium-Oxide (MY). Certain alloys are applied for high-tempearature applications such as furnace components, in the lightning industry, and in coating technologies [4].

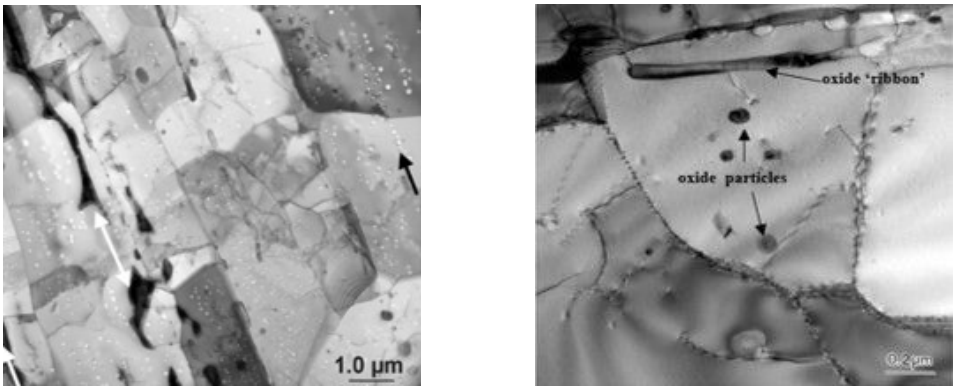

(a) (b)

Figure 5: Oxide particles in ODS molybdenum: (a) Ribbon & discrete La_2O_3 oxides and irradiation caused voids (TEM), and (b) ODS molybdenum sheet discrete & ribbon oxide particles and dislocation networks (TEM) [33]

2.1.2 Oxidation, Cold Brittleness, and Recrystallization

The influence of impurities on refractory metals has been studied intensively in the past. It has been observed that there is a high chemical affinity especially at elevated temperatures of molybdenum to gases (oxygen, nitrogen, hydrogen). A higher volume of the formed surface oxides compared to the specific volume of the base metal leads to cracking or exfoliation of the formed oxide layer, and further increase the oxidation rate. However, oxygen does not only occur in the formed surface oxide layers; it also might form a solid interstitial solution within the base metal [1]. The group VIa transition metals (molybdenum, tungsten, chromium) show a low solubility of oxygen in solid state condition. Therefore, if the solubility of oxygen in molybdenum is exceeded, oxides are formed along the grain boundaries and increase the hardness noticeable. The distributed brittle oxides along the grain boundaries weaken the grain boundary strength, reduce the material toughness significantly, and promote intergranular fracture (intergranular embrittlement) [1, 34, 35].
Despite a minimized amount of interstitial impurities in the raw material and continuous improvement of the powder metallurgy process, the harmful impurities cannot be avoided completely. Two strategies are possible to prevent the impurity driven grain boundary embrittlement: 1) Gettering or replacement of the harmful impurities by grain boundary cohesion enhancing impurities [36, 37] or 2) by adding s-block and p-block elements for grain boundary segregation to provide cohesion [38, 39]. Recent research [40] identified

carbon and boron (p-block elements) as the main grain boundary strengthening elements. The segregated elements along the grain boundaries increase the grain boundary cohesion and promote transgranular fracture. For future alloy design, a further reduction of oxygen in combination with the addition of carbon and boron is recommended.

In addition to the affinity to form oxides, molybdenum is prone to brittle fracture at room temperature and its brittleness limits application and obstacle utilization like every metal. The group VIa metals (tungsten, molybdenum), with their body-centred structure (bcc) exhibit a transition from brittle to ductile fracture mechanism in a certain temperature range (DBTT) [1]. Generally, metals with a bcc lattice provide a sufficient level of ductility at homologous temperatures of $T/T_m > 0.3$ [41]. For the application below transition temperature (e.g. room temperature ($T/T_m \approx 0.1$)) and in case of failure, the crack propagation is likely determined along cleavage planes (transgranular) or along grain boundaries (intergranular) with nearly no elongation (fig. 6) [1].

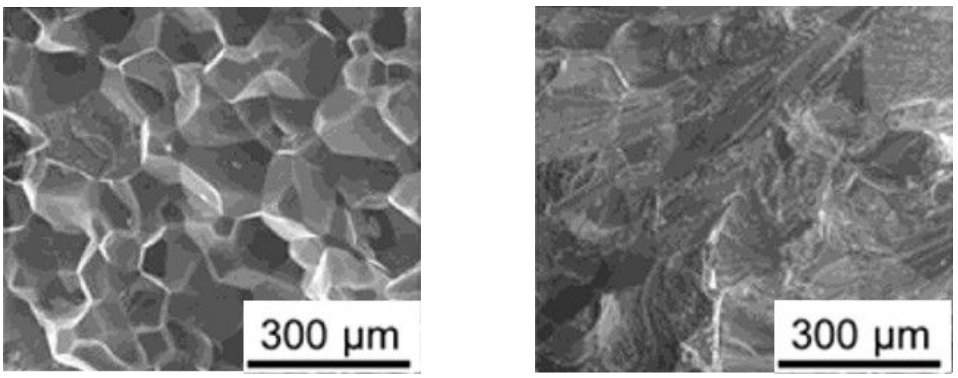

(a) (b)

Figure 6: Fracture surfaces of at room temperature tensile tested Mo-Hf alloys: (a) Intergranular fracture Hf 0.18 at% (SEM), and (b) transgranular fracture Hf 2.17 at% (SEM) [40]

However, the ductile-brittle transition temperature is not a constant value and it also depends on various influence factors such as grain size and shape, grain boundary character, purity of the metal, addition of alloying elemets or, and slip/deformation mechanisms [42–47].

The recrystallization temperature is considered as a benchmark for the strength of the interatomic bond of metals and alloys. The stronger the interatomic bond and higher the recrystallization temperature, the higher the strength of metals and alloys at room and elevated temperatures. Heating above the recrystallization temperature is in general accompanied by a reduction of strength and simultaneous increase in plasticity. For commercially pure molybdenum, the recrystallization annealing results in an embrittlement, which is not an intrinsic property of molybdenum, but is caused by the redistribution of the remaining impurities and their precipitations along the grain boundaries. During recrystallization annealing, the atoms of the distorted lattice overcome their atomic bonds

with the nuclei of new, undistorted grains and their subsequent growth. Consequently, there is a transition of the distorted to more thermodynamically stable, undistorted crystallites and a relief of internal stresses. At the beginning of the two staged recrystallization, the distorted grains are replaced by undistorted grains (treatment recrystallization), then followed by the growth of the new and undistorted grains (collective recrystallization) and resulting mutual contact in order to obtain the most thermodynamically stable state of a single-crystal structure. However, the rates of collective recrystallization are lower compared to the treatment recrystallization, and impurities and inclusions along the grain boundaries retard the actual grain growth. Further, the commencement of recrystallization and resulting grain size strongly depend on the previously experienced manufacturing history and degree of deformation. Certain correlations are visualized by recrystallization diagrams (fig. 7) and are helpful for the selection of heat treatments after cold deformation or the determination of capable service conditions [1].

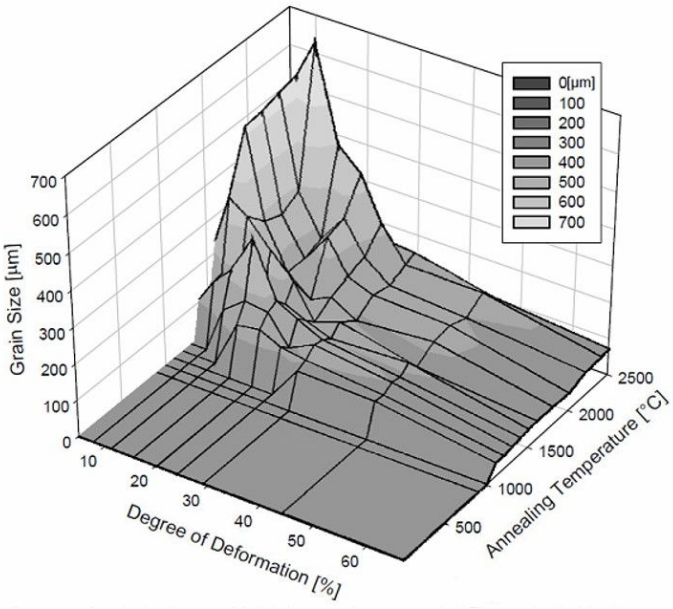

Figure 7: Recrystallization diagram of a rolled technically pure molybdenum sheet material. HT: 20 min heating time, 1 h annealing & cooling in furnace [6]

To extend the field of application and improve service condition, increased recrystallization temperatures are needed. By adding alloying elements, the commencement of recrystallization may be shifted to elevated temperatures. Substitutional solid solution strengthening of molybdenum (e.g. by rhenium) inhibits recrystallization caused by the strengthening of the interatomic bonds in the formed solid solution. The addition of rhenium not only provides room temperature ductility, it also increases the recrystallization temperature by 400 °C [1]. Further, the recrystallization behavior is affected by the purity of the metal with respect to interstitial impurities. Finely dispersed and uniformly distributed inclusions of carbides and oxides of thermodynamically active el-

ements substantially increase the recrystallization temperature of molybdenum. Major impact is achieved by adding e.g. titanium, zirconium, or hafnium to molybdenum [1].

However, being a body-centered cubic metal entails a high stacking fault energy (molybdenum 0.3 J/m^2), and recrystallization behavior is predominated by concurrent recovery process [48]. The formation of recrystallization nuclei of subsequent static recrystallization occurs via coalescence and growth of subgrain regions (fig. 8) that have been formed during dynamic recovery (in-situ recrystallization). The required coalescence of neighboured subgrains is formed by small rotations in their orientations, and is promoted by the distinct hot-worked and sharp texture of molybdenum which contains small orientation differences between the grains [6,49]. The distinct primary hot-worked texture is weakend during recrystallization caused by a steady growth of the subgrains and influences subsequent evolved microstructure and texture of recrystallization [50,51]. Recovery and recrystallization are the only mechanisms that control microstructure evolution of technically pure molybdenum in solid state [52].

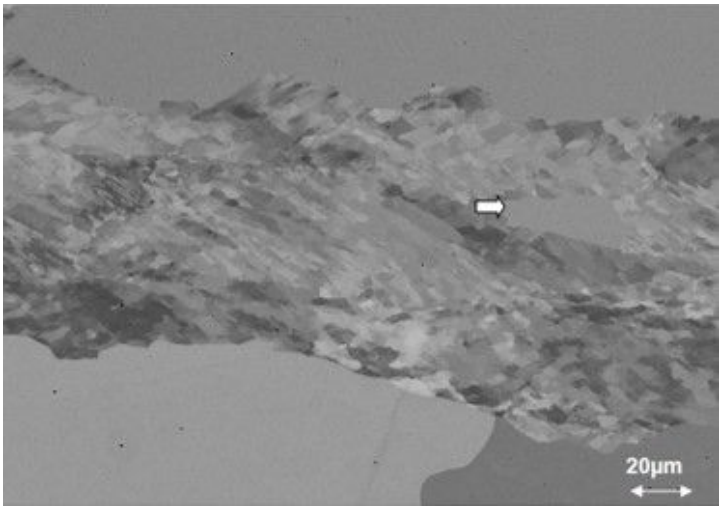

Figure 8: Coalescence of subgrains (arrow) acting as recrystallization nucleus and recrystalized by in-situ recrystallization (ECCI) [6]

2.1.3 Weldability of Molybdenum and Molybdenum Based Alloys

Nowadays, semi-finished molybdenum products are mainly produced by powder metallurgy (PM) and achievable dimensions are restricted to process limits. The application of joining technologies is a major interest to generate integral structures made out of the powder metallurgically processed molybdenum parts, though materials physical and chemical properties (e.g. melting point T_m, solubility, chemical reactivity) challenge joining and restrain applicable welding procedures. Molybdenum's melting point of T_m = 2623 °C combined with its high thermal conductivity and low heat capacity require a

high and concentrated heat input at the weld interface to countervail the rapid heat dissipation. Moreover, the material's susceptibility to embrittlement caused by low amounts of impurities (e.g. absorbed from weld atmosphere [53]) segregating along grain boundaries and extensive grain growth during recrystallization in the heat affected zone (HAZ) further limits the weldability. High-intensity heat sources such as electron beam, laser or tungsten inert gas welding are the most promising procedures to deal with molybdenum's special properties.

In [54] and [55], the mechanical properties of TIG welded TZM sheets were evaluated. Extensive grain coarsening in the heat-affected zone (HAZ) and fusion zone (FZ) were observed and resulted in embrittlement of the welds (fig.9). Arc welded TZM revealed a poor joint performance premised on a reduction of ultimate tensile strength (UTS) accompanied by nearly no fracture elongation. To provide a sufficient level of ductility of the weldments, a change of the chemical composition offers a suitable alternative. Beside the addition of rhenium to form a softened ductile substitutional solid solution [56, 57], the adding of small amounts of boron and zirconium prevents grain boundary embrittlement and extends the fracture elongation [47, 58]. The segregated boron, zirconium, and carbon suppress the formation of harmful molybdenum-oxides and oxygen concentration along the grain boundaries. The inhibited oxygen segregation shifts the predominant intergranular fracture failure to a transgranular failure, and results in an improved ductility of arc welded TZM [36, 59].

Electron beam welding (EBW) is a more suitable alternative to TIG welding and enables the joining of refractory metals without the need of a filler material. The vacuum in EBW ensures no contact to oxygen during processing and provides a high energy density resulting in a narrow weld zone (fig. 9), and heat-affected zone, which leads to less impact of the HAZ on the weld's properties [60].

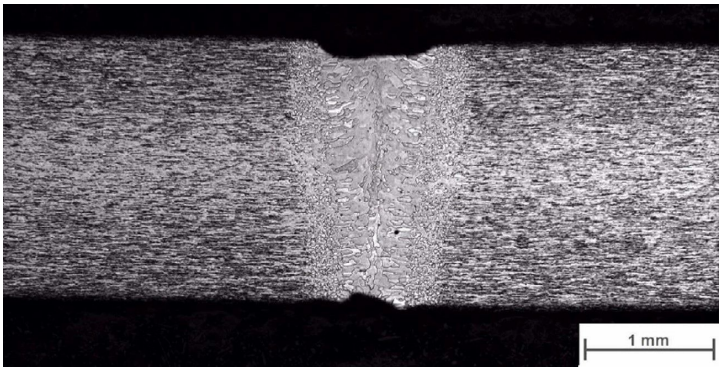

Figure 9: Weld cross-section of electron beam welded (EBW) 2 mm TZM sheets without filler material, with PWHT [61]

By using EBW, the obtainable ultimate tensile strength of molybdenum metal joints can be increased compared to TIG welds and extensive grain coarsening is suppressed.

Therefore, for joining molybdenum, high energy density welding procedures are preferable over common arc welding techniques [54,55,62]. However, regarding a nearly similar insufficient fracture elongation and the material's intrinsic residual oxygen level (e.g. 250 ppm), the influence of oxygen even at welding under vacuum cannot be avoided completely [54]. [63–65] observed the formation of various precipitations including the segregation of MoO_2 and TiO_2 along grain boundaries in the FZ. By alloying zirconium, plugged in as thin foil filler metal, the preferable reacted ZrO_2 ($\Delta G_{ZrO_2} < \Delta G_{TiO_2} < \Delta G_{MoO_2} < 0$) purifies the grain boundaries and relieve tensile stress concentration at partial grain boundaries. The further obtained improvement of the ultimate tensile strength is contributed to a change of fracture mode from mixed intergranular and transgranular fracture failure to fully transgranular cleavage fracture [66].

High-density fusion welding procedures combined with a controlled alloying purify grain boundaries and retard extensive grain coarsening. Nevertheless, the weldment's embrittlement and loss of strength cannot be avoided completely and other techniques should be taken into particular consideration. Solid state welding, precisely friction welding, offers an interesting alternative to fusion welding procedures and a general feasibility for joining refractory metals has already been proven in the past [53]. With occurring temperatures essentially below the melting temperature and the featured natural self-cleaning effect by extruding oxides at the surface and impurities out of the weld interface, rotary friction welding seems an appropriate welding procedure for joining axisymmetric tubes. So far conducted friction welding attempts mainly dealed with TZM [54], and assessed mechanical properties confirm the previous mentioned assumption of suitability. The technique of friction welding avoids the negative impact of fusion welding and reduces the material embrittlement. The ultimate tensile strength of TZM joints tested at RT and elevated temperature after post weld heat treatment (PWHT) was nearly similar to the value of the base material and was accompanied by a fracture elongation up to 35%. Light optical microscope characterization revealed a for friction welding typically evolved microstructure (fig. 10), and contained representative weld sections (e.g. TMAZ) resulting from high deformation and deformation rates during processing [67].

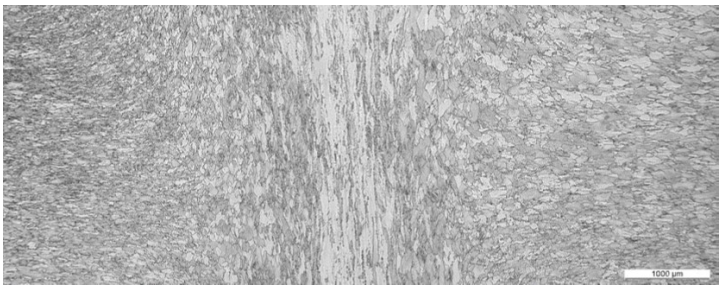

Figure 10: Cross-section rotary friction welded (RFW) commercially pure molybdenum with PWHT [68]

However, previous studies have shown that joining commercially pure molybdenum is much more challenging. Providing a sufficient drive power, occurring motor overload, extensive plastic deformation and rapid upset rates are only selected challenges to deal with and complicate establishing a solid direct drive friction welding process. Experimental practice and provided technical information (e.g. drive power) for friction welding molybdenum metals are limited, and general guidelines are missing. A more systematic and basic study for friction welding molybdenum is needed to investigate materials behavior during processing to describe its displacement history and to develop an established robust process design [68, 69].

2.2 Rotary Friction Welding (RFW)

Friction welding (FW) is classified as a solid state welding (SSW) technique. Solid state welding produces coalescence of the contacting surfaces at a temperature essentially below the melting temperature of the parent metal without the need of additional filler material. SSW techniques involve either the use of enhanced pressure and massive deformation, or diffusion and limited deformation to generate joints between similar and dissimilar materials [70]. In friction welding, the required heat for joining is generated locally by the relative motion of the two facing surfaces being joined, and the required deformation is ensured by the accompanied applied axial pressure. FW is based on the direct conversion of mechanical to thermal engery without further application of external heat sources, and involves heat generation through 1) friction abrasion, 2) heat dissipation, 3) plastic deformation, and 4) chemical interdiffusion. Friction welding implies linear friction welding (LFW), friction stir welding (FSW) and rotary friction welding (RFW). In rotary friction welding, the two established process variations direct drive friction welding (DDFW) and inertia friction welding (IFW) are the most commonly and widely used welding procedures for joining axisymmetric components [70, 72, 73].

The rotary friction welding principle steps are illustrated in fig. 11. First, one component rotates while the other one is held stationary. Further, the two components are brought into contact under constant or gradual increase of axial pressure until the weld interface reaches thermal shear strength range and the required upsetting starts (friction phase). Finally, once the weld interface is heated up, the rotation is stopped and axial pressure is increased (forging phase) which consolidates the weld. The occurring diffusion at the final stage enables a metallurgical bond and joining of the parts [70].

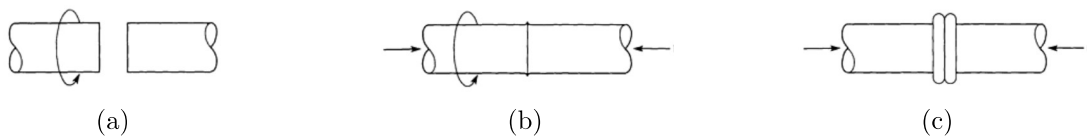

Figure 11: Schematic illustration of the principle steps in rotary friction welding: (a) initial phase, (b) friction phase and (c) forging phase [70]

The interrelation and the actual cause of heat generation in rotary friction welding is still discussed in literature and complicates setting up predictive models. However, performed empirical studies enabled an in-depth understanding of the process itself and identified qualitative influence factors in a variety of materials. Related friction welding process related factors are 1) interface temperature, 2) applied pressure levels and 3) relative velocity of the surfaces [70].
The weld interface temperature is probably the most decisive factor for the plasticization behavior and the microstructure evolution. The prevailing maximum interface temperature in steady-state phase is approximately between 0.75 and 0.95 of T_m. The obtained maximum normalized interface temperature is affected by applied pressure levels or material selection. It is assumed that an increased applied pressure or low thermal diffusivity combined with a pronounced decrease in strength at elevated temperatures results in a relatively low interface temperature (e.g. titanium) [72].
Further, the quality of the generated joints relies on the applied pressure and the relative velocity of the surface during processing. They are determined by the selected input parameters in order to control and adjust the rotary friction welding process. However, the controllable input parameters and general process design differ for inertia friction welding and direct drive friction welding [73].

2.2.1 Inertia Friction Welding vs. Direct Drive Friction Welding

In general, rotary friction welding can be divided depending in which manner rotational energy is converted into heat [72, 73].

In inertia friction welding, one of the facing workpieces is held stationary while the other one is attached to a flywheel. The flywheel is speed up to a certain speed and thus to a predetermined stored amount of rotational energy. Then, the drive of the flywheel is disengaged and the parts are brought in contact. By applying axial pressure, friction is generated and the relative speed is continuously reduced resulting in a permanent deceleration of the flywheel with the attached rotating workpiece (fig. 12a). Depending on the amount of applied pressure levels, inertia welding is distinguished in single-staged and two-staged welding. In certain cases and similar to the direct drive friction welding, enhanced forging pressure close to the spindle stop may be used for an even more concentrated power input before spindle stop.
The angular momentum inertia of the flywheel, the initial flywheel speed, and the applied axial pressure(s) are the three main input variables to control and adjust the inertia friction welding process. The total amount of weld energy is determined by the initial speed and the angular momentum inertia of the flywheel, and are considered as the key performance indicators in inertia friction welding. Corresponding actual power input and welding cycle time is related to the continuous deceleration of the flywheel. The deceleration rates depend on the applied axial pressure levels and the inertia of the rotating components and the flywheel [71, 73].

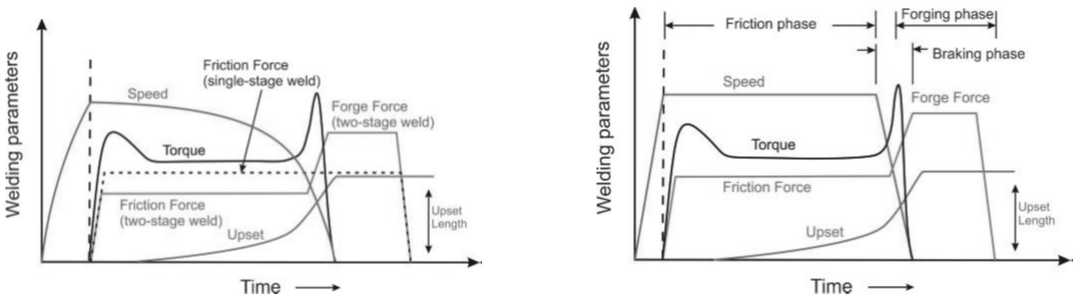

Figure 12: Schematic illustration welding parameters over time for: (a) A inertia friction welding (IFW) process and (b) a direct drive friction welding (DDFW) process [73]

In direct drive friction welding, the process stages are classified by the (constant) speed and the applied pressure levels into friction phase and forging phase. The objective in the friction phase is to generate heat by the applied constant axial pressure in combination with a constant relative speed. Axial shortening ("burn off") and torque undergo a change and vary over time during the friction phase. At the process start in the initial stage of the friction phase, the torque instantly increases to a maximum peak and further drops to an equilibrium value. The vital change of the resisting torque is associated with asperity interactions (e.g. interlocking, breaking) and a subsequent material softening in the weld interface by the generated friction heat. The ensuing equilibrium stage indicates a quasi-steady-state intrinsic self-regulation of the process and a balance between strain hardening and temperature softening. Finally, the forging phase is initiated by terminating the rotation and increasing the axial load in the weld cycle. The rate of spindle deceleration and resulting braking cycle time effects the weld interface temperature and collaboration with the forging pressure. Actual forging pressure can be applied while the braking phase and spindle deceleration ("forging into the turning spindle"), or at the end of the braking phase and after spindle stop. In case of initiating actual forging while decelerating, a second maximum torque peak is observed. The torsion leads to spiral material flow lines (fig. 13a). In case of continued axial forging after spindle halt, the torque decreases without a previous peak to zero while retarding. Hence the rotary motion is stopped, the axial shortening is only affected by applied axial forging force and results in radial material flow lines (fig. 13b) [71, 73].

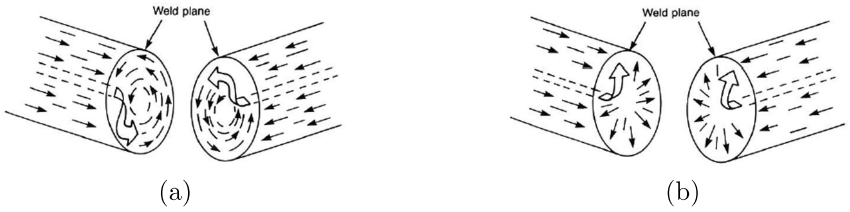

Figure 13: Schematic illustration upsetting material flow lines while forging phase: (a) Spiral flow lines and (b) radial flow lines [71]

For DDFW, more input variables need to be set than for IFW. The process is less subjected to restrictions and more flexible in design. However, the numerous input parameters complicate the identification of the optimum conditions before actual experience is obtained. 1) The relative velocity, 2) applied axial friction pressure, 3) friction time, 4) deceleration time/spindle braking rate, 5) time delay forging, 6) applied axial forging pressure, and 7) forging time are the input variables in order to control and adjust the direct drive friction welding process and to maintain a sufficient level of heat and plastic deformation. However, the relative velocity, applied friction pressure and duration of friction phase ("burn off"), and applied forging pressure (upsetting) have been identified as the major input variables with the most significant impact. For practical application, not every parameter needs to be controlled and simplifications, e.g. initial transition from friction to forging pressure after spindle deceleration, have to be made [71].

Direct drive friction welding as well as inertia friction welding are suitable to produce sound solid state welds. However, subtle differences and benefits for each of the two techniques exist. In inertia friction welding, the machine power requirements are inherently lower than in DDFW, as the flywheel acceleration is done priorly to welding. The provided weld energy is rapidly emitted and the welding cycles are much quicker than in DDFW. This results in a steep temperature gradient and a narrow HAZ. In direct drive friction welding, a high machine drive power is required to provide a constant relative velocity under the applied loading. In order to avoid an oversizing of the motor unit, it is common practice to select moderate pressure levels. The lower axial pressure levels and relative velocity in DDFW than in IFW are evidently balanced by a longer heating phase and welding cycle. A multitude of input variables enable a precise process control and the adjustment of every single welding stage. The gathered knowledge and general established guidelines are mainly determined empirically for widespread materials (e.g. various steel-, aluminium-, titanium grades). Several other factors such as material properties, axial shortening rate or geometry need to be taken into consideration and for each material the optimised parameters and their configurations are different [71, 73].

2.2.2 Weld Sections of Rotary Friction Welding

In friction welding, the maximum occurring temperature generally does not exceed the melting temperature of the bonded material. Nevertheless, the maximum weld interface temperature peak can be close to the liquidus temperature [72]. A high temperature gradient within the weld specimens along with the applied pressure levels result in a gradient of occuring strain and strain rates in the HAZ, and a significant evolution of microstructure close to the weld interface. No standard or widely accepted nomenclature is established for the evolved microstructure sections in rotary friction welding. The classification in literature is mainly derived from the more popular friction stir welding and received widespread acceptance [74]. Evolution of microstructure and the different zones within the HAZ can be divided into (1) contact zone, (2) fully plasticized zone, (3) partly deformed zone / TMAZ and (4) undeformed zone (fig.14) [72–76].

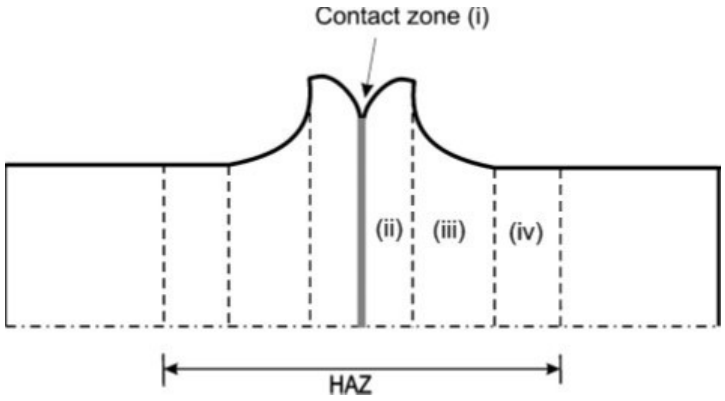

Figure 14: Schematic illustration weld sections within HAZ in rotary friction welding: (i) contact zone, (ii) fully plasticized zone, (iii) partly deformed zone and (iv) undeformed zone [73]

The contact zone is characterized by the contact of the joined parts and subject to a severe plastic deformation. During processing, the permanent rubbing of the contact surfaces results in a material transfer of fragments from one rubbing surface to another. The actual strain rate is determined by the applied relative velocity, and the evolved microstructure is uniformly fine grained due to a severe straining and the elevated prevailing temperature [73].

The fully plasticised zone is the region next to the weld interface and does not participate in materials rubbing and material transfer. This region is exposed to a considerable amount of heat and plastic flow, and features a high dislocation density. The evolved microstructure in this zone differs from the other regions within the HAZ. If a sufficient activation energy is provided, the plastic strain is accommodated by dynamic recovery or recrystallization of the microstructure and leads to an equiaxed, fine grained microstructure. The fully plasticized zone is generally subjected to heat and plastic deformation, and therefore theoretically a subgroup of TMAZ. However, due to the vastly different microstructure they are regarded separately [73–76].

In the partly deformed zone (TMAZ), the occurring temperature, strain rate, and amount of plastic deformation are lower than in the upstream zones. The experienced thermal cycle may be sufficient to permit dissolvent of strengthening precipitations, and the deformation is accommodated by an increase of the dislocation density. The reduced strain and strain rate result in a coarsened, deformed microstructure that is partly recovered or recrystallized [73–75]

The undeformed zone is only limited to thermal exposure of welding without any optical visible plastic deformation. A microstructure and/or mechanical properties change may take place, e.g. grain growth, re-precipitation of previous dissolved elements or solid-state transformation. Finally, the undeformed zone and parent metal merge seamlessly,

where no change in microstructure or mechanical properties is noticeable [73, 74].

2.2.3 Mechanisms of Bonding in Solid-State Welding

In solid state welding, joining is established due to an atom-to-atom bond obtained by an intimate intermetallic contact in absence of local protective films of the facing weld interfaces. The introduced strain (upsetting) and the elevated temperature (friction heating, plastic deformation) enable joining and facilitate the particular bonding mechanisms. Generally, the predominant bonding mechanisms are classified according to: 1) Contaminant displacement and interatomic bonding, 2) dissociation of retained oxides and 3) decomposition of the interfacial structure [77].

Considering the material's prebonded surface condition on a microscopic scale, the base metal is covered by interfering layers (mechanically affected, contaminated, and oxidized) [77–79]. For bonding, a disruption of the contaminated and oxidized layers and the extension of the contacting surfaces are essential. The applied axial pressure and the generated heat result in local surface strains, which accomplish the disruption of the interfering layers and the separation of the surface contaminations. The base material is extruded in the gap between the separated contaminated films and forms a clean metal-to-metal contact for direct interatomic bonding (fig. 15). However, there are still some scattered residual oxides and fine dispersed contaminant particles across the weld interface remaining, which can be thermally dissolved during friction welding in the base material [77–82].

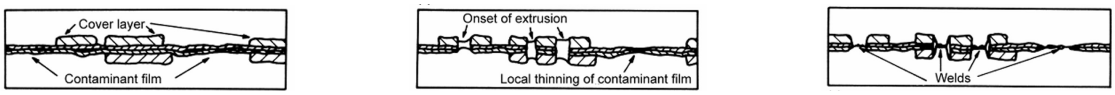

(a) (b) (c)

Figure 15: Schematic illustration interfacial breakup: (a) interfacial prebond surface condition, (b) extrusion and thinning of contamination layer and (c) seperation of contaminated area [79]

The realignment of the grain structures and crystallographic matchup across the bond line is a main topic in friction welding. The participating metals for joining provide in general a polycrystalline structure and require a local crystallographic reorientation [77, 80].

The prevalent macroscopic surface strains, the local inter-contaminant material extrusion and the reoriented matching crystallography across the bondline result in a highly dislocated bondline structure (fig.16) which vitally reacts to the in friction welding provided heat input. The decomposition of the interfacial structure and the relief of bondline stresses are thermally assisted and depend on the amount of provided activation energy (temperature, time). Recovery typically takes place at shorter and lower temperature

cycles, whereby the dislocations realign themselves into dislocation cells to reduce the energy level. The bond efficiency is comparatively weak, if the interfacial decomposition is only limited to recovery. For recrystallization, a higher annealing temperature and provided activation energy is required for the nucleation and subsequent new grain growth. Bondline recrystallization results in the greatest reduction of energy and form high integrity bonds. However, the required actual recrystallization temperature is also a function of the degree of deformation. Therefore the breakdown of the interfacial structure is affected by the thermal cycle and the applied strain. Higher levels of upset/strain enable joining at shorter times and relative low temperatures [77].

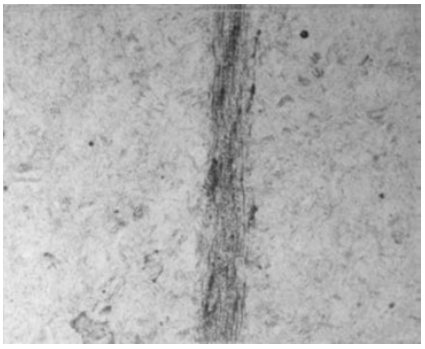

Figure 16: Highly deformed and dislocated bond line structure resistance butt weld mild steel [77]

3 Experimental

The content of this chapter is related to most recent study of Stütz et al. [68] on direct drive friction welding (DDFW) of commercially pure molybdenum. Insufficient power drive, occurring preliminary spindle stall, and "extensive" burn-off prevented an in-depth examination of the influence of welding parameters on the joint quality. This work aims at a more systematic and fundamental study on rotary friction welding (RFW) of molybdenum and molybdenum based alloys in order to establish a robust process design to countervail vigorous upsetting and to provide related technical information (e.g. power input and total energy input). The following study should reveal the underlying mechanisms of extensive plasticization and contrasts the displacement histories of molybdenum metals to a reference low-carbon steel. Experimental welding trials were carried out in small-scale weld cross-sections (Ø9 mm, Ø12 mm) under laboratory conditions on a friction stir welding (FSW) device providing high resolution, process parameter recording, and precise control.

3.1 Investigated Materials

Investigated metals were commercially pure molybdenum, carbide stabilized molybdenum alloy TZM, and as a reference low-carbon steel.

The process chain of powder metallurgy produced commercially pure molybdenum (>99.97 wt%) and TZM (0.5 wt% Ti, 0.08 wt% Zr, 0.01-0.04 wt% C, and bal. wt% Mo) rod material included sintering, hot working (cogging), thermal treating (stress relieve annealing) and machining to final dimensions (Ø9 mm x 30 mm, Ø12mm x 30mm). The thermomechanical processing resulted in a characteristic microstructure of elongated grains along the plastic material flow in lateral direction (fig. 17).

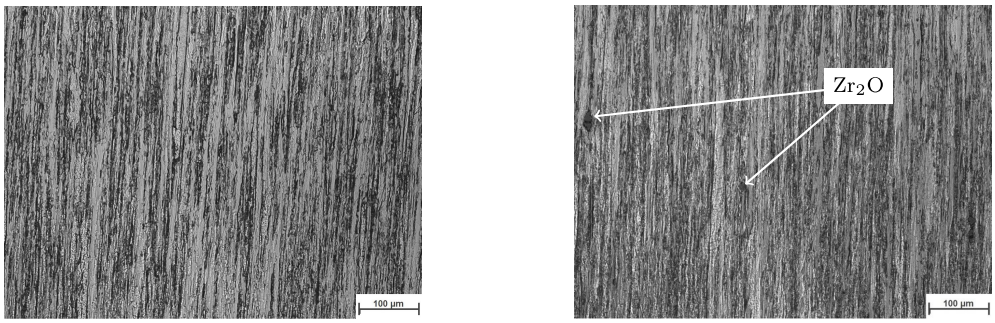

(a) (b)

Figure 17: Base material in lateral direction after thermomechanical processing: (a) Commercially pure molybdenum and (b) TZM [murakami etchant, 200x magnification]

By adding small amounts of titanium, carbon, and zirconium to the molybdenum matrix, the precipitation of fine distributed carbides (e.g. TiC) is promoted and act as getter elements for oxygen (e.g. Zr_2O) (fig. 17b). The formed precipitations inhibit recrystallization, hence increase recrystallization temperature and improve high-temperature strength. During welding, materials thermal conductivity and specific heat capacity determine the temperature distribution within the weld specimens and mainly affect materials strength and microstructure evolution in the surrounding area of the weld interface. The combination of high-temperature strength and excellent thermophysical properties is unique and entirely differs to the referenced low-carbon steel.

Table 1: Selected thermophysical properties of stress relieved molybdenum, stress relieved TZM and AISI 1000 series of low-carbon steels at room temperature [83]

	Molybdenum Stress Relieved	TZM Stress Relieved	AISI 1000 Series
Thermal conductivity λ [W/m K]	138	118	55
Specific thermal capacity c [J/g K]	0.255	0.250	0.511
Density ρ [g/cm^3]	10.22	10.16	7.85
Thermal diffusivity $\lambda/(c.\rho)$ [10^{-6} m^2/s]	53	47	14
Yield strength [MPa]	415	860	>165
Ultimate tensile strength [MPa]	515	965	>295
Melting temperature [°C]	2,623	2,623	1,430

To promote material characterization and value process deviations during rotary friction welding, molybdenum and its alloy were compared to an established material and process design. An unalloyed low-carbon steel (<0.30 wt% C) semi-finished rod material served as a reference to the hot-worked molybdenum metals and were machined to final dimension (Ø9 mm x 30 mm). Light optical microscopy of the parent material in lateral direction revealed a uniform mainly ferritic and pearlitic recrystallized microstructure.

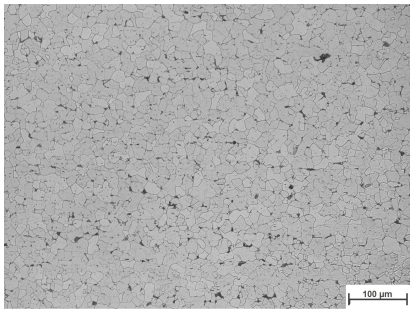

Figure 18: Base material in lateral direction semi-finished rod material low-carbon steel [3% nital, 200x magnification]

3.2 Experimental Set-Up

Small-scale rotary friction welds were accomplished under laboratory condition on a friction stir welding (FSW) device providing comprehensive automatic parameter control and recording. Investigated output variables (actual pressure, welding speed, upset and upset-rate) and technical informations (maintained power drive, machine load and energy input) were derived from selected recorded output parameters (axial force, traveling, spindle speed, loaded, and unloaded torque over time). The NC program and the clamping system were adjusted to resemble a direct drive friction welding process and occuring thermal cycles during welding were logged.

3.2.1 Friction Stir Welding (FSW) Device

Welding experiments with small-scale (Ø9 mm, Ø12 mm) weld specimens of cross-sections 63 mm^2 and 113 mm^2 were conducted by using the 2D R&D *I-STIR BR4* device from *MTS Systems Corporation* (fig. 19) at the *Institute of Materials Science, Joining and Forming, Graz University of Technology*. The machine combines its moving weld head (Y & Z axes) and machine table (X axis) to a 3d manipulation system, and provides another option to manually adjust the pitch axis (for RFW tilt angle $\alpha = 0$ °).

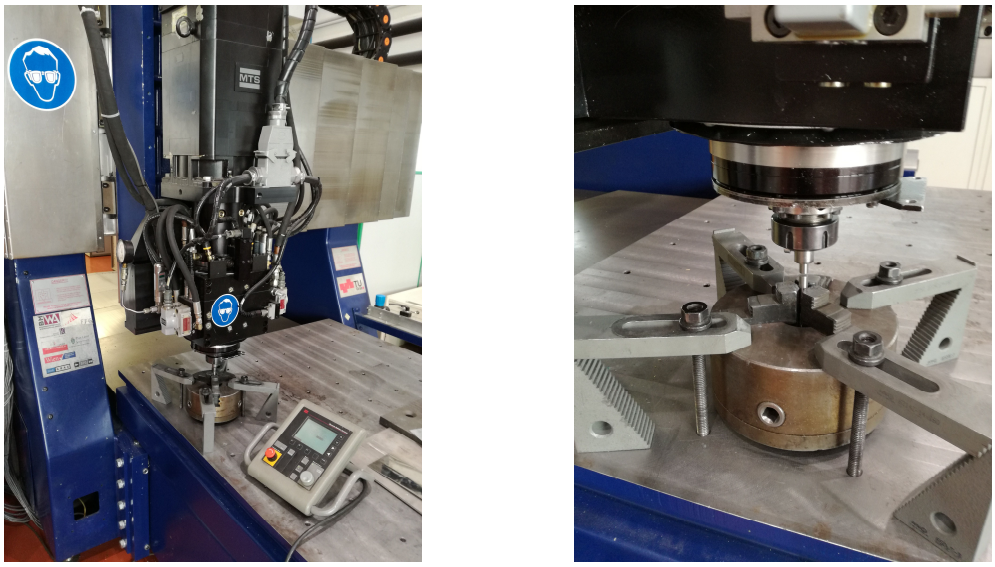

(a) (b)

Figure 19: Experimental set-up DDFW: (a) FSW MTS I-STIR BR 4 device and (b) applied clamping system

The numeric control of the machine is freely programmable and the axial movement can be controlled by displacement- or load control. In addition, to prevent an overheating of the tool and the weld head during friction welding, a separated liquid-cooled tool holder can be plugged in. However, the application of the plugged in cooling system

would influence the heat flow and distort the actual energy input, and was therefore consciously avoided. Analysis of the recorded machine data revealed only a slight increase of the machine front spindle temperature by 12 °C to 56 °C during processing, and indicates that despite the experienced weld temperature peaks (>1600 °C) an overheating can be ruled out in the short welding cycles.

The machine capabilities regarding DDFW requirements are: 1) Recording frequency of 20 Hz, 2) maximum attainable axial force of 35.6 kN, 3) spindle speed of 3200 rpm, 4) torque of 180 Nm and 5) axial travel of 19 mm (effectively <16 mm).

3.2.2 Clamping System

To engage the weld specimens in position and avoid adverse translation and rotation, an adjusted clamping system was implemented as depicted in fig. 20. The designed pin-sleeve (2) was plugged into the FSW weld head (1), axial fixation was ensured by axial form lock and rotary lock by using a fixation screw (3) for the notched and later on rotating weld pins (4). Stationary weld pins (4) were positioned by an adjustable counterpart (6) and fixed on the machine table (7) by a fastened jaw chuck (5).

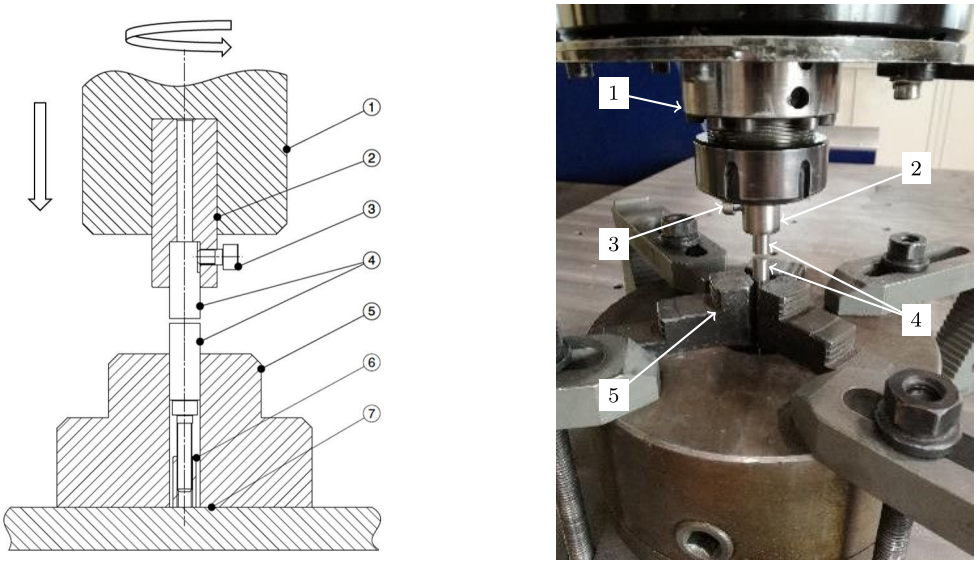

(a) (b)

Figure 20: Clamping set-up DDFW: (a) Schematic illustration clamping system and (b) actual applied clamping system

Various materials (mild steel, stainless steel, hot work tool steel, hard metal) were applied for the pin-sleeve and the most capable one considering durability, high temperature strength, and deformation proved to be 1.2343 hot work tool steel and tungsten based hard metal.

3.2.3 Temperature Measurement

To reconstruct the material's temperature history during rotary friction welding, selected stationary weld specimens were equipped with thermocouples along the outer circumference. Mounted thermocouples were resistance spot welded 2 mm and 10 mm away from the weld interface and recorded actual local temperatures over time (recording frequency of 300 Hz). Based on the enhanced service temperatures two different types were applied: (1) K-type thermocouples (chromel – alumel) for low-carbon steel approved for maximum operating temperature of 1260 °C [84] and (2) S-type thermocouples (platinum – rhodium) for molybdenum metals approved for maximum operating temperature of 1600 °C [84]. Measuring signals were amplified by an *HBM MX840B universal amplifier*, while data acquisition and monitoring took place by means of the *HBM catman DAQ* software.

3.3 Assessment of Process Design

The material's behavior during direct drive friction welding and generated joints were assessed by means of: 1) Process accuracy analysis of the recorded parameters, 2) estimation of technical information considering 3) calculated derived variables, 4) characterization of the evolved microstructure and related 5) mechanical properties.

3.3.1 Machine Capability and Process Accuracy

The machine's capability for rotary friction welding and automatic process control were valued by opposing nominal and actual input parameter courses after welding. Process accuracy and error were determined by calculating the relative error δ over time and overall mean relative error $\overline{\delta}$ for the input parameters axial pressure p and rotational speed n.

The measurements and error analysis is commonly used for evaluating process data, and process accuracy is frequently reported by using the relative error [85]. Let the nominal value of a quantity be $x_{nominal\ i}$ and the measured actual value be $x_{actual\ i}$. Then the incremental relative error δx_i and overall mean relative error $\overline{\delta x}$ of the quantity are defined by:

$$\delta x_i = \frac{\mid x_{actual\ i} - x_{nominal\ i} \mid}{x_{nominal\ i}} \times 100 \tag{3}$$

$$\overline{\delta x} = \frac{1}{N} \sum_{i=1}^{N} \delta x_i \tag{4}$$

3.3.2 Recorded Output Parameters and Derived Variables

Beside actual applied pressure and rotational speed, the axial upset of the FSW weld head z and motor torque in loaded T_{load} and unloaded T_{unload} condition were logged. Subsequently, technical information and performance indicators were derived based on the previous recorded output parameters. Derived and calculated variables were: Axial upset-rate $\dot{z}(t)$ (eq. 5), provided weld power input $P(t)$ (eq. 6), and maintained weld energy input $E(t)$ (eq. 7).

A centered difference quotient was used to approximate incremental axial upset-rate $\dot{z}_i$ over the interval $\Delta t = [t_{i+1}, t_{i-1}]$ and is defined by:

$$\dot{z}_i \approx \frac{z_{i+1} - z_{i-1}}{t_{i+1} - t_{i-1}} \tag{5}$$

Power input was determined by the difference between loaded T_{load} and unloaded T_{unload} torque, rotational speed n and mechanical efficiency η. For simplification, the efficiency η was set to one and it has to be considered that the actual weld input power and energy related to reported values is lower. Incremental weld power input including simplification is defined by:

$$P_i = (T_{load\ i} - T_{unload\ i}) \cdot \frac{2\pi}{60} \cdot \ n_i \ \cdot \eta \quad | \ \eta = 1 \tag{6}$$

Overall maintained weld energy input is calculated by summing up the incremental weld energy input E_i. The maintained weld energy input is defined by:

$$E = \sum_{i=1}^{N} E_i = \sum_{i=1}^{N} P_i \cdot \Delta t \tag{7}$$

3.3.3 Microstructure Characterization

"As-welded" specimens were visually inspected and evalued with respect to a proper flash formation. Further, the friction welds were mechanical and electrical discharge machined (EDM) in the longitudinal direction and transversely trimmed. The trimmed regions of interest were hot-mounted, abrasively grinded with various grit sizes and polished up to a grit of size 1 µm (tab. 2 & 3). Integrity over the entire weld interface was evaluated by means of light optical microscopy of the non-etched embedded cross-sections. Evolved microstructure, geometric arrangement, average grain size and grain size ratio were examined by means of light optical microscopy and scanning electron microscopy of the wet etched embedded samples (tab. 4). For selected samples and spots, the chemical composition was determined using energy dispersive X-ray spectroscopy (EDX) attached to the SEM device. In order to obtain an optimized quality of the

images, molybdenum metals were finally vibra-polished by using a neutral aluminium oxide suspension (OP-AN) with a grit size of 0.02 µm.

Table 2: Preperation steps for abrasive grinding and polishing of molybdenum and TZM

Grit Size	Lubrication	Force per Sample	Duration
SiC Foil 180- 500	water	35 N	various
SiC Foil 800	water	30 N	3 x 3min
SiC Foil 1200	water	30 N	3 x 3min
SiC Foil 2000	water	30 N	3 x 3min
MD MOL DP-suspension + paste 3 μm	DP-lubricant	25 N	>20 min
MD NAP DP-suspension + paste 1 μm	DP-lubricant	20 N	>20 min

Table 3: Sample preperation steps for abrasive grinding and polishing of low-carbon steel

Grit Size	Lubrication	Force per Sample	Duration
SiC Foil 180- 1200	water	35 N	various
SiC Foil 2000	water	25 N	2 x 3min
MD MOL DP-suspension 3 μm	DP-lubricant	20 N	$\approx$ 5 min
MD NAP DP-suspension 1 μm	DP-lubricant	15 N	$\approx$ 5 min

Table 4: Composition, concentration [87] and etching time of applied etchands

	Composition	Concentration	Duration
Murakami	destilatted water H_2 O	100 m	$\approx$ 30-35 s
	potassium ferricyanide $K_3[Fe(CN)_6]$	10 g	
	potassium hydroxid KOH	10 g	
Cr m2	destilatted water H_2O	70 ml	$\approx$ 2 min
	30% hydrogen peroxide solution H_2O_2	20 ml	
	97% sulfuric acid H_2SO_4	10 ml	
Nital	ethanol C_2H_6O	100 ml	$\approx$ 10-20 s
	nitric acid HNO_3	1-10 g	

3.3.4 Mechanical Characterization

To assess the mechanical properties in longitudinal- and transverse direction of the generated friction welds, automated hardness measurements were performed on the non-etched polished cross-sections. Vickers hardness measurements were conducted according to EN ISO 6507-1:2005 with a load of 1 kp (HV1). The measured single hardness values were assigned to hardness-matrices and associated hardness heat maps were generated. Monitored hardness distribution across the entire region of interest enabled a comparison to so far in literature conducted friction welding attempts of molybdenum and the inference on materials mechanical properties.

3.4 Experimental Procedure

Multi-staged experimental procedure was designed and conducted in order to structure and simplify data analysis and obtain valuable results. The experimental procedure was split into six separated steps. The steps were (fig. 21): 1) Adaption of the friction stir welding machine, 2) feasibility study of low-carbon steel (LCS), 3) pilot study of RFW molybdenum and TZM, 4) case study of RFW molybdenum and TZM, 5) comparison of molybdenum / TZM / LCS and 6) upscale small scale to full scale).

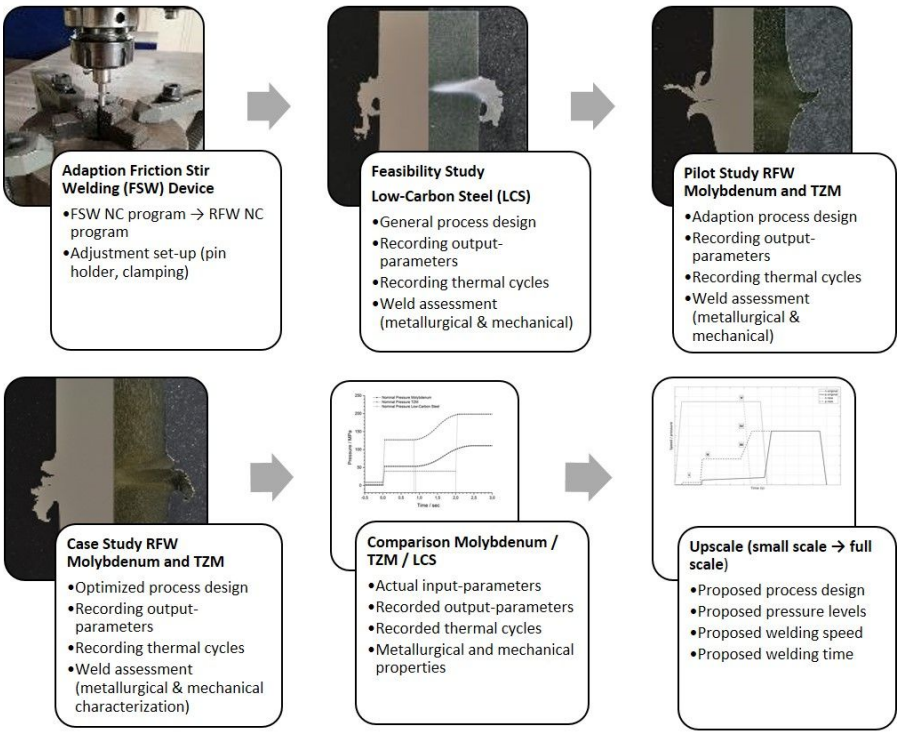

Figure 21: Seperated steps of experimental procedure rotary friction welding (RFW) of molybdenum

3.4.1 Adaption Friction Stir Welding (FSW) Device

First, the adaption of the FSW machine was needed for rotary friction welding utilization. The adjustment comprised the realization of a sufficient clamping system to prevent adverse translation and rotation of the weld specimens exposed to the heavy process loads. Designed pin-sleeves simplified the handling and plug in, and protected the FSW head from weld exposure. Further, the FSW NC program (fig. 22) was modified to illustrate every single representative weld stage of the direct drive friction welding process.

```
% home position movement
GOTO/0.0,0.0,0.0;                                   % move to home position

% zero point determination
FORGEMOVE/TOUCH,0,FORCE,0.5,RATE,12,ACCEL,100;      % touch stat. specimen F = 0.5 kN & weld head z-position = 0
DELAY/SEC,0.1;                                      % time delay t = 0.1 sec

% start position movement
FORGEMOVE/POSITION,0.2,RATE,6,ACCEL,6,RELATIVE;     % move weld head relative position z-position = 0.2 mm
DELAY/SEC,0.1;                                      % time delay t = 0.1 sec

BREAK/"ALLES PALETTI?";                             % manual confirmation

% spindle start
SPINDLE/RPM,1750,ACCEL,1500;                        % rotational speed n = 1750 rpm, acceleration 1500 rpm/s
DELAY/SEC,2.0;                                      % time delay t = 2.0 sec

% contact inititation                               % displacement controlled
FORGEMOVE/POSITION,-0.2,RATE,10,ACCEL,10,RELATIVE;  % move weld head relative position z-position = -0.2 mm
DELAY/SEC,0.1;                                      % time delay t = 0.1 sec

% friction stage                                    % hand over displacement- to force controlled
FORGECONTROL/FORCE,2.5;                             % axial friction force F = 2.5 kN
DELAY/SEC,2.0;                                      % friction time t = 2.0 sec

% forge stage
FORGECONTROL/FORCE,12.5;                            % forge force F = 12.5 kN
SPINDLE/RPM,0,ACCEL,4000;                           % spindle speed n = 0 rpm, deceleration 4000 rpm/s
DELAY/SEC,10.0;                                     % forging time t = 10.0 sec

% unload
FORGECONTROL/FORCE,0.0;                             % unload F = 0 kN
DELAY/SEC,1.0;                                      % time delay t = 1 kN
```

Figure 22: Extracted source code sections of a modified sample NC program for rotary friction welding low-carbon steel

The sample FSW NC program start initiated the overall machine movement to its manually set home position (e.g. aligned pin axes and 3 mm slit). To define the FSW head zero point, the weld head travelled downwards until the pins came in mutual contact and reached the selected force level of 0.5 kN (fig. 23a). Further, the FSW head moved 0.2 mm relative in z-axis upwards from the previous set zero point and loosened its preload. This position served as starting position for the subsequent rotary friction welding process (fig. 23b). After a manual confirmation, the FSW spindle was constantly accelerated over 2 s in order to ensure determined rotational speed. Once the operating

speed was reached, the contact of the weld specimens was initiated by moving the FSW head to $z = -0.2$ mm and displacement control was switched to force control. The actual friction stage started and previously in the NC program determined force level and friction time were applied (fig. 23c). The following stage was initiated by the instant transition from applied friction force to forging force and a simultaneous spindle stop (fig. 23d). Upon completion, applied force was unloaded and the welded specimen was removed.

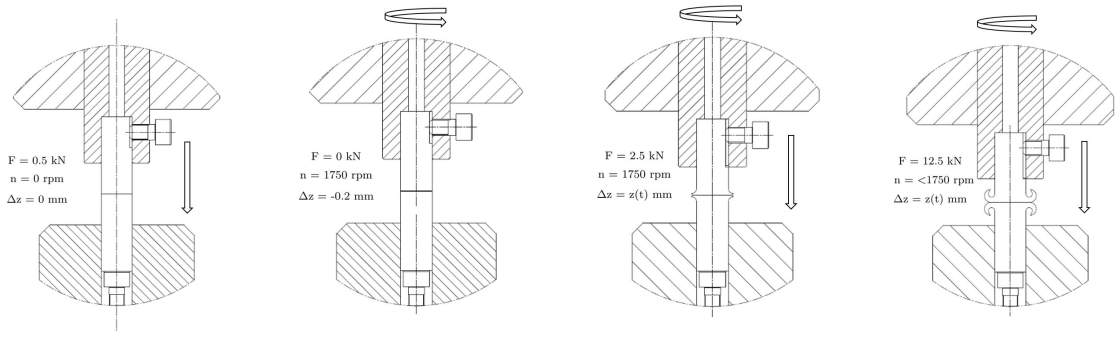

Figure 23: Schematic illustration weld stages realized by sample NC programm for low-carbon steel: (a) Zero point determination, (b) start position movement, (c) friction stage inititation and (d) forging stage inititation

Beside usually chosen input parameters (rotational speed, friction pressure, friction time, forge pressure, forging time), additional input parameters were implemented (rotational speed de-/ acceleration, pressure gradient, pressure de-/ acceleration, time delay) to fine-tune the process. It has been revealed that especially the mutual agreement of force and spindle speed in the transition stages is a key factor to success and justified the implementation of these parameters (fig. 24).

```
% friction stage
FORGECONTROL/FORCE,6.0;                          % axial friction force F = 6.0 kN
DELAY/SEC,0.85;                                  % friction time t = 0.85 sec

% forge stage
SPINDLE/RPM,0,ACCEL,4000;                        % spindle speed n = 0 rpm, deceleration 4000 rpm/s
FORGECONTROL/FORCE,12.5,RATE,7.5,ACCEL,10.0;     % forge force F = 12.5 kN, force gradient Fv = 7.5 kN/sec &
                                                   force acceleration Fa = 10 kN/s^2
DELAY/SEC,10.0;                                  % forging time t = 10.0 sec
```

Figure 24: Extracted source code sections of modified sample NC programm for rotary friction welding molybdenum metals

3.4.2 Capability Study Low-Carbon Steel (LCS)

Based on the established best practice process design, the machine capability for rotary friction welding was examined by means of reference welding Ø9 mm low-carbon steel pins. First input parameters were set regarding the DVS guideline [86] for relative velocity (10 m/s) and applied pressure levels (40/200 MPa). However, the machine capability for rotational speed (3200 rpm) and weld specimens circumference (Ø9 mm) limited the maximum obtainable relative velocity to 1.5 m/s. Conducted preliminary studies identified the lower limit of a potential process window (rotational speed $n = 1250$ rpm, friction pressure $p_{friction} = 40$ MPa and friction time $t_{friction} = 2$ s), and gave a rough estimation of suitable parameter configurations. In order to identify the basic relationship between input parameters and their effect on the process and its output, the Design of Experiments (DoE) approach was chosen (cause and effect relationship). To keep the workload manageable, the subsequent Full Factorial Design (FFD) focused on the adjustable factors k: 1) Rotational speed n, 2) friction pressure $p_{friction}$ and 3) friction time t_{time} and target values: 1) Total upset z and 2) max. upset-rate $\dot{z}$. Applied forging pressure (200 MPa), forging time (10 s), rotational speed deceleration (4000 rpm/s) were set constant. Factor combination and levels for the 2^3 FFD are shown in table 5. Statistical evaluation of the results took place by means of *Minitab 16.1.1* software.

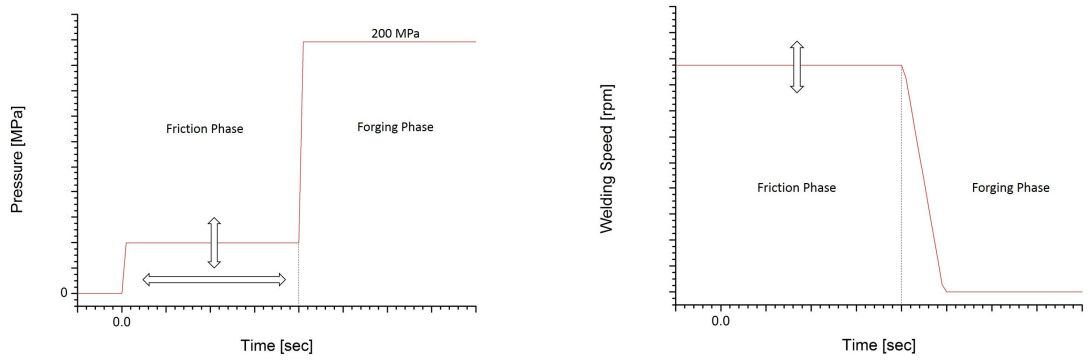

(a) (b)

Figure 25: Nominal input parameters: (a) Pressure and (b) welding speed for DoE low-carbon steel

Table 5: Factor levels and combination of FFD for reference low-carbon steel

Factor	Low Level	High Level
Rotational speed n [rpm]	1250	1750
Friction pressure $p_{friction}$ [MPa]	40	60
Friction time $t_{friction}$ [s]	2.0	2.5

In addition to the first statistical insight, selected generated joints were further in-depth characterized to describe the material behavior during the single stages of friction welding. Extended welding experiments with increased friction time (2.0 s, 2.5 s, and 3.0 s) were conducted in order to investigate and identify essential correlations in the passed equilibrium stage. Plasticization history and technical information were determined based on the recorded and derived output variables. Joint quality was evaluated by the investigation of the microstructure and mechanical characterization.

3.4.3 Pilot Study RFW Molybdenum and TZM

Ensuing from literature [54, 67, 69], first rough input parameters (e.g. pressure levels 60/200 MPa) were estimated for the so far established two stage direct drive friction welding process. A similar approach like for low-carbon steel should be used to ascertain molybdenum's plasticization behavior. However, the pilot study revealed that molybdenum's intrinsic properties require a general re-design of the process itself. The process design was successively iteratively adjusted considering a preceding in-situ pre-heating stage and a mutual arrangement of applied pressure and spindle speed in the transition stage. The implemented preceding in-situ preheating stage elevated the operating temperatures ($\approx$ 350 °C), countervailed the material's brittleness at room temperature and guaranteed sufficient toughness at the initial welding cycle. Beside commonly used input parameters, friction pressure $p_{friction}$, friction time $t_{friction}$, forge pressure p_{forge}, forging time t_{forge}, and rotational speed n additionally adjusted parameters were: Spindle deceleration $\dot{n}$, pressure acceleration $\ddot{p}$ to facilitate a pressure gradient $\dot{p}$ in the transition zone. This enabled a fully defined and controlled transition from friction into forging stage.

3.4.4 Case Study RFW Molybdenum and TZM

The revised process design was applied for Ø12 mm molybdenum and Ø9 mm TZM weld specimens (fig. 26). The preceding in-situ preheating by friction at low pressure levels ($<$ 10 MPa) at operating rotational speed resulted in a stationary temperature distribution within the weld specimens without any significant plastic deformation before the actual weld cycle started. Further, the actual welding process was started and controlled by the constantly set input parameters: Friction time $t_{friction}$ (0.80 s), forging time t_{forge} (10 s), spindle deceleration $\dot{n}$ (4000 rpm/s), pressure acceleration $\ddot{p}$ (10 kN/s^2) and pressure gradient $\dot{p}$ (7.5 kN/s) in the transition zone. The forge condition, that is, the transition from friction to forging phase, was now fully defined by: 1) The acceleration $\ddot{p}$ of the pressure to its selected gradient, 2) the rate $\dot{p}$ of pressure increase from friction to forge level, and 3) the spindle deceleration $\dot{n}$ to spindle stop. To obtain a variety in displacement within given machine capability (total upset <16 mm), a variable rotational speed (tab. 6) was selected to adjust the power input. To illustrate similar upset courses compared to commercially pure molybdenum, TZM required a nearly two times higher friction and forge pressure.

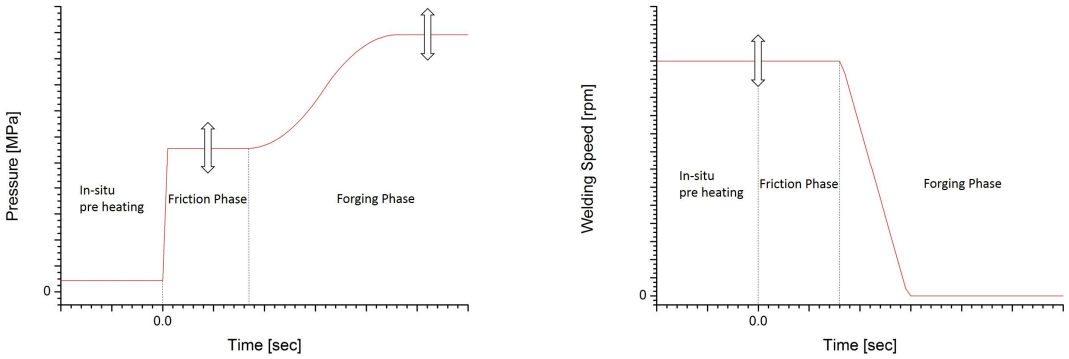

(a) (b)

Figure 26: Nominal input parameters: (a) Pressure and (b) welding speed for the case study molybdenum and TZM

Table 6: Variable input parameters and combination for molybdenum and TZM

Variable Input Parameter	Molybdenum	TZM
	2500	2500
Rotational speed n [rpm]	2600	2600
	2750	2750
Friction pressure $p_{friction}$ [MPa]	53	110
Forge pressure p_{forge} [MPa]	110	200

Generated molybdenum and TZM joints were further in-depth characterized to describe material's behavior during friction welding. Plasticization history and technical information were determined based on recorded and derived output variables. Joint qualities were evaluated by means of microstructure and mechanical characterization.

3.4.5 Comparison Molybdenum and TZM to LCS

Based on the results, the general process design and required input parameters of molybdenum metals to the reference low-carbon steel were opposed. Materials displacement histories and representative upset-rates were discussed, and linked to recorded thermal cycles and the material's thermophysical properties.

3.4.6 Upscale

Based on the input parameters and derived technical information from the previous established general process of the small cross-section's experiment, an adjustment of the process design for large cross-sections [68] was recommended.

4 Results and Discussion

The results and the discussion of the previously conducted experiments are arranged in the same order as in the experimental procedure section.

4.1 Capability Study Low-Carbon Steel (LCS)

This subchapter provides selected results of rotary friction welding of a reference low-carbon steel. A general machine capability for direct drive friction welding was proven and basic influence of adjustable input parameters on the response within the different weld stages was identified. Further, the representatively evolved microstructure was characterized by LOM and related mechanical properties were discussed in detail.

4.1.1 Design of Experiments

In order to determine the individual effects of selected input parameters that could affect the output result, a Design of Experiments (DoE) approach was chosen. The conducted Full Factorial Design (FFD) focused on the adjustable factors: 1) Rotational speed, 2) friction pressure, and 3) friction time and their influence on 1) the total upset and the 2) maximum upset-rate. The applied factor levels and recorded target values are scheduled in Tab. 5 and are attached in the appendix. The minimum process requirements for welding were evaluated by the means of pilot studies and the selected parameter configuration (n = 1250 rpm, $p_{friction}$ = 40 MPa and $t_{friction}$ = 2 s) served as corner point providing the lowest amount of weld energy input.

The obtained data was statistically evaluated, analyzed and visualized. The plotted pareto chart and the main effect plot visualize the effect of the selected factor and factor levels on the target values. The pareto chart reveals that of the three varied factors in conducted experiment, the rotational speed n and friction pressure $p_{friction}$ have the statistically most significant influence on the total upset result (fig. 27a).

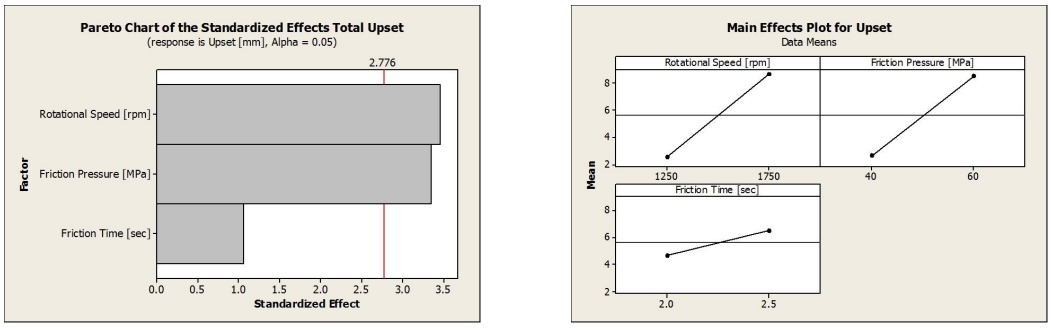

(a) (b)

Figure 27: Design of Experiments feasibilty study low-carbon steel: (a) Pareto chart and (b) main effects plot for total upset

To examine the differences between selected factors, the main effects plot was used (fig. 27b). The main effects plot visualizes the response for each factor level connected by a line. All the selected input factors show a positive sign and main effect on the response. That implies that the average response is higher at a higher level rather than a low level of the parameter setting. Considering the analyse's main effect's magnitude, the single strength of the effect for the selected input factors differs. The steeper the slope of the line, the greater is the impact of the main effect. Consequently, the more horizontal line for friction time indicates that there is nearly no effect, which means that each level of this factor affects the response in the similar way. While the steep lines for rotational speed and friction pressure indicate a predominant main effect and that different levels affect the response significantly.

Similar to previous statistical analysis, an evaluation was conducted to determine the influence of adjustable selected factors on the maximum upset-rate result. The analysis reveals an equal influence of the factors on the selected response compared to the total upset result (fig. 28). To conclude, it is likely that there is a direct correlation between total upset and maximum upset-rate within the conducted experiment.

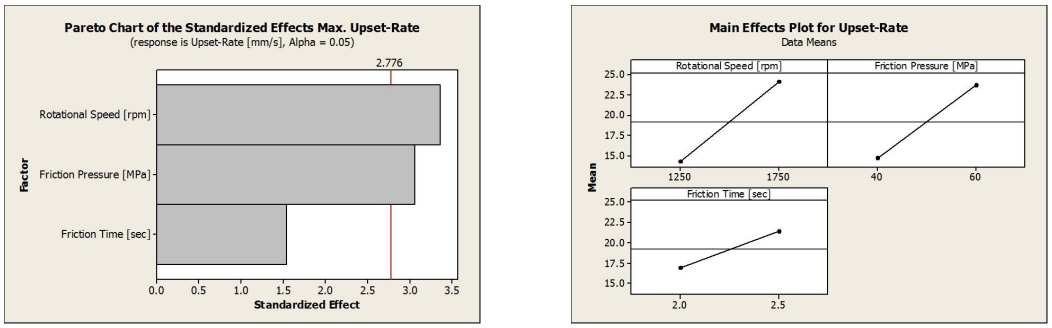

(a) (b)

Figure 28: Design of Experiments feasibilty study low-carbon steel: (a) Pareto chart and (b) main effects plot for max. upset-rate

In addition to the first statistical insight, a selected representative upset and upset-rate course shall be used to interpret the results (fig. 29). Within the given process design and experiment, the total upset ($z = z_{friction} + z_{forge}$) is mainly determined by the amount of forge upset ($z \approx z_{forge}$). The applied forge condition might explain the observed results. The transition stage is initiated by starting spindle deceleration to final spindle stop and is accompanied by an instant increase of the load to forge pressure level. However, the maximum spindle deceleration is restricted to the system's mechanic inertia and requires at least a minimum duration, towards the hydraulic cylinder and the initial applied actual forge pressure. The instable coordination of the actual forge pressure in relation to the current spindle speed resulted in an exposure to maximum applicable pressure at a rotational speed close to the maximum operating speed. The so suddenly introduced power input resulted a further upsetting and resulted in maximum upset-rates

initially after the forging phase start. The previously significantly attributed rotational speed and friction pressure encourage the plasticization behavior during processing. An increased friction pressure minimizes the difference to maximum applied forge pressure, while an increased rotational speed directly increases the introduced power input level and extends the spindle deceleration time.

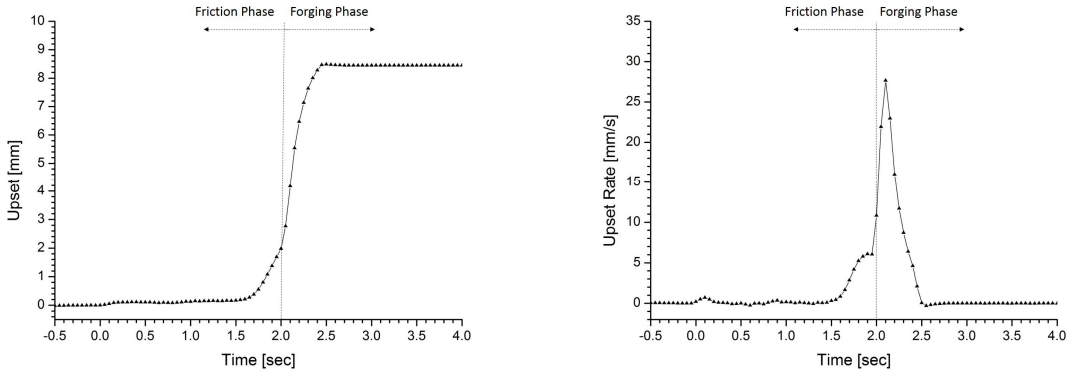

(a) (b)

Figure 29: Representative (a) upset and (b) upset-rate course of Design of Experiments low-carbon steel ($n = 1250$ rpm, $p_{friction} = 40$ MPa and $t_{friction} = 2$ s)

The Design of Experiments (DoE) approach and results for total upset and maximum upset-rate mainly reflected the effect of adjustable input factors on the response in the forging phase. Their effect in the early stage of the process on the response is almost excluded and a more appropriate method is needed. In order to describe the material's behavior in a more detailed way, considering every single weld stage and to define the machine's general capability for friction welding, the analysis' focus is shifted to representatively recorded and derived output parameter courses of selected parameter configurations.

4.1.2 Recorded and Derived Output Parameters

The selected parameter configuration ($n = 1750$ rpm, $p_{friction} = 40$ MPa and $t_{friction} = 2$ s) and recorded/derived output parameter courses serve as a reference for DDFW low-carbon steel. Subsequent analysis takes place on the selected configuration and comprises: 1) Machine capability and process accuracy, 2) upset behavior and 3) technical information. The gathered results are discussed in detail.

To determine the machine capability and process accuracy, the actual and nominal input parameter courses (axial pressure, welding speed) are opposed (fig. 30). The logged actual pressure reveals a maximum deviation from the nominal value at the initial friction and forging phase. With the incremental duration of the weld phases, the discrepancy

between actual and nominal pressure is minimized. Unlike the applied welding speed, no significant deviation between the actual and nominal value is determined. However, the actual spindle deceleration start initiating the forging phase is time-delayed in the range of one measurement point (50 µs).

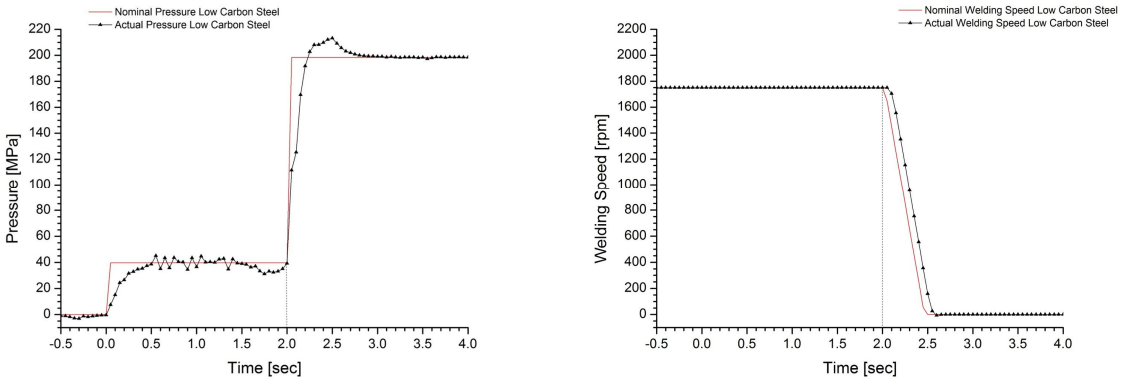

(a) (b)

Figure 30: Comparison of nominal and actual input parameters: (a) Pressure and (b) welding speed examination of the machine capability of low-carbon steel

The process accuracy is evaluated by the means of the relative and the overall mean relative error (fig. 31) and is derived from nominal and actual applied input parameter courses (eq. 3 and 4).

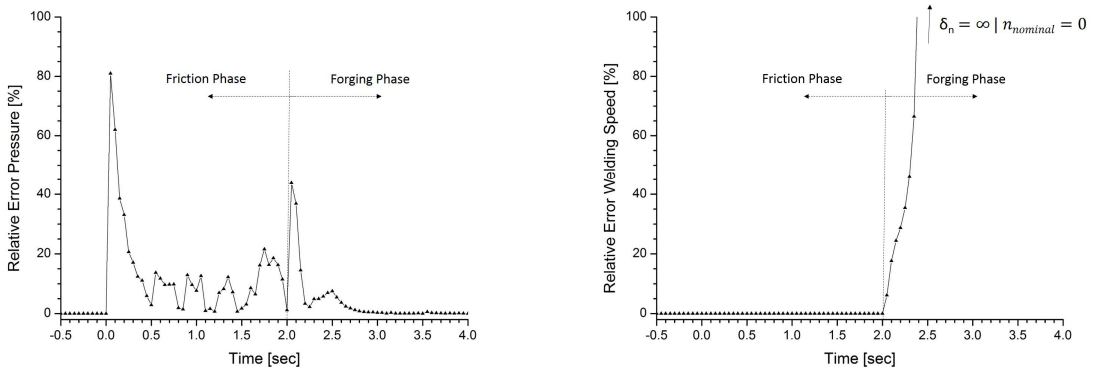

(a) (b)

Figure 31: Comparison of relative errors: (a) Pressure and (b) welding speed examination of the machine capability of low-carbon steel

The maximum relative errors for pressure instantly occur after the first measurement points in the friction and forging phase (max. $\delta_{p,friction} = 81.0\%$ and max. $\delta_{p,forge} =$

43.8%). This means that the specified target value (friction/forge pressure) cannot be achieved within a certain relative short time (50 μs), and needs at least a minimum time period (<0.5 s) to recover auto control and process accuracy. The overall mean relative errors for pressure are $\overline{\delta}_{\mathrm{p,friction}} = 13.3\%$ and $\overline{\delta}_{\mathrm{p,forge}} \rightarrow 0\% \mid t_{forge} = 10$ s. Unlike the relative errors for welding speed, there is no significant error over the entire friction phase detected ($\overline{\delta}_{\mathrm{n,friction}} = 0.02\%$). Though the time-delay in spindle deceleration start results in a steady increase of the relative error coupled with the continuous decrease of nominal spindle speed ($\delta_{n,forge} \rightarrow \infty \mid n_{nominal} = 0$). Regarding the time shifted actual and nominal spindle deceleration start, the plotted input parameter courses of welding speed are completely congruent ($\overline{\delta}_{\mathrm{n,forge}} \rightarrow 0 \mid nominal_{\ \mathrm{i}} = actual_{\ \mathrm{i-1}}$).

To describe the representative plasticization behavior of low-carbon steels over the entire weld cycle, the deformation history and ascertain derived displacement-rate are visualized (fig. 32). Due to the varying upsetting within the different weld stages, the analysis needs to be divided into the separated friction and forging phase. In the friction phase, within the first $\approx$ 1.5 s the participating weld specimens come into contact and rub against each other. The asperities are worn down and the flattened surfaces provide a full surface contact without any notable plastic deformation. In this stage of the process, the participating low-carbon steel pins are heated up mainly by friction. The steady increase of the weld interface temperature leads to a local material softening and lower the local shear yield strength τ_y. After >1.5 s, the applied loading condition exceeds the local shear strength and the material starts to plastically deform. Henceforward, the heat generation is not only represented by the friction heat but also by plastic deformation. The upset-rate increases and stabilizes close to the end of the friction phase ($\dot{z} = 6.01$ mm/s), the related upset ("burn-off") course shows a steady growth and indicates the start of the characteristic equilibrium stage.

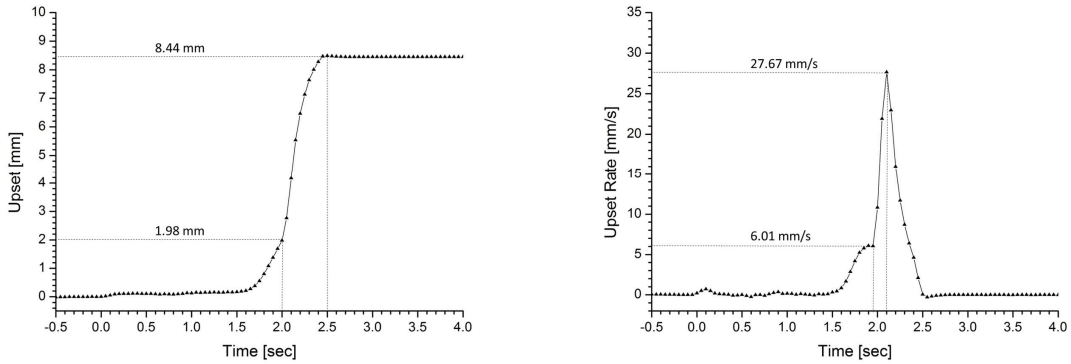

(a) (b)

Figure 32: Recorded (a) upset and acertained (b) upset rate examination of the machine capability of low-carbon steel

The subsequent initiation of the forging phase facilitates the plastic deformation, and results in a maximum upset-rate (27.67 mm/s) shortly after the spindle deceleration start and simultaneously applied forge pressure. With the incremental duration of the spindle deceleration, the maintained power input and therefore the upset-rate drops. Within the conducted experiment and recommended applied technique ("forging into the turning spindle"), the total upset (z = 8.44 mm) of the weld specimen is mainly determined by the forge upset (z_{forge} = 6.46 mm).

In order to provide technical information of the process in combination with a certain material, the torque in loaded/unloaded condition and the derived power input are of interest (fig. 33). The marked area between the loaded and unloaded torque curve represents the nominal torque input and is utilized for calculating the power input. In the early stage of the friction phase (<1.5 s) where no significant plastic deformation takes place, a lower nominal torque and therefore friction shear stress ($T \propto \tau_{fric}$) is recorded. This might be explained by the presence of microscopic irregularities on the weld interfaces. The inconsistent surface roughness results in the contact of the present asperities and reduces the real contact area to a fraction of the sliding condition ($\tau_{fric} < \tau_y$). In this stage, the frictional shear stress and therefore generated heat input can be described by Coulomb's friction law ($\tau_{fric} = \mu \cdot p$) and is dependent on the applied normal pressure p and the friction coefficient μ. However, the friction coefficient is a non-constant value and its value depends on a variety of influencing factors such as material, temperature, velocity or pressure. Actual friction coefficients in friction welding and their validity is still discussed in literature.

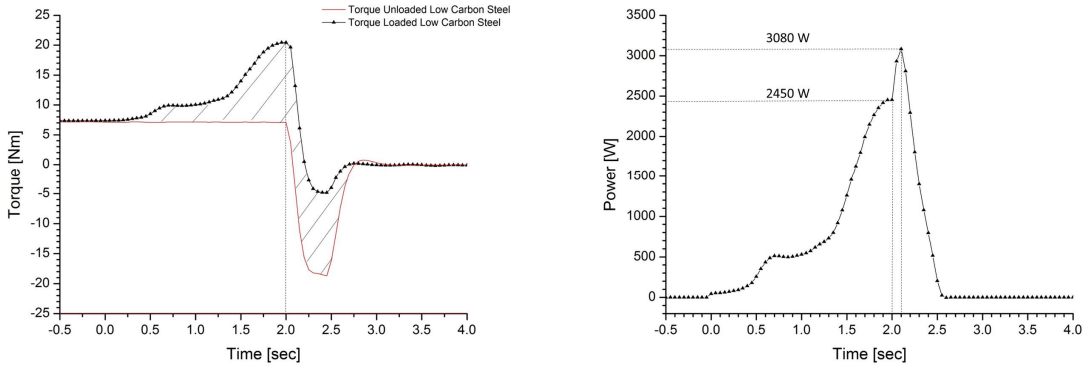

(a) (b)

Figure 33: Recorded (a) loaded/unloaded torque and acertained (b) power input examination of the machine capability of low-carbon steel

During the ongoing process, the surrounding weld interface area is heated up and the critical local shear strength is lowered. The real contact area is identical to the apparent contact area and the sticking condition is fulfilled ($\tau_{fric} = \tau_y$). Material plasticization is initiated and the nominal torque rises to a maximum peak and is stabilized close to the

end of the friction phase (fig. 33a). The initial nominal torque and therefore power input (2450 W) lead to a maximum upset-rate of 6.01 mm/s and is the limiting factor for plasticization in the friction phase. The subsequent initiated forging phase results in a maximum "power burst" (3080 W) shortly after the spindle starts to decelerate and correlates with the corresponding overall maximum upset-rate (27.67 mm/s) of the process.

Torque courses in representative literature [73] slightly differ to the recorded one. In literature, the initial torque peak is attested to even out the weld interface surfaces without any axial shortening. Afterwards, the torque starts to fall and drops to the level of the equilibrium torque value. This stage of the process is accompanied by the start of upsetting. On the contrary, in the conducted experiments, an increase and stabilization of the torque at its maximum peak at a simultaneous axial shortening is observed. In order to clearly describe the friction phase and its containing equilibrium stage, the friction phase was isolated and additional experiments with extended friction time (2.0 s, 2.5 s and 3.0 s) were conducted.

The additionally conducted experiments reveal nearly completely congruent nominal torque curves within the first 2.0 s and prove the high reproducibility of the process (fig. 34a). With incremental duration of the friction time (>2.0 s), the initial maximum torque peak starts to decrease and stabilizes at a lower level (equilibrium level). Further, the corresponding power input is reduced and the upset-rate drops to 3.85 mm/s (fig. 34b) within the starting equilibrium stage and regulates the process. While the initial maximum torque peak determines the maximum upset-rate, the equilibrium torque determines the quasi-steady-state upset-rate within the friction phase (fig. 34).

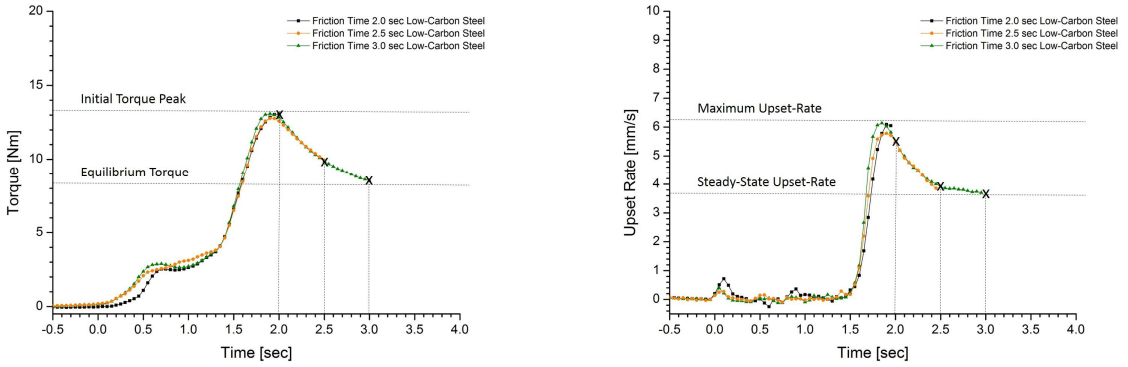

(a) (b)

Figure 34: Derived (a) nominal torque and (b) upset-rate examination of the equilibrium stage of low-carbon steel

Based on the previously derived welding parameters (nominal torque, power input), the total energy input over time and the upset over total energy input are plotted in fig. 35. Concerning the upset behavior, the total weld energy input (2590 J) is mainly determined by the amount generated in the friction phase (1740 J) (fig. 35a). Almost 1000 J of the friction phase's weld energy is needed for heat dissipation and to heat-up the weld specimens before actual plasticization takes place. The ratio of upset to energy (gradient) is a variable (fig. 35b) and obviously also depends on the operating condition. An application of heavier loads (i.e. forge pressure) leads to more plasticized material at a similar provided energy input. Therefore, the only indication of technical information (e.g. total energy) without levels considering actual process conditions (e.g. pressure levels) is not sufficient enough and additional information such as forging condition or power input course is needed.

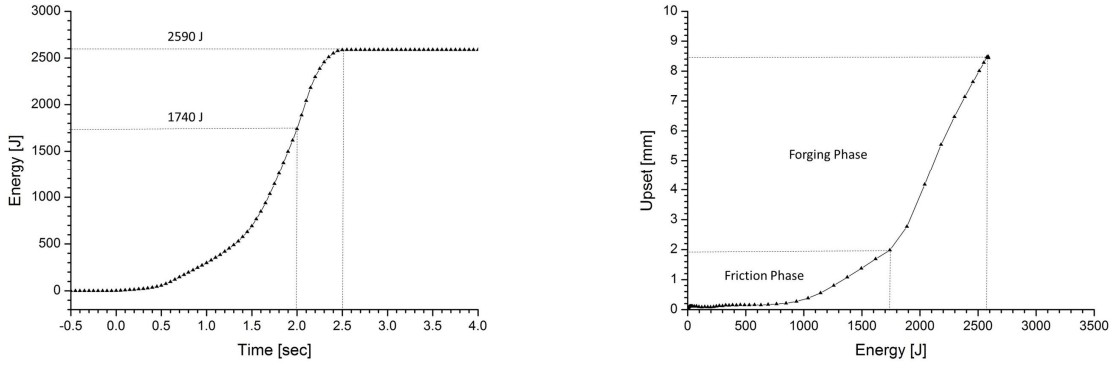

(a) (b)

Figure 35: Acertained (a) energy input and (b) upset behavior examination of the machine capability of low-carbon steel

4.1.3 Assessment of the Weld Specimens

Visual Inspection Visual inspection of the welded pins reveals an atypical flash formation compared to literature (fig. 37). The formed flash is nearly rotationally symmetrical, though the flash of the previously rotating pin interleaves the fixed one. In the conducted experiments it has been observed that the forging condition and therefore the main material displacement defines the visual appearance of the finally formed flash. In addition, the high nominal torque during processing results in clamping marks on the fixed weld pin. The observed annealing colors are restricted to a close area next to the weld interface and confirm the concentrated heat input of the process.

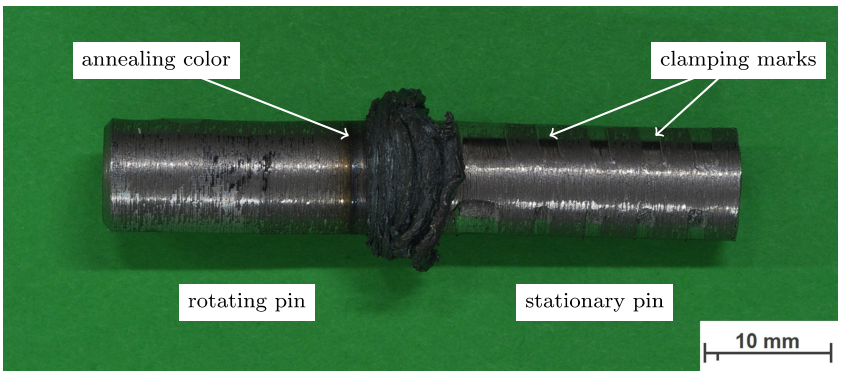

Figure 36: As-welded RFW low-carbon steel specimen

In industrial applications, the well-established theory is that the visual appearance of the flash is directly related to the "joint quality" is widely spread. Therefore, the integrity and further the microstructure of the bond is characterized by examination of the region of interest. The embedded, trimmed, and polished longitudinal cross-section reveals a proper bonding over the weld interface without any presence of welding defects (fig. 37a). However, a small parallel misalignment (<0.5 mm) of the previously rotating to the stationary weld pin axes is observed.

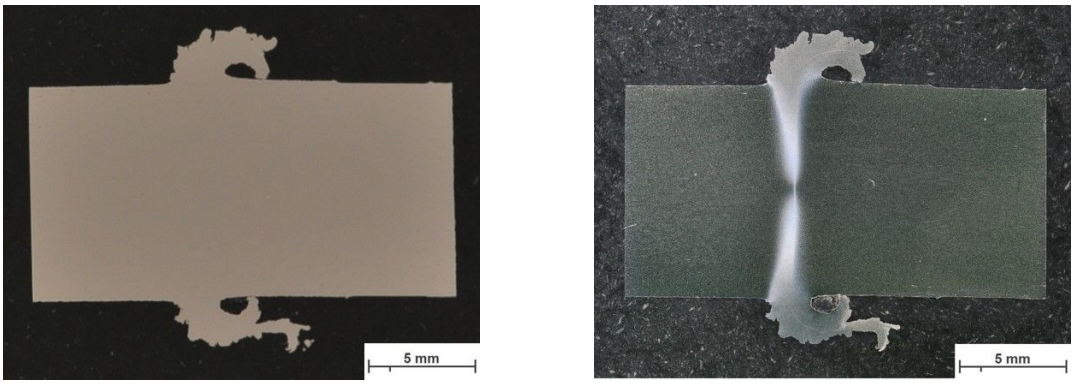

(a) (b)

Figure 37: (a) Polished unetched and (b) etched [3% nital] cross-section of RFW low-carbon steel

Microstructure Characterisation The etched cross-section reveals a radial influence of the evolved microstructure (fig. 37b), with a maximum HAZ width at the outer circumference of the weld interface and a minimum HAZ width at the weld interface center. Geometric distribution of the formed microstructure correlates with a basic theoretical heat generation model (fig. 38) across the weld interface and points out the lower heat generation (temperature) in the center zone due to the missing relative motion of the weld specimens.

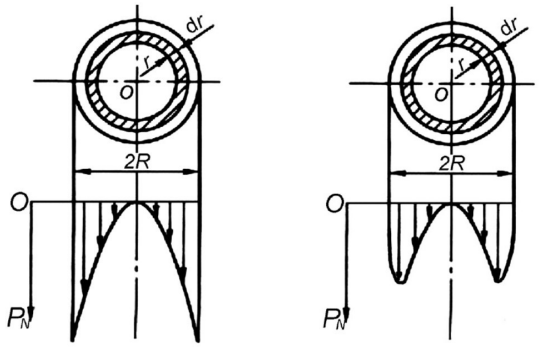

(a) (b)

Figure 38: (a) Basic theoretical heat generation and (b) experimental heat generation across the weld interface [88]

The three-dimensional temperature field within the weld specimens may be described by Fourier's law (heat equation) and is therefore determined by the material's thermo-physical properties thermal conductivity λ, thermal capacity c, and time. However, the actual welding cycle and cooling time do not provide a sufficient level of activation energy (temperature, time) in the surrounding area next to the weld interface center to enable recovery/recrystallization. As shown in fig. 39a, the highly deformed and dislocated bond line structure is surrounded by thermo-mechanically deformed and in transverse direction elongated realigned ferrite grains. Towards the circumference of the weld interface (fig. 39b), where no actual bond line structure is clearly discernible and the weld region is in a wide range (>500 μm) recovered/recrystallized.

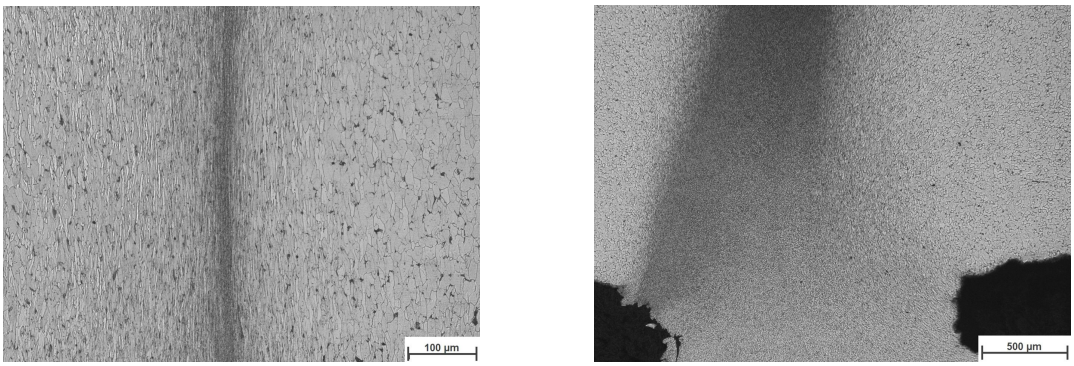

(a) (b)

Figure 39: Etched (a) weld interface center [3% nital, 200x magnification] and (b) weld interface circumference [3% nital, 50x magnification] cross-section of RFW low-carbon steel

In practice, the problem of insufficient heat generation in the centre zone is well known. Considering the related evolved microstructure, the established guidelines [70] for IFW recommend a higher relative velocity or lower pressure. However, due to weld specimens

geometry (Ø9 mm) and the machine capability (max. 3200 rpm), the maximum relative velocity is restricted and a minimum pressure level is needed to provide a sufficient power input for welding.

A closer look at the evolved microstructure reveals the in literature [73] mentioned formation of representative weld sections (fig. 40). The transition from the undeformed zone (IV) to the fully plasticized zone (II) is accompanied by the partly deformed zone/TMAZ (III) with a width of approximately 450 μm.

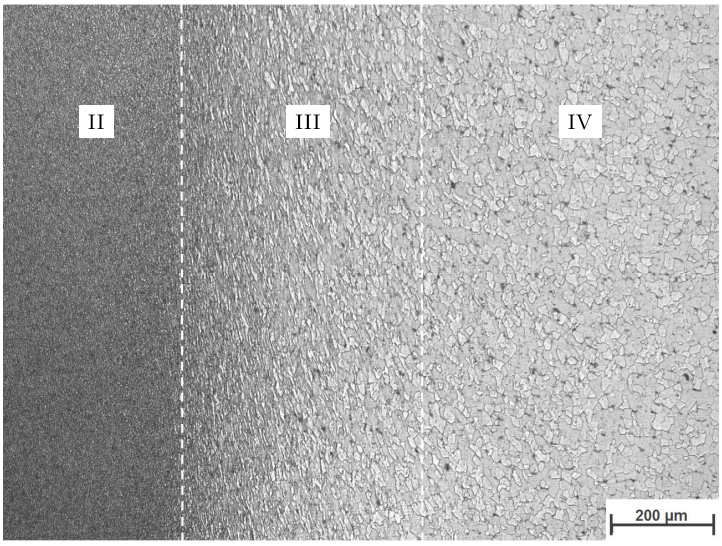

Figure 40: Weld cross-sections of an etched [3% nital, 100x magnifi.] RFW low-carbon steel

During processing, the fully plasticized zone (II) is exposed to a considerable amount of plastic flow and high temperature. The occurring dynamic recovery/recrystallization results in an equiaxed, very fine grained microstructure (fig. 41a). Though a precise determination of the average grain size is not possible, the by light optical microscopy (maximum magnification 1000x) examined grains are too small for the provided ASTM maximum G10 method and a more sophisticated method (e.g. by SEM or EBSD) is needed. With increasing distance to the weld interface, the microstructure is exposed to lower temperature, strain rate and plastic deformation. This results in a coarsened, deformed microstructure (fig. 41b). General visual appearance and aspect ratio of the grains change over the width of the partly deformed zone (III) (fig. 41c) and end up in the undeformed parent microstructure (IV) (fig. 41d).

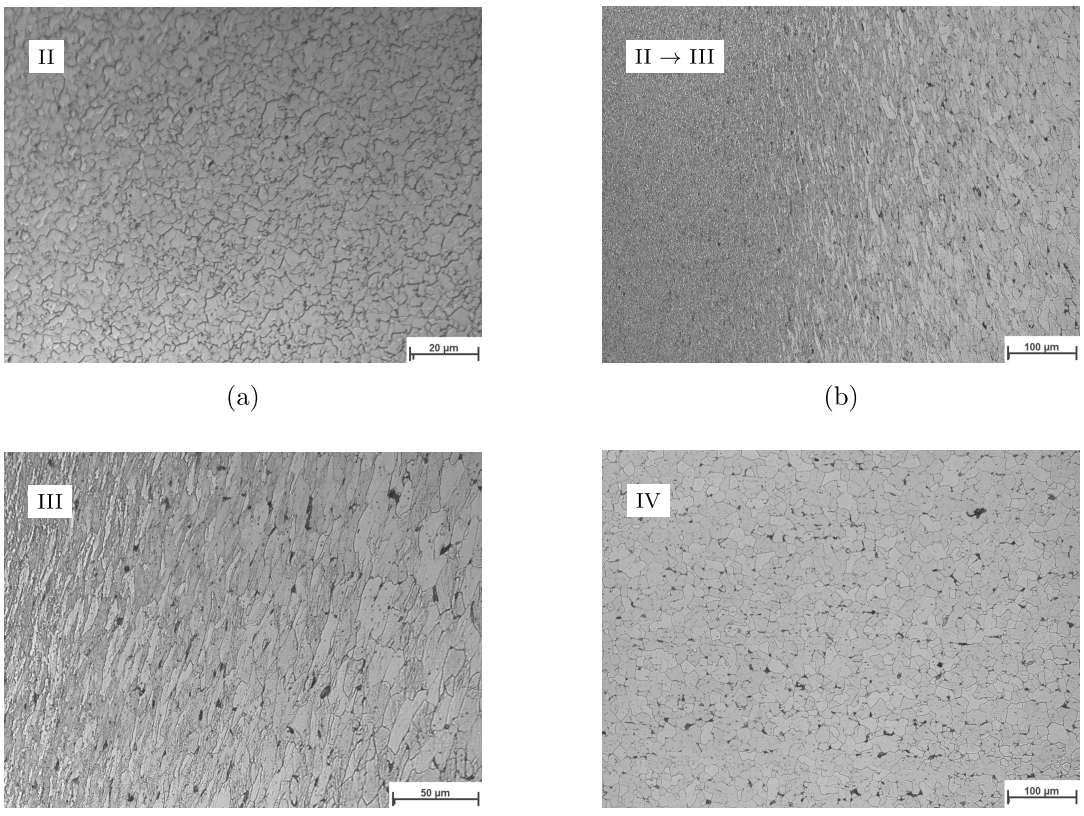

Figure 41: Etched (a) fully plasticized zone [3% nital, 1000x magnifi.], (b) transition zone [3% nital, 200x magnifi.], (c) partially deformed zone [3% nital, 500x magnifi.] and (d) undeformed zone [3% nital, 200x magnifi.] of RFW low-carbon steel

Mechanical Characterisation The evolution of the microstructure is also reflected by non-uniform mechanical properties. Mechanical properties are characterized by Vickers hardness HV1 and hardness is measured in transverse and longitudinal direction. The evolved hardness distribution is visualized by the means of a generated hardness map and superimposed with the etched cross-section (fig. 42). The hardness of the joint steadily increases from the unaffected parent metal (175 ± 12 HV1) toward the contact zone. Highest average (265 ± 45 HV1) and maximum (352 HV1) hardness value are measured within the fine grained contact and fully plasticized zone. During friction welding, additional strengthening mechanisms such as phase transformation hardening, work hardening or grain boundary strengthening may take place and improve the material's mechanical properties. Considering the specific location of the maximum values and the Hall-Petch relationship, most reasonable and dominant one might be grain boundary strengthening.

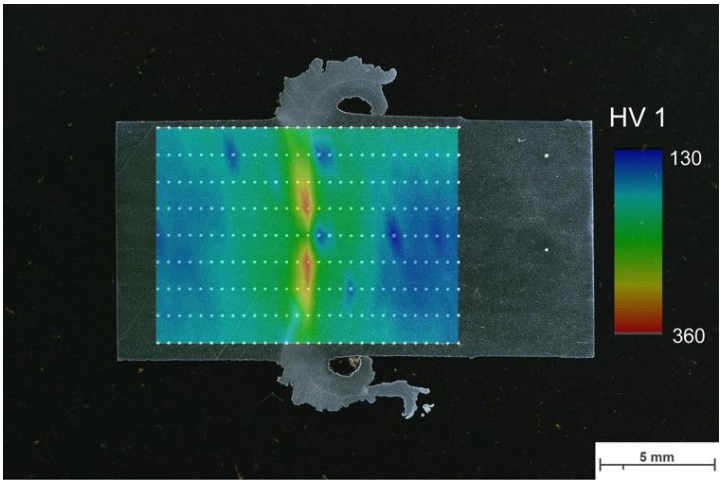

Figure 42: Hardness map and distribution RFW low-carbon steel

Table 7: Hardness values for representative weld sections RFW low-carbon steel

Weld Section	Average Hardness [HV1]	Standard Deviation Hardness [HV1]
Fully plasticized zone	265	± 45
Partially deformed zone	226	± 32
Undeformed zone	198	± 14
Base material	174	± 12

4.2 Pilot Study RFW Molybdenum and TZM

This subchapter provides selected results of the pilot study of rotary friction welding of molybdenum. Molybdenum's unique properties are a challenge for direct drive friction welding and the occurring problems are presented. It has been revealed that a general re-design of the so far established two-level process is needed in order to successfully join molybdenum and its alloys.

4.2.1 Rupture Friction Phase Inititation

According to literature [54, 67, 69] and the substantial knowledge of welding reference low-carbon steel, first parameter configurations (e.g. $n = 2500$ rpm, $p_{friction} = 60$ MPa, $t_{friction} = 3$ s and $p_{forge} = 200$ MPa) were estimated for the two level process design (fig. 48). Generally, a slightly increased friction pressure and welding speed were applied considering molybdenum's high-temperature strength and to compensate the previously mentioned missing heat generation within the weld interface center. A to the reference low-carbon steel similar experimental approach, including DoE and single weld specimen analysis, was planned in order to study the material's plasticization behavior during processing and to determine technical information. However, the first conducted molybdenum welding trials revealed a limited weldability of molybdenum and further considerations (e.g. room-temperature brittleness) need to be taken into account.

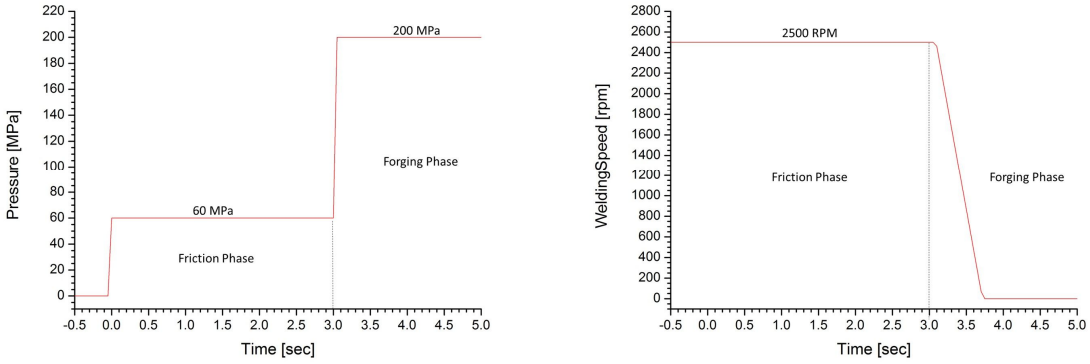

(a) (b)

Figure 43: Nominal input parameters: (a) Pressure and (b) welding speed pilot study RFW molybdenum – rupture friction phase inititation

In the first experiment immediately after initiating the friction phase and before the actual welding phase took place, the process had to be manually aborted because the rotating molybdenum pin fractured and lost its load carrying capacity. An evaluation of the recorded data revealed the approximate time of rupture ($t_{fracture}$ =0.2–0.3 s) and the ascertain loading conditions ($p_{fracture} = 55$ MPa, $T_{fracture} = 7$ Nm). In relation to the

reference low-carbon steel and considering molybdenum's strength, the material fracture took place at moderate loading condition close to room temperature.

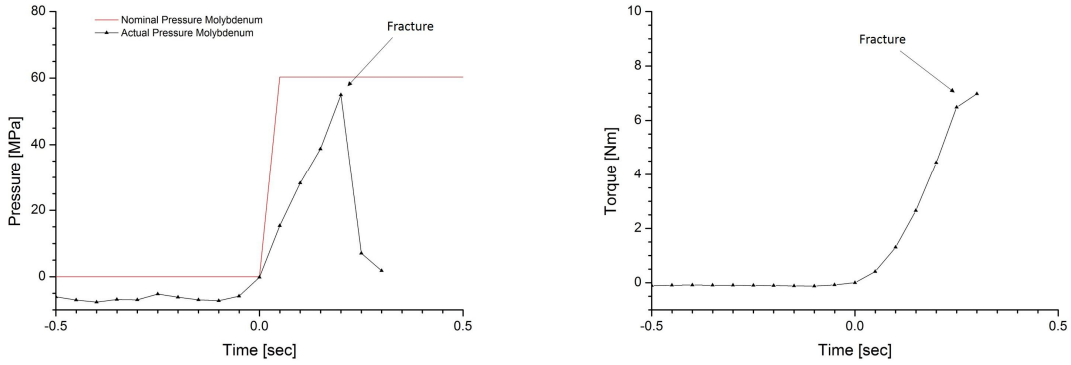

(a) (b)

Figure 44: Recorded (a) actual pressure and (b) torque pilot study RFW molybdenum – rupture friction phase inititation

Visual inspection of the weld specimens reveals a transversely as well as a longitudinally orientated fracture face. It is assumed that crack initiation started at the location providing the highest stress concentration (notch root) (fig. 45). Further, the absence of annealing colors in the region close to the fracture faces indicates a temperature below 400 °C and thus the material's DBTT. The local circumstances (stress concentration, multiaxiality of the loading, high loading rate, temperature) facilitated the fracture and the material did not provide a sufficient level of ductility at the operating temperature.

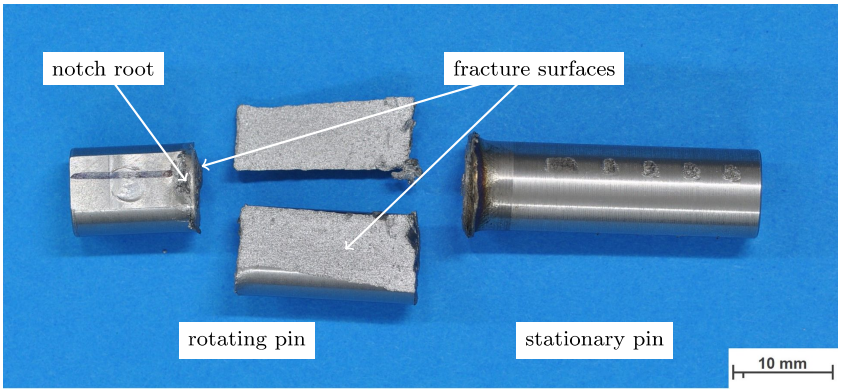

Figure 45: Ruptured molybdenum specimen of pilot study RFW molybdenum – rupture friction phase inititation

Stereomicroscopy of the transverse and longitudinal fracture faces reveal a smooth, featureless, and shiny crystalline appearance of the surfaces, where obviously plastic

deformation is strongly limited. In order to identify the actual brittle fracture mode (intergranular or transgranular), subsequent fractography was conducted by the means of scanning electron microscopy on the trasversely ruptured sample. The provided depth of sharpness ensures the explicit identification of characteristic patterns of the fracture faces and infers the actual failure mechanism.

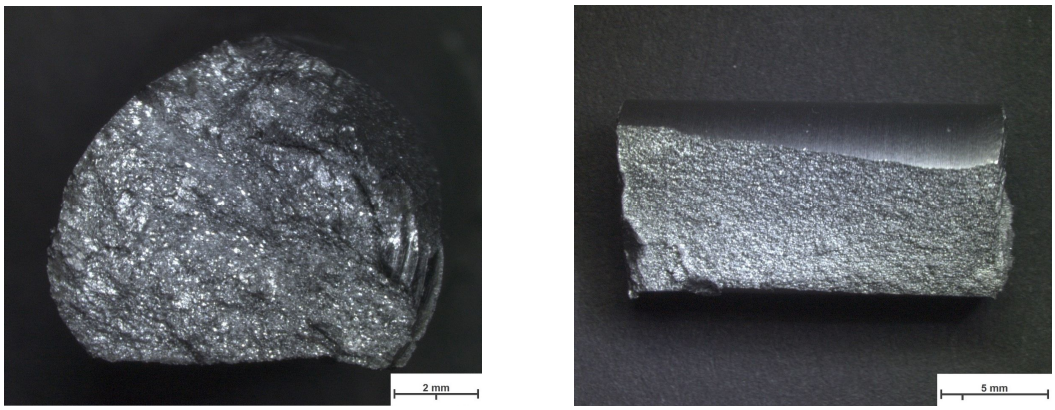

(a) (b)

Figure 46: Stereomicroscopy of the (a) rotating specimen transverse fracture face [12x magnification] and (b) longitudinal fracture face [6x magnification]

A fractography of the ruptured transverse fracture surface confirms the previously mentioned assumption of brittle failure. Scanning electron microscopy shows a typical fully transgranular morphology. The fracture cracks passed though the grains and resulted in a faceted fracture surface due to the different orientation of the cleavage planes.

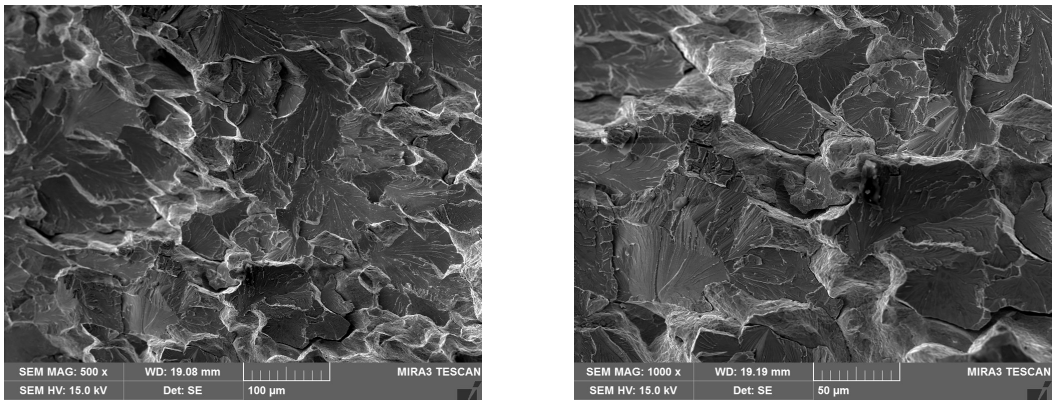

(a) (b)

Figure 47: Scanning electron microscopy of the rotating specimen (a) transverse fracture face [1000x magnification] and (b) transverse fracture face [2000x magnification]

The material's brittleness at room temperature ($T/T_m \approx 0.1$) complicates the actual process initiation and to apply the selected nominal friction pressure. In order to exceed DBTT and provide a sufficient level of ductility, additional actions (e.g. pre-heating) are required.

4.2.2 Extensive Plasticization Behavior Friction Phase

To reduce the initial introduced loading, the friction phase was split into two different applied pressure levels (15/60 MPa) and were linked by a soft transition gradient (22.5 MPa/s) (fig. 48). The preceding intial "rubbing" at a low pressure level for 2.0 s increased the weld interface temperature without any macroscopic plastic deformation and heated the weld specimens. The subsequent gradual increase to an elevated pressure level minimized the experienced loading rate and initiated the original friction phase. The selected input parameters for the following second friction and forging phase were similar to the previously presented process.

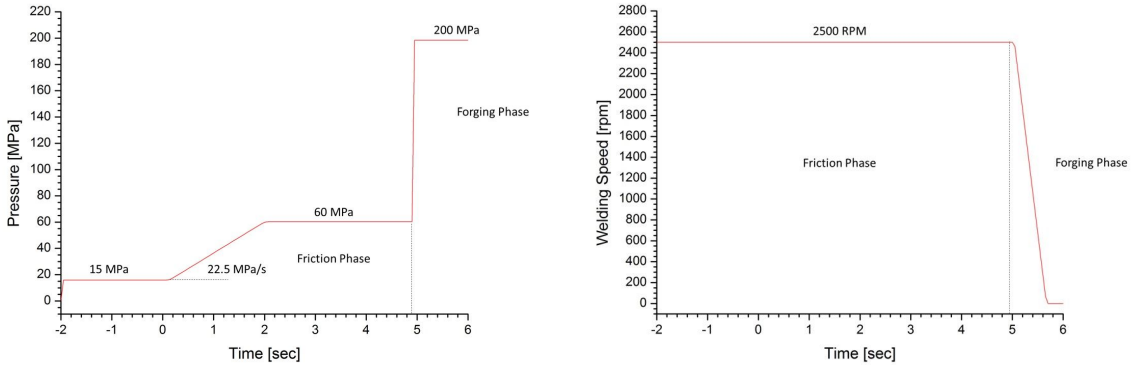

(a) (b)

Figure 48: Nominal input parameters: (a) Pressure and (b) welding speed pilot study RFW molybdenum – extensive plasticization behavior friction phase

The implementation of a preceding low pressure level and the subsequent soft transition to the actual applied friction pressure prevented the previously observed transgranular brittle fracture at the process initiation. However, the process needed to be aborted manually after 2.8 s, shortly after reaching the second friction pressure level (fig. 49). A sudden and steep increase of the upset nearly exceeded the machines capability of maximum displacement ($\approx$ 16 mm). The observed vigorous plasticization behavior of molybdenum within the friction phase is already reported in present literature [68].

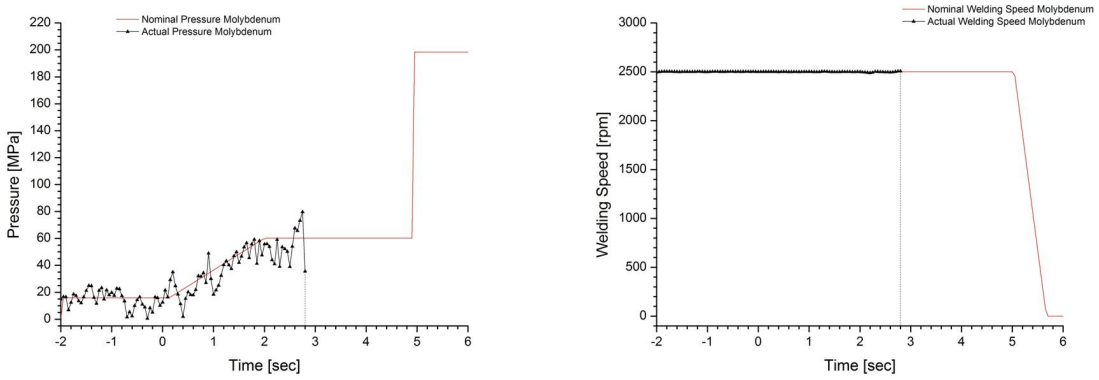

(a) (b)

Figure 49: Comparison of nominal and actual input parameters: (a) Pressure and (b) welding speed pilot study RFW molybdenum – extensive plasticization behavior friction phase

Fig. 50a and 50b show the courses of measured the upset and the ascertain derived upset-rate. Within the preceding low pressure friction stage (<0 s), the participating weld specimens came into initial contact and rub against each other without any significant plastic deformation (0.33 mm). The subsequent soft transition into the increased second friction stage (0–2 s) is reflected by a moderate increase of the experienced upset (2.47 mm) and accompanied upset-rate (3.23 mm/s). Though by passing the transition stage (>2 s), the recorded total upset shows a sharp and exponential increase of the material displacement just before the manual process termination. This is also reflected by a gradual increase of the derived upset-rate to its maximum value of 24.64 mm/s.

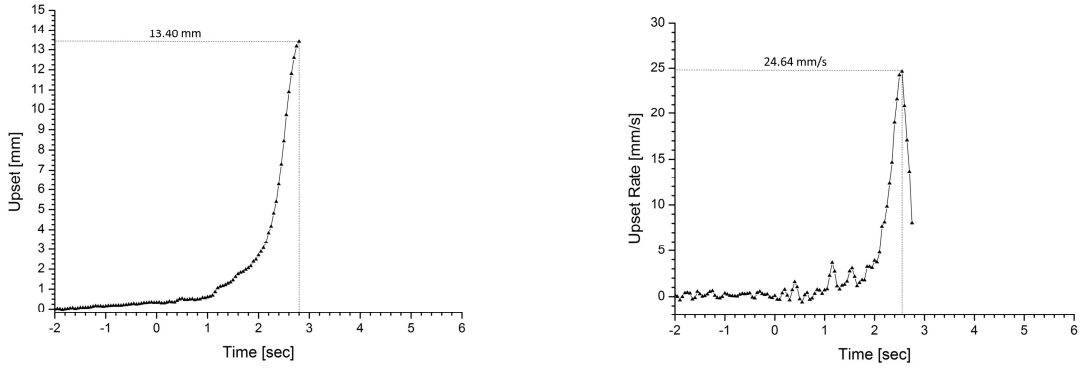

(a) (b)

Figure 50: Recorded (a) upset and acertained (b) upset rate pilot study RFW molybdenum – extensive plasticization behavior friction phase

The final drop of the material displacement-rate and "stabilization" of the plasticization behavior is less a sign of the intrinsic self-regulation of the process, rather than the influence of the distorted heat flow and increased cooling rate close to the clamping.

A first comparison of molybdenum to the reference low-carbon steel confirms molybdenum's vital plasticization behavior. Within the conducted experiments, molybdenum reveals a more than four times higher maximum upset-rate (26.64 mm/s) compared to the low-carbon steel (6.01 mm/s). The fundamental difference in upsetting is also reflected by the torque and power input as depicted in fig. 51. Within the preceeding low pressure friction stage (<0 s) and the transition stage (0–2 s), the nominal torque and therefore power input is directly related to the applied friction pressure (Coulomb's friction law). At the beginning of the second friction stage (>2 s) and after accomplishing the sticking condition ($\tau_{fric} = \tau_y$), the nominal torque and ascertained power input rapidly rise and result in a steady increase of the displacement-rate. Within the conducted experiments and the given machine capability, there is no stabilization (maximum peak) or quasi-steady-state (equilibrium level) of the nominal torque and therefore power input in the sticking condition within the friction phase observed.

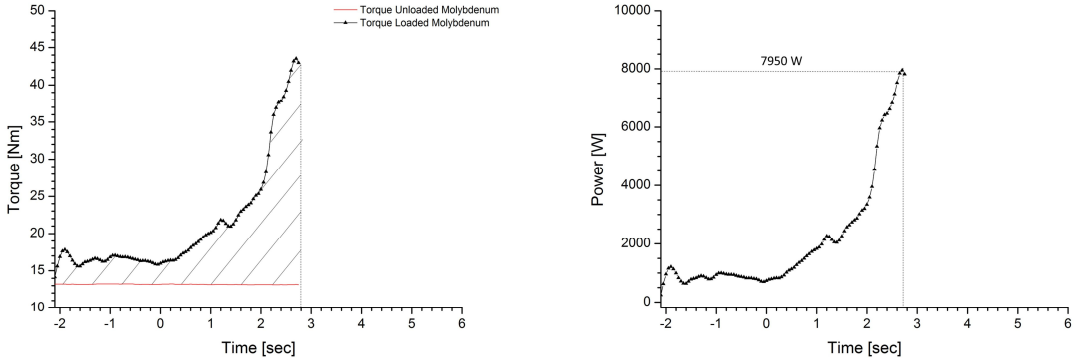

(a) (b)

Figure 51: Recorded (a) loaded/unloaded torque and acertained (b) power input pilot study RFW molybdenum – extensive plasticization behavior friction phase

As shown in fig. 52, the extensive plasticization behavior during processing is reflected by a massive "material bulk" instead of the typically formed flash. The manually operated process termination initiated a subsequent upward movement of the FSW weld head, and provoked a delamination of the weldment from the stationary pin. Molybdenum's thermophysical properties, thermal conductivity λ and specific heat capacity c, resulted in a quick heat distribution within the weld specimens. An indicator for a high temperature over a large distance are the observed annealing colors. The annealing colors are restricted by the beginning of the clamping and strengthens previous mentioned assumption of a distorted heat flow and an increased cooling rate next to the clamping system.

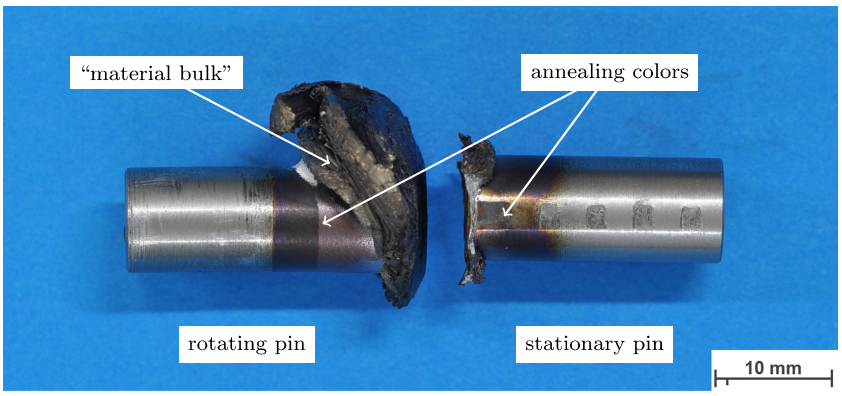

Figure 52: Extensive plasticized molybdenum specimen pilot study RFW molybdenum – extensive plasticization behavior friction phase

Molybdenum's vital plasticization behavior and vigorous displacement-rate within the friction phase complicate the direct drive friction welding process. A controlled transition from a stabilized friction stage to a subsequent forging phase is not feasible. Further, molybdenum's thermophysical properties and the selected weld cycle determine the transient temperature field within the weld specimens and govern the heat dissipation (Fourier's law). A more rapid energy input and thus shorter process time is required in order to generate a high spatial temperature gradient within the weld pins.

4.2.3 Stabilization and Controlling Problems Forging Phase

To prevent brittle fracture at room temperature and to increase the initial operating temperature, a preceding low pressure (<10 MPa) pre-heating stage was implemented. In order to reduce the actual friction time and to obtain a more rapid energy input, the previously implemented soft transition stage was renounced and replaced by a shorter friction time (0.8 s) accompanied by a high rotational speed (3000 rpm) (fig. 53). To reduce the previously in low-carbon steel observed effect of the “power burst” in the transition stage from the friction to the forging phase, the time between the selected spindle deceleration start and the initiation of the nominal forge pressure was delayed by 0.15 s (fig. 53b).

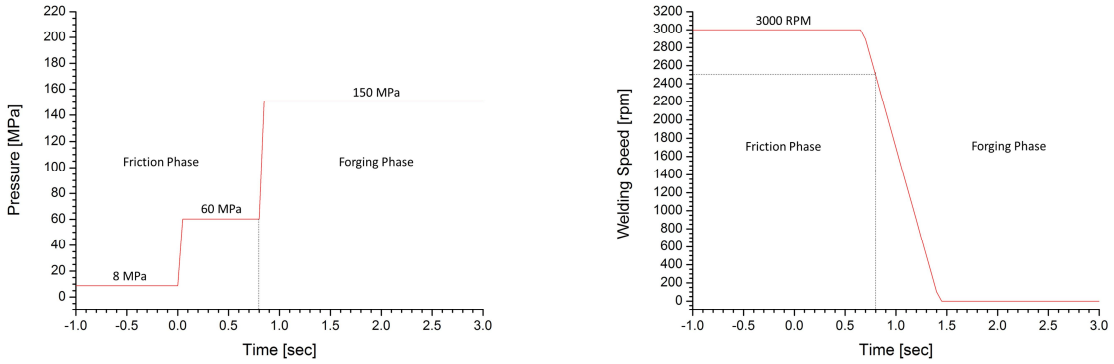

(a) (b)

Figure 53: Nominal Input parameters: (a) Pressure and (b) welding speed pilot study RFW molybdenum – stabilization and controlling problems forging phase

Similar to the reference low-carbon steel, the logged actual pressure reveals a maximum deviation from the nominal value at the initial forging phase (max. $\delta_{p,forge} = 29.5\%$). Additionally, the ongoing process inaccuracy after initiating the forging phase (>0.8 s) is reflected by a continuous series of deviated actual logged pressure values (fig. 54a). Finally, the process accuracy is only recovered after the spindle stop and the derived overall mean relative error for the related time period is $\overline{\delta}_{\mathrm{p,forge}} = 15.23\% \mid t_{forge} = t_{n\to 0}$. Further, the actual spindle deceleration starts 50 µm later than the nominal value and therefore the current spindle speed (2860 rpm) at forge pressure initiation is nearly the operating rotation speed (3000 rpm) (fig. 54b).

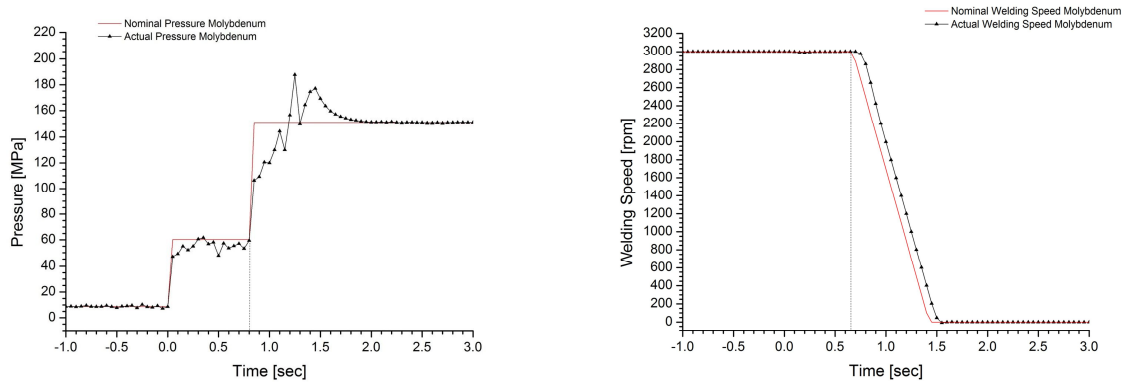

(a) (b)

Figure 54: Comparison of nominal and actual input parameters: (a) Pressure and (b) welding speed pilot study RFW molybdenum – stabilization and controlling problems forging phase

As depicted in fig. 55, within the friction phase (0–0.8 s), only a slight increase of the upset (0.99 mm) and a moderate maximum displacement-rate (2.66 mm/s) are observed. The time delayed subsequent forging phase initiated the actual material plasticization and mainly determines the total upset of 10.48 mm.

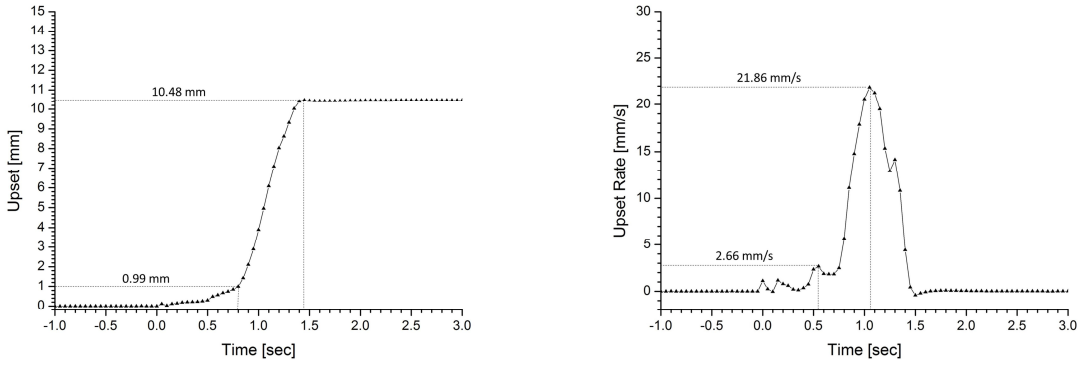

(a) (b)

Figure 55: Recorded (a) upset and acertained (b) upset rate pilot study RFW molybdenum – stabilization and controlling problems forging phase

The combination of an insufficient process accuracy in the initial and ongoing forging phase of the process design and the evolved temperature field within the weld specimens resulted in a wide ranged thermo-mechanically deformed conically formed zone (fig. 56). Further, the exposure to an increased loading condition is also reflected by the observed clamping marks on the previous rotating and stationary weld pins. Nevertheless, the first molybdenum welds were successfully DDFW on the FSW device, though further improvements were needed.

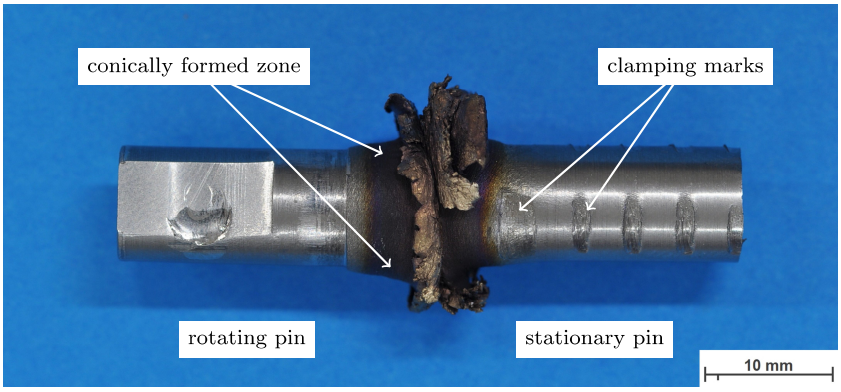

Figure 56: Destabilized and deformed molybdenum specimen pilot study RFW molybdenum – stabilization and controlling problems forging phase

4.2.4 Establishing a General DDFW Design for Molybdenum

Based on the recorded and analyzed data of the conducted pilot study for RFW of molybdenum, it was observed that molybdenum's intrinsic properties complicate a successful joining by applying the so far established two level design. The material's brittleness at room temperature prevented an initial transition to the friction stage and the general desired short welding cycles. Further, the in literature observed vigorous plasticization behavior within the friction phase was confirmed and the presence of an equilibrium stage within the given machine capability was not observed. In order to avoid extensive material plasticization and to keep the power input manageable, the actual axial shortening needed to be shifted into the forging phase. Although an initial transition from the friction to the forging phase resulted in an ongoing process inaccuracy of the applied forge pressure and led to an instable forging condition and an impermissible thermo-mechanical deformation. Summarized, a general re-design of the so far established two level process was required.

First, in order to countervail the material's brittleness at room temperature and to increase the initial operating temperatures, it was concluded that a proper in-situ pre-heating stage should solve this problem. Compared to common pre-heating techniques (e.g. in a furnace), the implementation of an in-situ pre-heating stage enables a continuous welding process. To monitor the obtained pre-heating temperature, the stationary weld pins were equipped with thermocouples along the outer circumference at 2 mm and 10 mm away from the weld interface. The first conduced experiments proved a general feasibility to increase and stabilize the initial operating temperature by the means of the "rubbing" at a minimum axial applied pressure level (fig. 59).

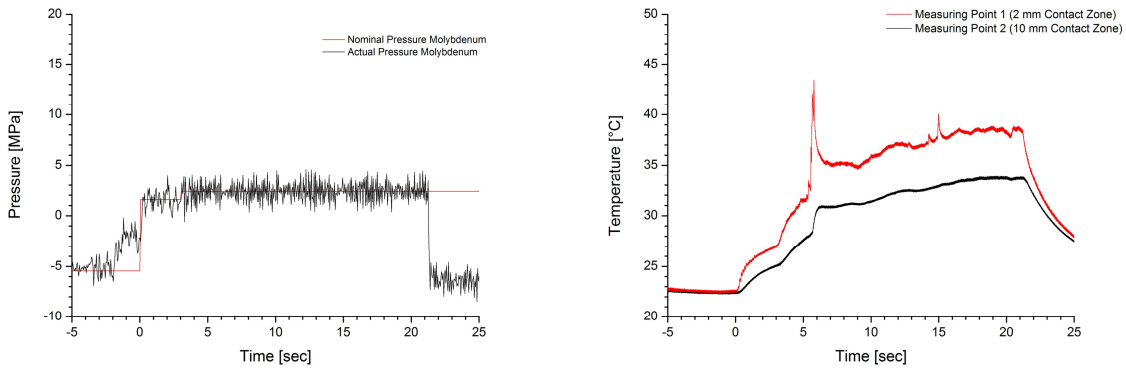

(a) (b)

Figure 57: (a) Comparison of nominal and actual pressure and (b) recorded temperature evolution single stepped pre-heating stage pilot study RFW molybdenum – establishing general DDFW design for molybdenum

The required initial operating temperatures need to be higher than 300 °C to provide a sufficient level of ductility and to exceed DBTT. Therefore, the initial process design was upscaled by the implementation of further low pressure friction levels (fig. 58a) and applied for several rotational speeds (tab. 8). With the read-out of the thermocouples, a stabilization and scalability of the quasi-steady-state temperature evolution (fig. 58b) within the weld specimens was proven. This means that the heat dissipation from the weld interface reached an equilibrium between the by Coulomb's friction inserted power input and the heat dissipation.

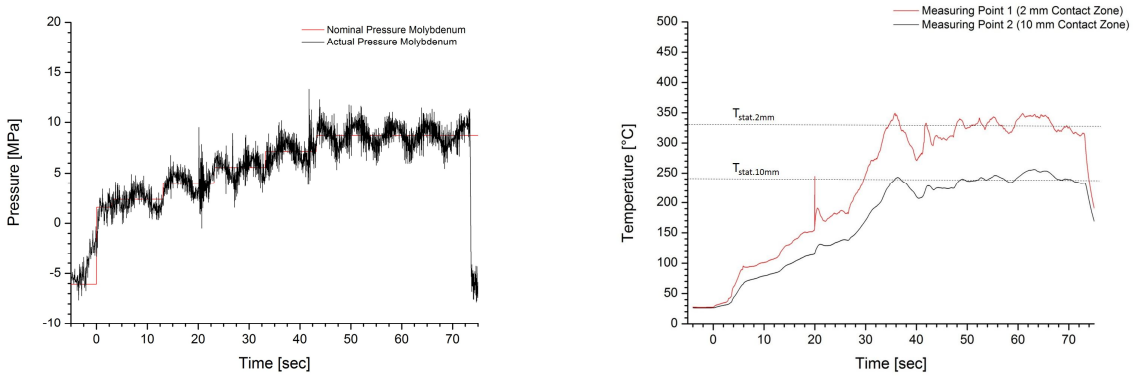

(a) (b)

Figure 58: (a) Comparison of nominal and actual pressure and (b) recorded temperature evolution multi stepped pre-heating stage pilot study RFW molybdenum – establishing general DDFW design for molybdenum

Within the conducted experiments and depending on the selected rotational speed, the logged maximum stationary temperatures (2 mm away from the interface) were in the range between 160 °C ($T/T_m = 0.15$) and 490 °C ($T/T_m = 0.26$) (tab. 8).

Table 8: Recorded temperature evolution for several rotational speeds of a multi stepped pre-heating stage stage pilot study RFW molybdenum – establishing general DDFW

Rotational Speed [rpm]	Maximum Pressure [MPa]	$T_{Stat.2mm}$ [°C]	$T_{Max.2mm}$ [°C]	$T_{Stat.10mm}$ [°C]	$T_{Max.10mm}$ [°C]
2500	8.65	160	170	125	135
2750	8.65	210	230	170	230
3000	8.65	320	350	240	260
3200	8.65	490	530	340	370

Further, the previously conducted experiments revealed that the majority of molybdenum's plasticization was contributed by the transition from the friction to the forging phase. However, the so far established process design in the transition stage revealed a poor process accuracy and a limited controllability of the applied pressure level. In order to enable a fully defined and controlled transition from friction into forging phase, additional input parameters: 1) Pressure acceleration $\ddot{p}$ to facilitate a 2) pressure gradient $\dot{p}$ in the transition zone and 3) spindle deceleration $\dot{n}$ were implemented.

To determine the process accuracy of the adapted transition stage, the actual and nominal pressure courses of the established (fig. 59a) and the adjusted (fig. 59b) process design are opposed. Towards the forging phase of the established process design, the logged actual pressure of the adjusted process design reveals a minimum deviation from the nominal value at the initial and ongoing forging phase.

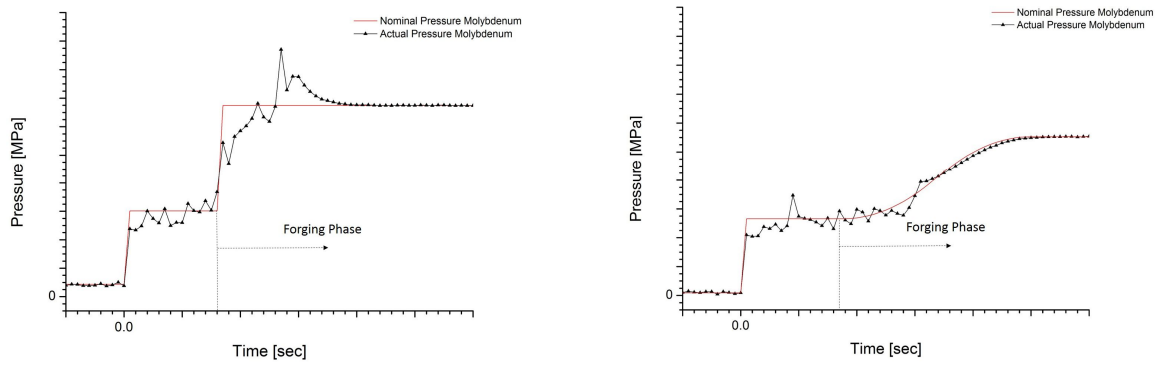

(a) (b)

Figure 59: Comparison of pressures for (a) established process design and (b) adjusted process design for pilot study RFW molybdenum – establishing general DDFW design for molybdenum

The more precise process accuracy and improved controllability of the forging phase is also reflected by a comparison of the relative errors (fig. 60) derived from the nominal and actual recorded pressure courses. By considering the time period from the initiation of the forging phase to the final spindle stop, the overall mean relative error of the adjusted process design ($\overline{\delta}_{\mathrm{p,forge}} = 6.82\% \mid t_{forge} = t_{n\to 0}$) is significantly reduced compared to the overall mean relative error of the so far established process design ($\overline{\delta}_{\mathrm{p,forge}} = 15.23\% \mid t_{forge} = t_{n\to 0}$).

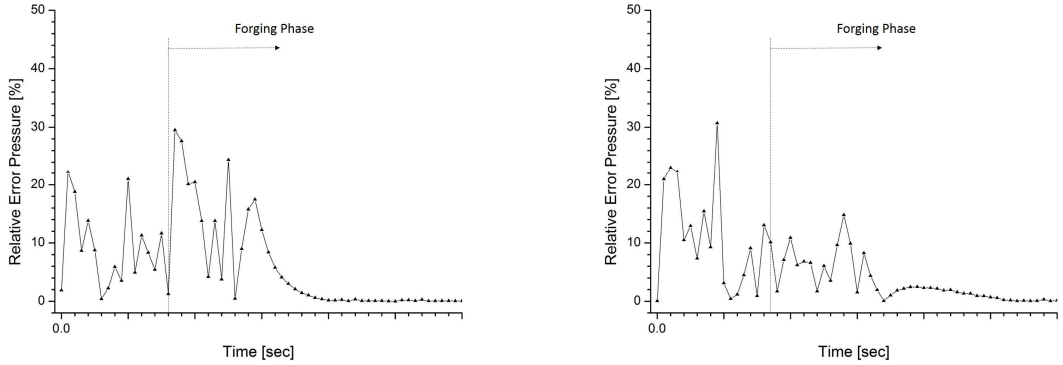

(a) (b)

Figure 60: Comparison of relative errors of pressure for (a) established process design and (b) adjusted process design for pilot study RFW molybdenum – establishing general DDFW design for molybdenum

4.3 Case Study RFW Molybdenum

This subchapter provides selected results of the case study of rotary friction welding of molybdenum. The previously revised process design was applied for Ø12 mm molybdenum weld specimens to obtain a variety in plasticization at variable rotational speeds (2500 rpm, 2600 rpm, and 2750 rpm). Feasible welding parameters and derived technical information were identified to generate sound and proper joints. Further, the evolved microstructure was characterized by the means of microscopy and related mechanical properties were discussed.

4.3.1 Recorded and Derived Output Parameters

The conducted case study of molybdenum experiments reveals nearly completely congruent actual pressure curves and confirm the precise process accuracy of the revised process design (fig. 61a). The overall mean relative errors of the predominantly forging phase are $\overline{\delta}_{\mathrm{p,forge}} = 3.77\%$ at 2500 rpm rotational speed, $\overline{\delta}_{\mathrm{p,forge}} = 6.82\%$ at 2600 rpm rotational speed, and $\overline{\delta}_{\mathrm{p,forge}} = 6.35\%$ at 2750 rpm rotational speed for $t_{forge} = t_{n\to 0}$.

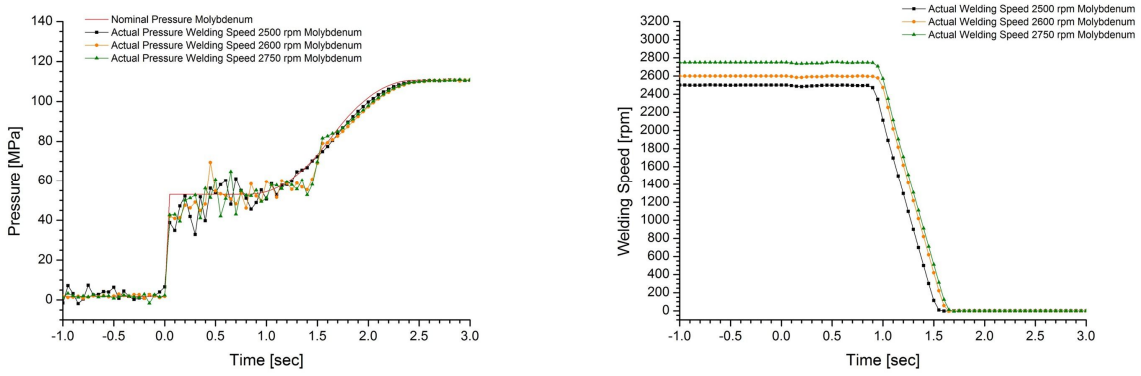

(a) (b)

Figure 61: Comparison of nominal and actual input parameters: (a) Pressure and (b) welding speed case study RFW molybdenum

Further, the spindle deceleration was set to a constant value of 4000 rpm/s and resulted in slightly different spindle deceleration times of the varying rotational speeds (fig. 61b). Therefore, an increased rotational speed directly increases the introduced power input level, and also extends the spindle deceleration time and weld cycle. As a result, the upset increases (fig. 62a) from 2.78 mm to 3.96 mm to 5.28 mm, at 2500 rpm, 2600 rpm, and 2750 rpm, respectively. The actual difference in the plasticization behavior of the weld specimens is reflected by their derived displacement-rates (fig. 62b). While the upset-rate of the weld specimen with the lowest power input and the shortest deceleration time is constantly reduced at the end of the weld cycle, the upset-rates of the

weld specimens with the increased power input and the extended deceleration times are rapidly increased. The derived maximum upset-rates within the forging phase are 3.82 mm/s at 2500 rpm, 9.46 mm/s at 2600 rpm, and 13.69 mm/s at 2750 rpm.

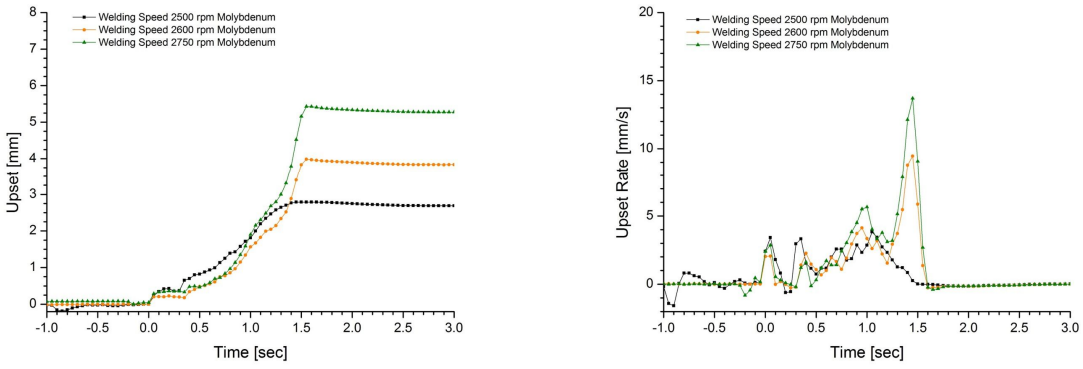

(a) (b)

Figure 62: Recorded (a) upset and acertained (b) upset rate case study RFW molybdenum

As shown in fig. 63b, the two separated power input peaks are determined by the area between the logged torque in loaded and unloaded condition (fig. 63a). The first power peak is attributed to the transition from the sliding ($\tau_{fric} < \tau_y$) to the sticking condition ($\tau_{fric} = \tau_y$) and the beginning of a significant axial shortening within the friction phase.

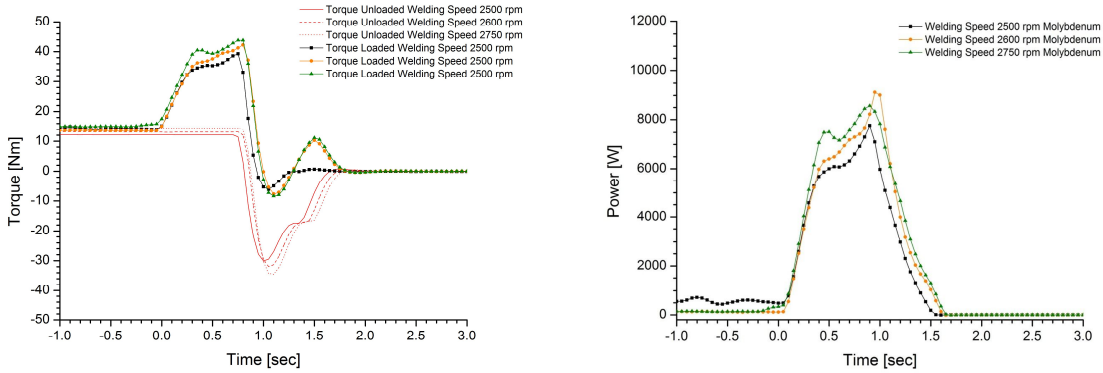

(a) (b)

Figure 63: Recorded (a) loaded/unloaded torque and acertained (b) power input case study RFW molybdenum

The second peak is the result of the ongoing forging phase and the increased applied forging pressure. Finally, the decreasing rotational speed results in a sharp drop off the derived power input to zero. Considering the vigorous plasticization and the related displacement-rates close to the end (>1.3 s) of the weld cycle at a minimum amount of provided power input (fig. 63b), it is assumed that there is only a small process window within the given machine capability to produce sound welds.

Based on the previously derived power input and the logged material plasticization, the total energy input over time and the upset over total energy input are plotted in fig. 64. For the determination of the particular total energy input, only the actual weld cycle without the preceding in-situ pre-heating stage ($\approx$ 350 °C) is considered. The total energy input of the weld cycles within process times of approximately 1.6 s are 6296 J ($\rightarrow$ 56 J/mm^2) at 2500 rpm, 7397 J ($\rightarrow$ 65 J/mm^2) at 2600 rpm and 8022 J ($\rightarrow$ 71 J/mm^2) at 2750 rpm. The actual impact of the varying total energy input is visualized in fig. 64b. While the nearly similar ratios of upset to energy (gradient) reveal a moderate level in the range of <7000 J, the gradients rapidly increase in the range of >7000 J. It is assumed that at least a minimum amount ($\approx$7000 J $\rightarrow$ 62 J/mm^2) of (specific) total energy input (activation energy) within a certain short time period is needed in order to initiate the previous and also in literature reported sudden and steep plasticization behavior.

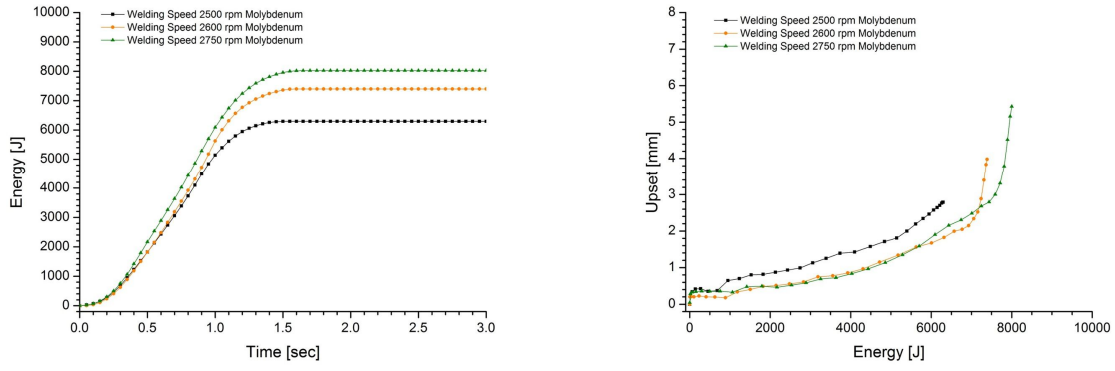

(a) (b)

Figure 64: Acertained (a) energy input and (b) upset behavior case study RFW molybdenum

4.3.2 Assessment of the Weld Specimens

Visual Inspection Visual inspection of the welded specimens reveals a difference in the visual appearance of the rotational symmetrically formed flashes (fig. 65). With increasing total energy input, more material is plasticized and extruded from the weld interface into the flash. As a result, an even more massive flash is formed. Further, as a result

of the material's thermophysical properties and even though the short weld cycles, the observed annealing colors are expanded over a wide area and indicate an extended HAZ compared to the reference low-carbon steel. In addition, the high nominal torques during processing result in clamping marks on the stationary weld pins.

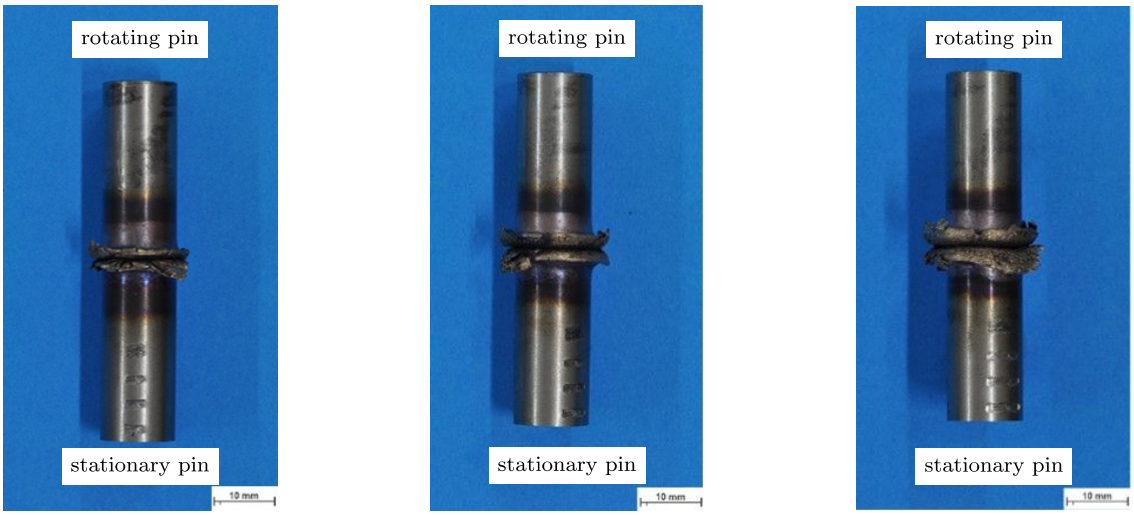

(a) (b) (c)

Figure 65: As-welded RFW molybdenum specimens (a) 2500 rpm (b) 2600 rpm (c) 2750 rpm

The integrity and further the microstructure is evaluated by the means of the polished and etched longitudinal cross-sections of the generated joints (fig. 66). The embedded and polished regions of interest indicate that at least a minimum amount of total energy input and as a result upset is needed to facilitate a proper bonding. While the weld specimen with the highest maintained energy input (8022 J) reveals a sound and defect free bond over the entire weld interface, the two weld specimens with the lower maintained energy input (7397 J and 6296 J) show the presence of welding defects (lack of fusion). The etched cross-sections of the generated joints confirm the previously mentioned assumption of an extended HAZ compared to the reference low-carbon steel. The maintained weld energy input within the molybdenum experiments also affects the width of the formed HAZ. The parameter configuration (2750 rpm) which provides the highest energy input shows the most pronounced HAZ. Further, the etched cross-sections show the for friction welding typically formed weld sections. Similar to the reference low-carbon steel, the weldments reveal a radial influence of the evolved microstructures, with a maximum HAZ width at the outer circumference and a minimum HAZ width at the weld interface center.

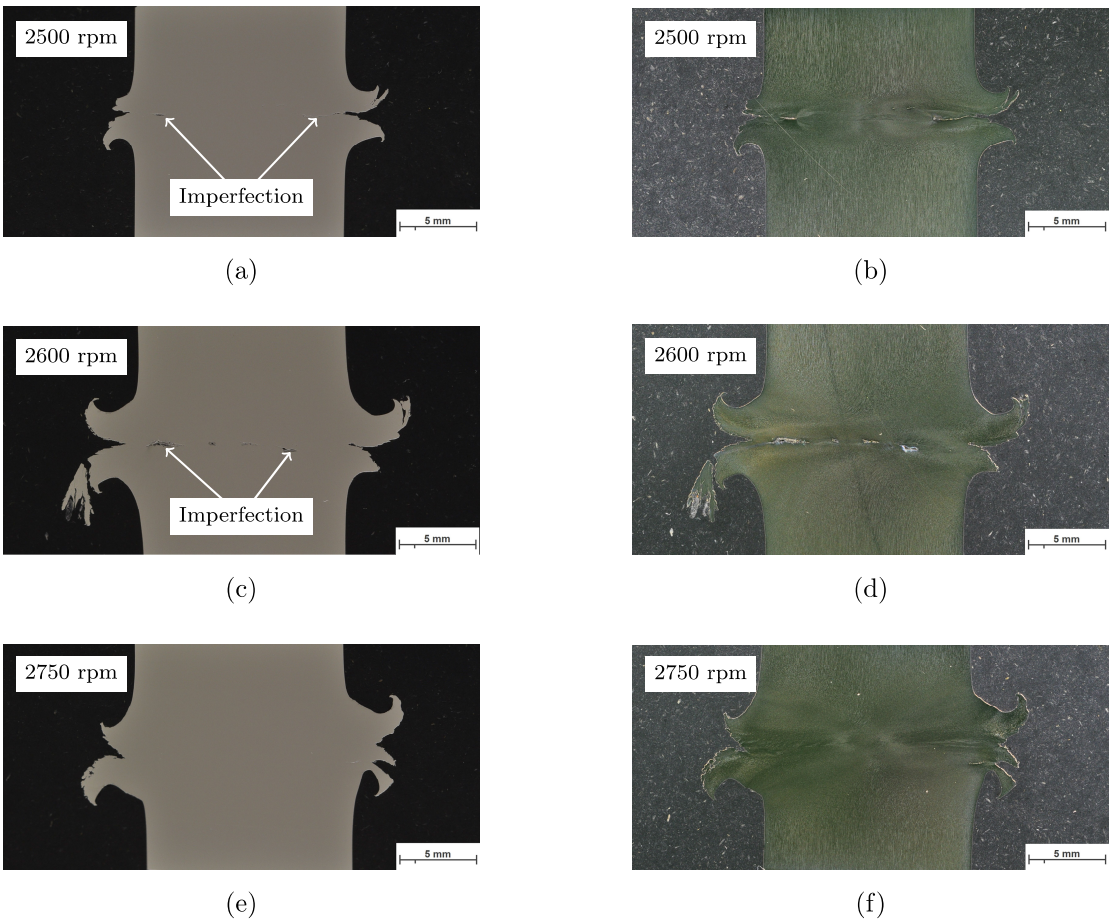

Figure 66: (a) Polished unetched and (b) etched [Cr m2] 2500 rpm, (c) polished unetched and (d) etched [Cr m2] 2600 rpm, (e) polished unetched and (f) etched [Cr m2] 2750 rpm cross-section of RFW molybdenum

Microstructure Characterisation In order to describe the evolved microstructure in a more detailed way, a subsequent microscope study of the weld specimen with the highest energy input (2750 rpm) was conducted. As depicted in fig. 67, light optical microscopy was examined in the region next to weld interface center, the distinct hot-worked elongated grains of the undeformed base material (fig. 68d) are continuously re-aligned outwards in direction of the plastic flow in the partially deformed zone (III) (fig. 68c). With decreasing distance to the weld interface, the microstructure is exposed to a higher amount of temperature, strain rate, and plastic deformation. As a result, the former distinct hot-worked microstructure is completely annihilated within the fully plasticized zone (II) (fig. 68a).

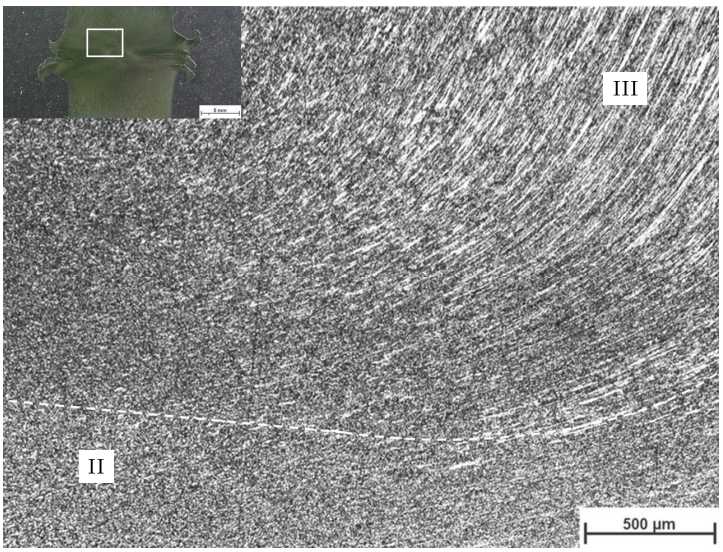

Figure 67: Weld cross-sections of an etched [murakami, 50x magnification] RFW molybdenum specimen (2750rpm)

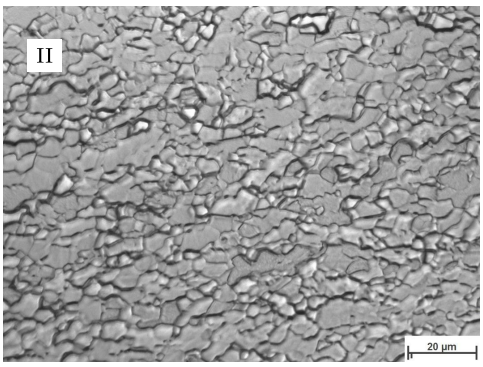

(a)

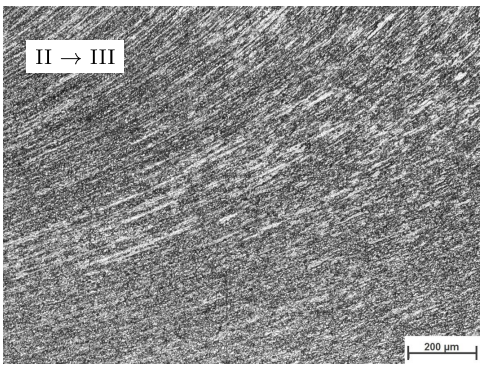

(b)

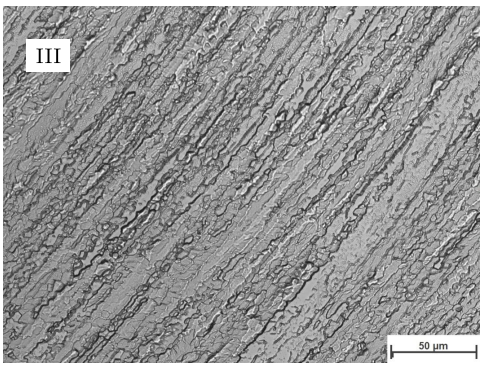

(c)

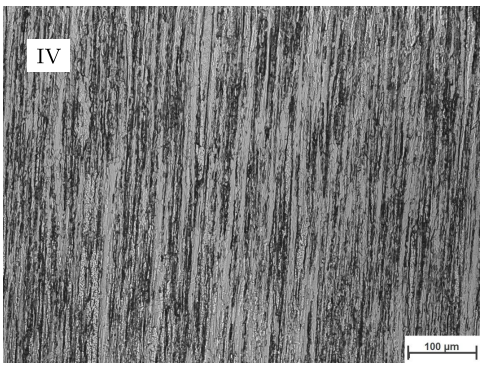

(d)

Figure 68: Etched (a) fully plasticized zone [murakami, 1000x magnification], (b) transitions weld sections [murakami, 100x magnification], (c) partially deformed zone [murakami, 500x magnification] and (d) undeformed zone [murakami, 200x magnification] of RFW molybdenum (2750 rpm)

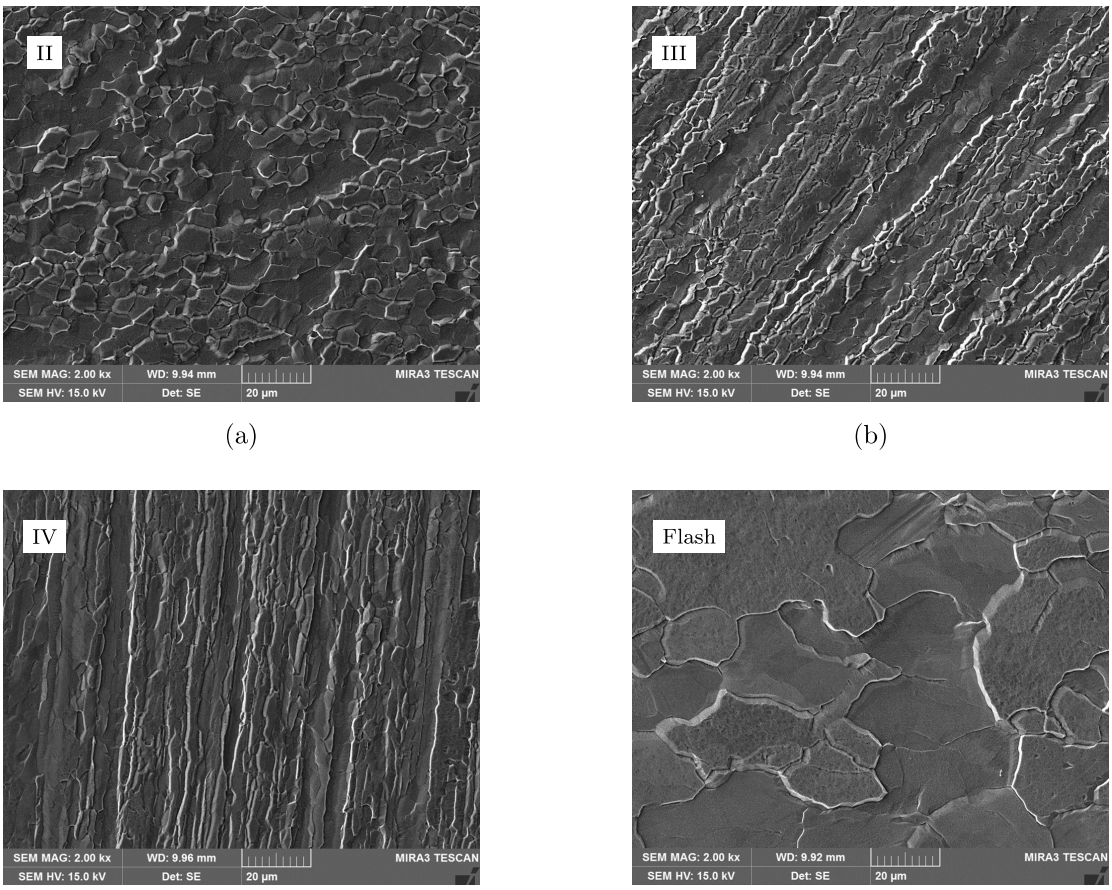

Figure 69: Scanning electron microscopy of etched (a) fully plasticized zone [murakami, 2000x magnification], (b) partially deformed zone [murakami, 2000x magnification], (c) base material [murakami, 2000x magnification] and (d) flash [murakami, 2000x magnification] of RFW molybdenum (2750 rpm)

In addition to light optical microscopy, scanning electron microscopy was conducted (fig. 69). The provided higher magnification and depth of sharpness enable a more detailed exmination of the weld sections. In the fully plasticized zone (II), the occurring dynamic recovery/recrystallization results in an equiaxed, very fine grained microstructure (fig. 69a). The grain size was determined by the means of EBSD and returned an average grain size value of 4.39 µm. The partly deformed zone (fig. 69b) and re-oriented microstructure is characterized by a partly recovery/recrystallization of the prior elongated grains of the undeformed base material (fig. 69c). Further, by the comparison of the evolved microstructure in the fully plasticized zone (fig. 69a) to the formed flash (fig. 69d), it is assumed that the missing high degrees of deformation result in a grain growth and the grain coarsened microstructure of the flash.

Determination Chemical Composition In order to evaluate the influences of impurities, contaminations, residual oxygen, and the weld atmosphere on the weldment, the chemical composition in the fully plasticized zone (fig. 70a) was determined by the means of energy dispersive X-ray spectroscopy (EDX) point scan (fig. 70b). The recorded spectrum indicates that the chemical composition (tab. 9) of the fully plasticized zone consists out of the predominant molybdenum base material (92.86 wt%), but also out of a considerable amount of oxygen (7.14 wt%), though the listed high oxygen error and the chemical affinity of molybdenum to oxygen need to be taken into account. It is likely that the measured oxygen value is mainly influenced by the formed oxide layer during the time period from sample preparation to EDX measurement. Therefore, the obtained value for oxygen in the fully plasticized zone has to be considered with care. However, the absence of further elements in the spectrum indicates that the presence of impurities and contaminations can be excluded.

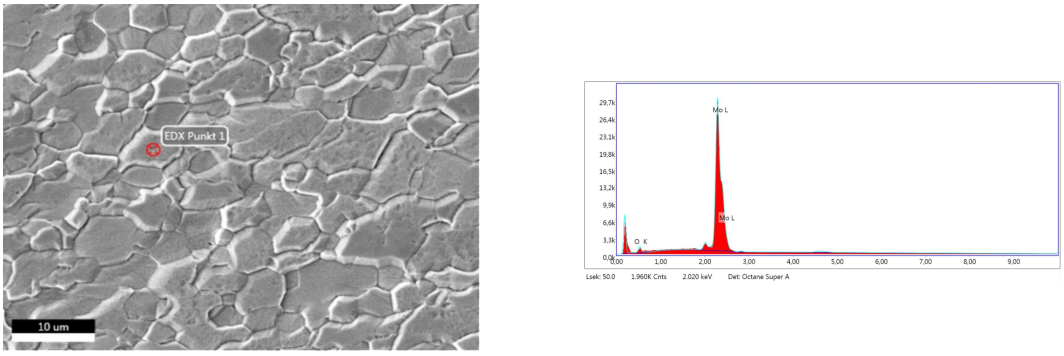

(a) (b)

Figure 70: Scanning electron microscopy (a) fully plasticized zone and (b) energy dispersive X-ray spectroscopy 2700 rpm molybdenum RFW specimen

Table 9: Chemical composition EDX point scan RFW molybdenum

Element	Shell	wt%	Error %
Molybdenum	L	92.86	1.65
Oxygen	K	7.14	12.40

Mechanical Characterisation The evolution of molybdenum's microstructure is not reflected by the logged hardness values. The in transverse and longitudinal direction measured Vickers hardness HV1 reveals a similarly homogeneous hardness distribution of the entire weldment (fig. 71). This means that there is no significant deviation (tab. 10) of the single average hardness value of the fully plasticized zone (246 ± 7 HV1), partly deformed zone (245 ± 7 HV1), and undeformed zone/base material (245 ± 6

HV1). The phenomenon of the evolved homogeneous hardness distribution within the weld specimen correlates with the in literature [69] reported observations. Ambroziak only observed a slight increase of the hardness values in the contact zone (260 HV0.05). During processing, the material's distinct work-hardened microstructure is continuously annihilated and results in a new fine grained microstructure. Consindering the results of the hardness measurements, it is reasonable that the loss of work hardening is in an equilibrium to the increase of grain boundary strengthening.

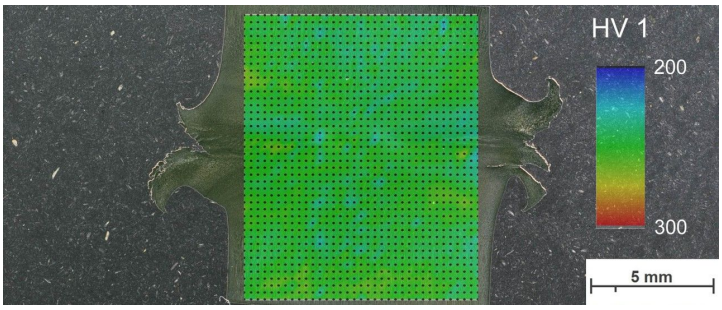

Figure 71: Hardness map and distribution RFW molybdenum

Table 10: Hardness values for representative weld sections RFW molybdenum

Weld Section	Average Hardness [HV1]	Standard Deviation Hardness [HV1]
Fully plasticized zone	246	± 7
Partially deformed zone	245	± 7
Undeformed zone and Base material	245	± 6

4.4 Case Study RFW TZM

This subchapter provides selected results of the case study of rotary friction welding of TZM. An analogous approach to that of the case study molybdenum was chosen. The previously revised process design was applied for Ø9 mm TZM weld pins and to achieve a variation in material displacement a variable rotational speed (2500 rpm, 2600 rpm, and 2750 rpm) was selected. Feasible welding parameters and derived technical information were identified to generate welds. Further, the evolved microstructure was characterized by the means of microscopy and related mechanical properties were discussed.

4.4.1 Recorded and Derived Output Parameters

Similar to the previously presented case study and despite the increased applied pressure, the recorded actual pressure curves are nearly congruent (fig. 72a). The overall mean relative errors of the predominantly forging phase are $\overline{\delta}_{\mathrm{p,forge}} = 4.17\%$ at 2500 rpm rotational speed, $\overline{\delta}_{\mathrm{p,forge}} = 5.12\%$ at 2600 rpm rotational speed, and $\overline{\delta}_{\mathrm{p,forge}} = 7.07\%$ at 2750 rpm rotational speed for $t_{forge} = t_{n\to 0}$.

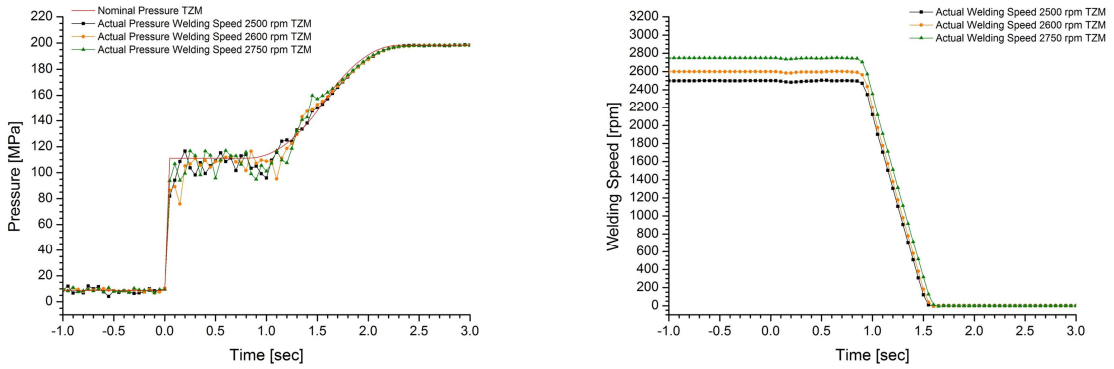

(a) (b)

Figure 72: Comparison of nominal and actual input parameters: (a) Pressure and (b) welding speed case study RFW TZM

In order to illustrate a nearly similar material plasticization compared to the commercially pure molybdenum, the carbide stabilized TZM requires nearly two times higher friction and forge pressure levels. The logged upsets increase (fig. 73a) from 3.95 mm to 5.43 mm to 7.09 mm, at 2500 rpm, 2600 rpm, and 2750 rpm, respectively. The derived and related maximum material displacement-rates (fig. 73b) are 7.73 mm/s at 2500 rpm, 9.98 mm/s at 2600 rpm and 15.46 mm/s at 2750 rpm.

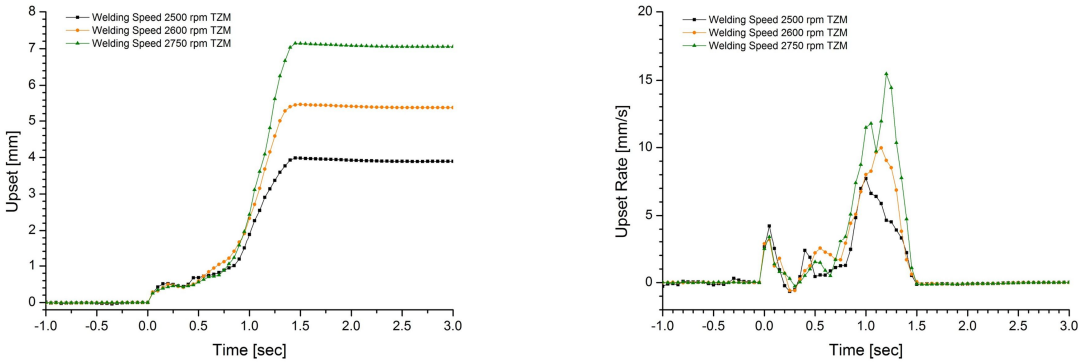

(a) (b)

Figure 73: Recorded (a) upset and acertained (b) upset rate case study RFW TZM

In comparison to commercially pure molybdenum, the actual difference in the plasticization behavior of TZM is reflected by the derived displacement-rates close to the end of the spindle deceleration. While the maximum upset-rate of molybdenum occur nearly the spindle stop (1.45 s) (fig. 62b), the maximum upset-rate of TZM is shifted to earlier stages (<1.20 s) (fig. 73b) despite the increased applied pressure (fig. 72a) and higher specific power input (fig. 74b). It is assumed that the high-temperature strength of TZM results in an earlier recovery of the material's strength upon cooling and the stabilization of the upset-rates within the ongoing forging phase at a continously decreasing power input.

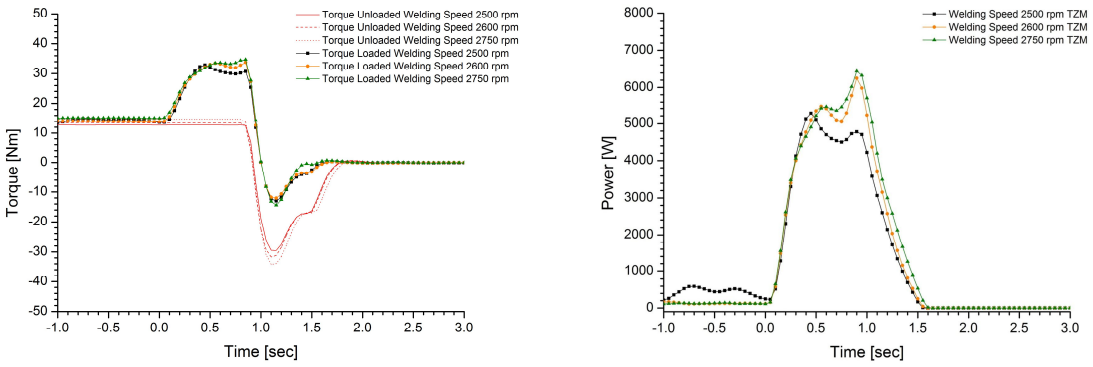

(a) (b)

Figure 74: Recorded (a) loaded/unloaded torque and acertained (b) power input case study RFW TZM

Based on the previously derived power input and the logged material plasticization, the total energy input over time and the upset over total energy input are plotted in fig. 75. For the determination of the particular total energy input, only the actual weld cycle without the preceding in-situ pre-heating stage ($\approx$ 350 °C) is considered. The total energy input of the weld cycles are 4745 J ($\rightarrow$ 75 J/mm^2) at 2500 rpm, 5335 J ($\rightarrow$ 85 J/mm^2) at 2600 rpm and 5694 J ($\rightarrow$ 90 J/mm^2) at 2750 rpm (fig. 75a). In relation to commercially pure molybdenum, the doubling of the applied pressure values resulted in a nearly 30% higher specific weld energy in order to achieve a similar upset response.

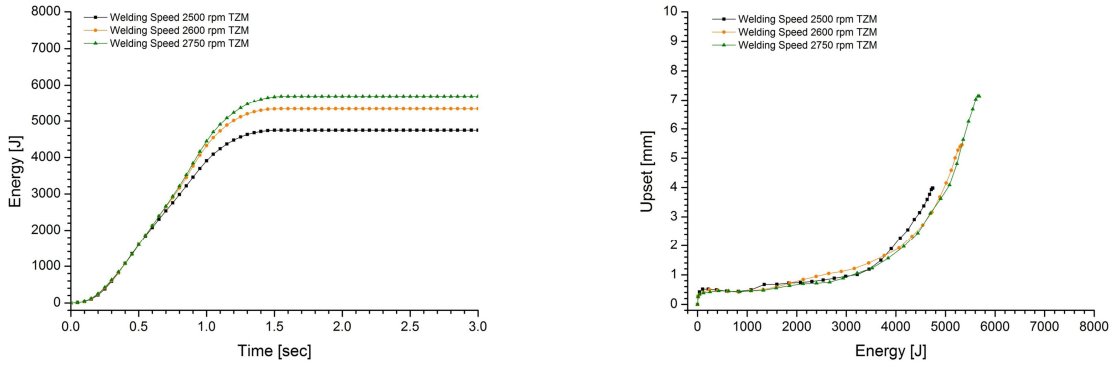

(a) (b)

Figure 75: Acertained (a) energy input and (b) upset behavior case study RFW TZM

4.4.2 Assessment Weld Specimens

Visual Inspection The as-welded specimens are depicted in fig. 76. The visual inspection of the TZM weld specimens reveals rotationally symmetrical, soundly formed flashes and a slightly different visual appearance in relation to the molybdenum flashes. For the weld specimens providing the higher energy input (2600 rpm and 2750 rpm), a slightly angular misalignment is notable. Further, the observed annealing colors are expanded in the same range like in the molybdenum case study and also indicate an extended HAZ compared to the reference low-carbon steel. In addition, the high nominal torques during processing result in clamping marks on the stationary weld pins.

(a) (b) (c)

Figure 76: As-welded RFW TZM specimens (a) 2500 rpm (b) 2600 rpm (c) 2750 rpm

The integrity and further the microstructure is evaluated by the means of the polished and etched longitudinal cross-sections of the generated joints (fig. 77). The embedded and polished regions of interest reveal the presence of welding defects (lack of fusion) in all of the TZM welding specimens. The present bonding defects are mainly situated on one side of the outer circumference of the weld interface. It is likely that the manually adjusted (for RFW tilt angle $\alpha = 0\ °$) and fixed pitch axis relaxed under the exposure to heavier loads, and slightly changed the tilt angle ($\alpha \neq 0\ °$) during processing. Considering the actual circumstances (forge pressure level, short welding cycle, the machine layout (stiffness)), it is reasonable that the angular misalignment caused the asymetric bonding defects.
Similar to the previous molybdenum experiments, the maintained weld energy input affects the width of the formed HAZ. The parameter configuration (2750 rpm) which provides the highest energy input shows the most pronounced HAZ. The etched cross-sections show the for friction welding representative formed weld sections, this means the transition from the undeformed base material (IV) to the severely deformed fully plasticized zone (II) and the contact zone (I). The etched cross-sections reveal a radial influence of the evolved microstructures, with a maximum HAZ width at the outer circumference and a minimum HAZ width at the weld interface center.

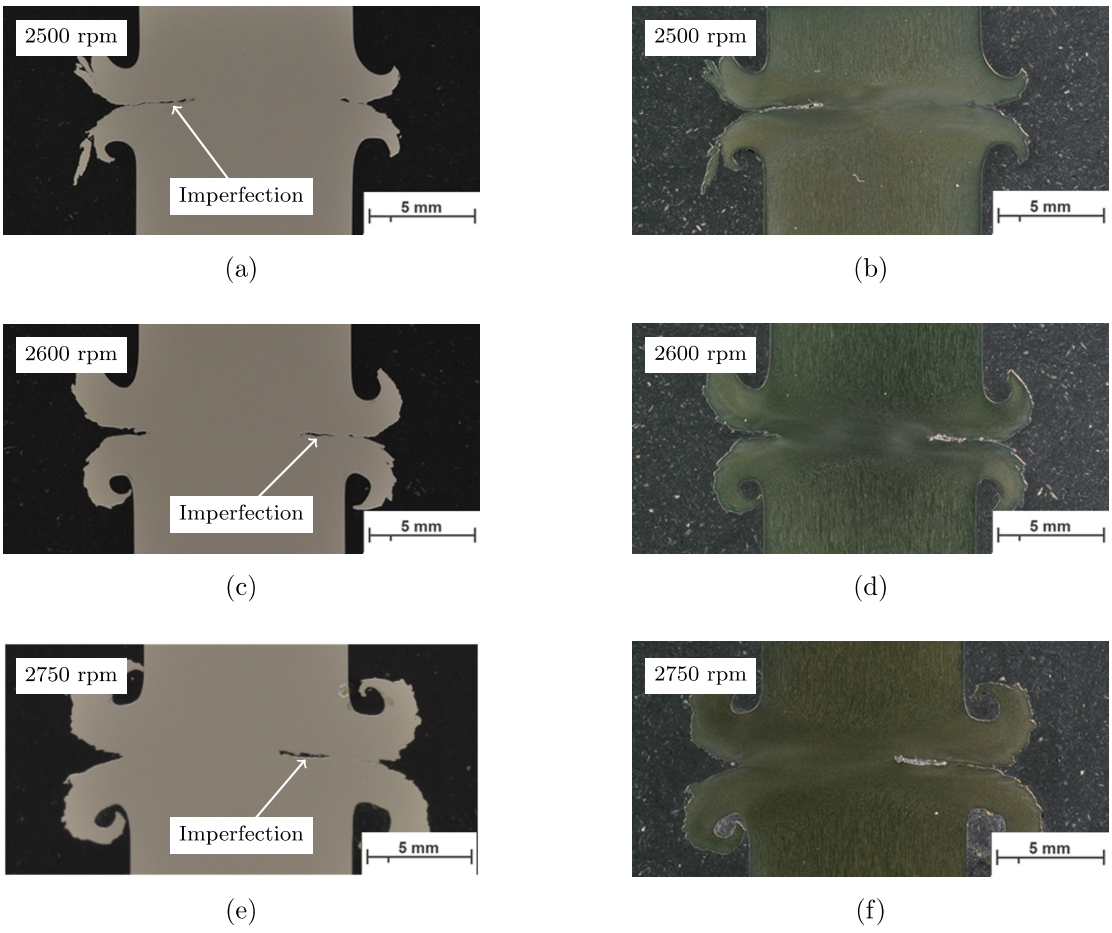

Figure 77: (a) Polished unetched and (b) etched [Cr m2] 2500 rpm, (c) polished unetched and (d) etched [Cr m2] 2600 rpm, (e) polished unetched and (f) etched [Cr m2] 2750 rpm cross-section of RFW TZM

Microstructure Characterisation In order to compare the evolved mircostructure in the similar region next to the weld interface center of TZM to molybdenum, a subsequent microscope study of the TZM weld specimen with the highest energy input (2750 rpm) was conducted. As depicted in fig. 78, analogous to the molybdenum weld specimen, the distinct hot-worked elongated grains of the undeformed base material (fig. 79d) are continuously re-oriented outwards in the partially deformed zone (III) (fig. 79c), and finally annihilated in the fully plasticized zone (II) (fig. 79a). In the fully plasticized zone (II), the occurring dynamic recovery/recrystallization results in a finer grained microstructure (fig. 80a) with an average grain size value of 1.43 µm. It might be assumed that the reduction in grain size is a result of the material's higher recrystallization temperature and the in the process occurring degrees of deformation. Further, the visual appearance of the grain coarsened microstructure of the formed TZM flash (fig. 80d) differs to molybdenum. The decorated grain boundaries might indicate the presence of precipitations and oxides in the flash.

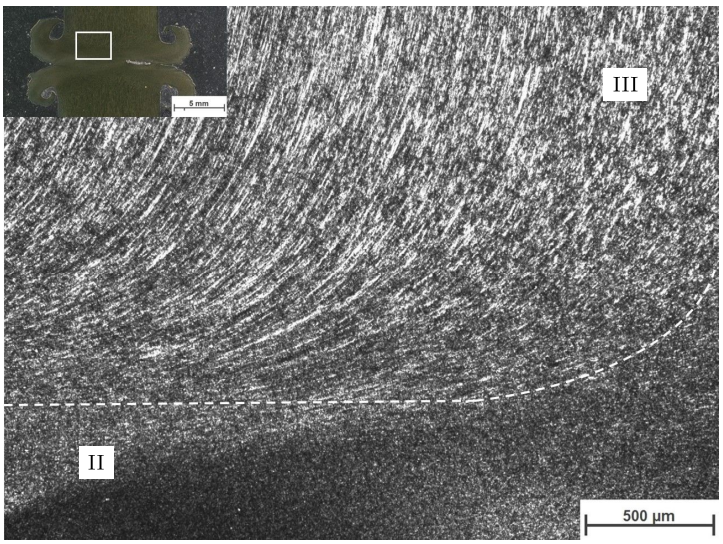

Figure 78: Weld cross-sections of an etched [murakami, 50x magnification] RFW TZM specimen (2750rpm)

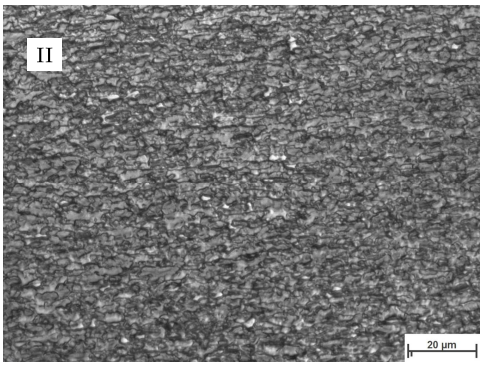

(a)

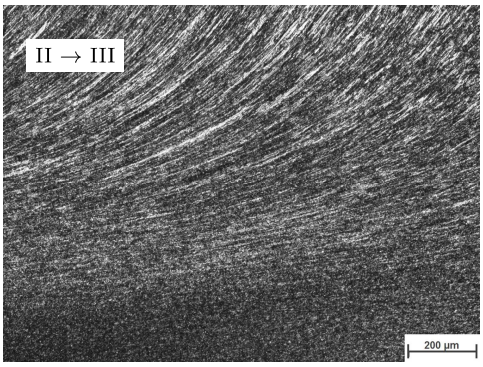

(b)

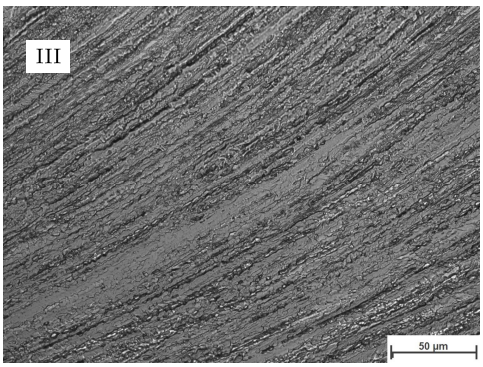

(c)

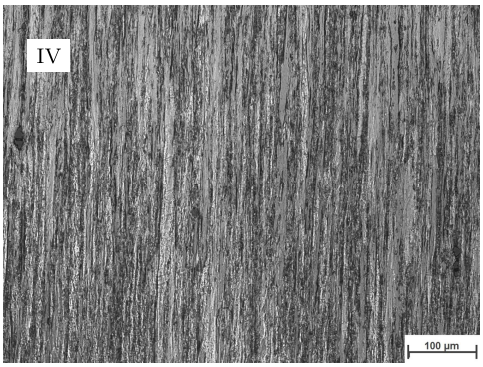

(d)

Figure 79: Etched (a) fully plasticized zone [murakami, 1000x magnification], (b) transitions weld sections [murakami, 100x magnification], (c) partially deformed zone [murakami, 500x magnification] and (d) undeformed zone [murakami, 200x magnification] of RFW TZM (2750 rpm)

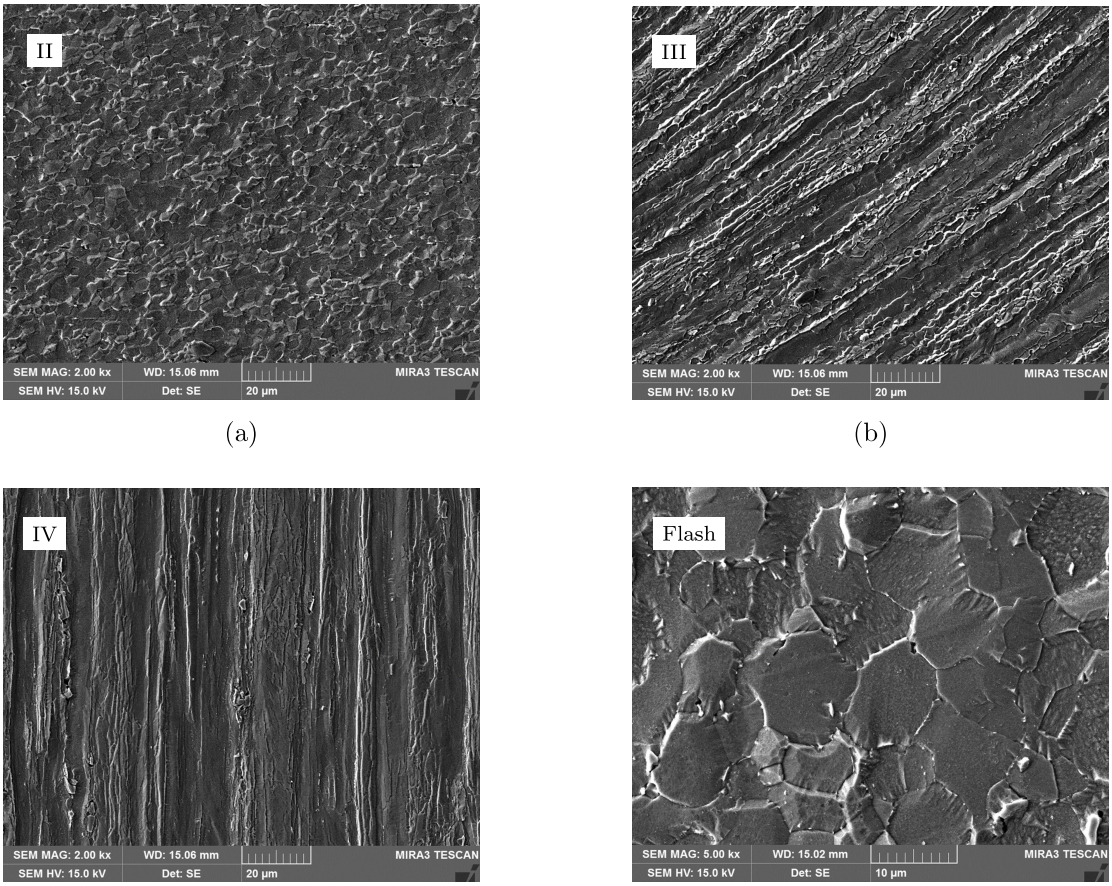

Figure 80: Scanning electron microscopy of etched (a) fully plasticized zone [murakami, 2000x magnification], (b) partially deformed zone [murakami, 2000x magnification], (c) base material [murakami, 2000x magnification] and (d) flash [murakami, 5000x magnification] of RFW TZM (2750 rpm)

Mechanical Characterisation The in transverse and longitudinal direction measured Vickers hardness HV1 reveals a similarly homogeneous hardness distribution, except the fully plasticized zone (fig. 81). This means that there is a slight deviation (tab. 11) of the average hardness value of the fully plasticized zone (310 ± 8 HV1) to the partly deformed zone (293 ± 8 HV1) and the undeformed zone/base material (292 ± 7 HV1). Considering the chemical composition of TZM and the finer grained microstructure (1.43 µm), it is likely that grain boundary strengthening and/or precipitation hardening may influence the mechanical properties within the fully plasticized zone.

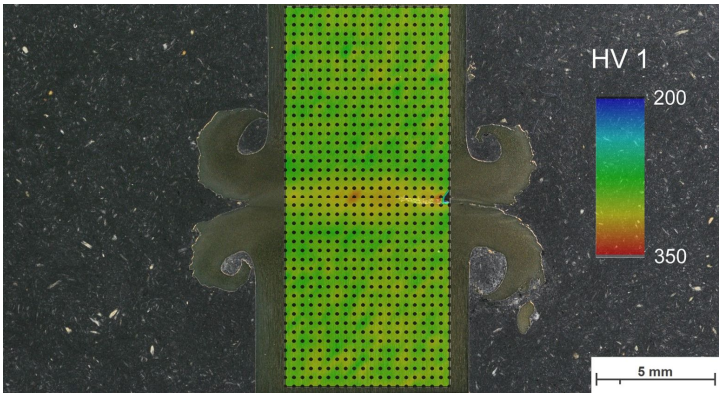

Figure 81: Hardness map and distribution RFW TZM

Table 11: Hardness values for representative weld sections RFW TZM

Weld Section	Average Hardness [HV1]	Standard Deviation Hardness [HV1]
Fully plasticized zone	310	± 8
Partially deformed zone	293	± 8
Undeformed zone and Base material	292	± 7

4.5 Comparison Molybdenum and TZM to LCS

In the conducted experiments it was observed that molybdenum and TZM reveal a completely different plasticization behavior compared to the reference low-carbon steel (fig. 82b). As a result, different process designs and welding parameters are required (fig. 82a). For the reference low-carbon steel, the so far established two level design with a friction pressure of 40 MPa and forging pressure of 200 MPa is suited in order to generate sound joints. The material displacement within the friction phase is characterized by a stable upset behavior (1.98 mm) and a moderate quasi-steady-state displacement-rate (6.01 mm/s). The subsequent transition ("forging into the turning spindle") from friction to forging pressure results in an initial increase of the maximum derived upset-rate (8.44 mm) and mainly determines the total material displacement (27.67 mm/s). Further, within the ongoing spindle deceleration in the forging phase, the actual power input decreases and the displacement-rate of low-carbon steel continuously drop to zero.

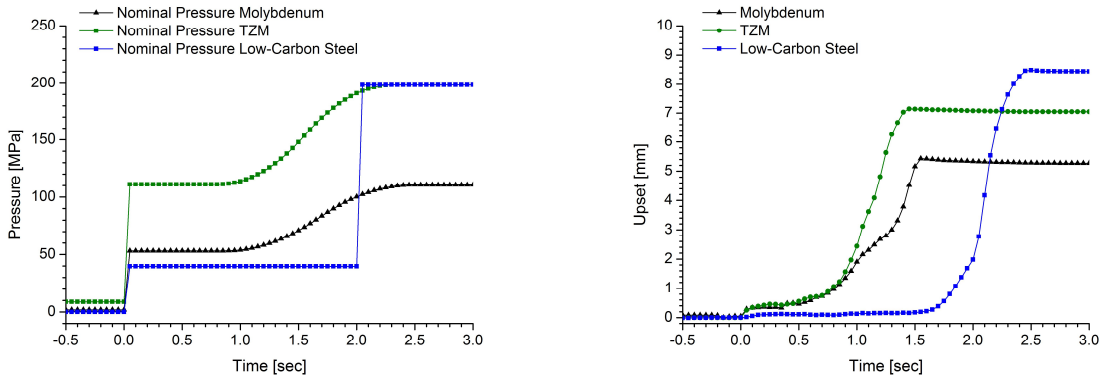

(a) (b)

Figure 82: (a) Nominal pressure and (b) recorded upset for comparison molybdenum and TZM to LCS

The conducted molybdenum pilot study revealed that a general different process design and additional welding parameters are required in order to join molybdenum metals. Molybdenum's intrinsic brittleness at room temperature, the maximum displacement-rate (24.64 mm/s) within the friction phase, and the instable and not fully controlled transition from friction to forging phase complicate the DDFW of molybdenum metals. To countervail the material's cold brittleness, the implemented preceding in-situ preheating routine increases the initial operating temperatures (DBTT) before the actual weld cycle starts. Further, the material's unique thermophysical and thermomechanical properties require a shorter process time and a controlled and concentrated energy input during the transition from friction to forging phase. The additionally implemented input parameters in the transition stage enable the mutual arrangement of the applied axial pressure with the current decelerated speed in order to control the power input

beyond the friction phase. Compared to commercially pure molybdenum (53 MPa / 110 MPa), a two times higher pressure level (110 MPa / 200 MPa) for DDFW TZM is needed to obtain a nearly similar upset response. The recorded material displacements for commercially pure molybdenum and TZM show dynamic upset behaviors and are accompanied by maximum upset-rates (molybdenum 13.69 mm/s, TZM 15.46 mm/s) close to the spindle stop. In order to identify feasible input parameters and to keep the material plasticization manageable, a comprehensive and precise machine control is needed.

In addition, the different material behavior during DDFW is also reflected by the recorded typical thermal cycles for the particular materials (fig. 83). To reconstruct the temperature history, selected stationary weld pins were equipped with thermocouples in 2 mm and 10 mm distance to the weld interface.

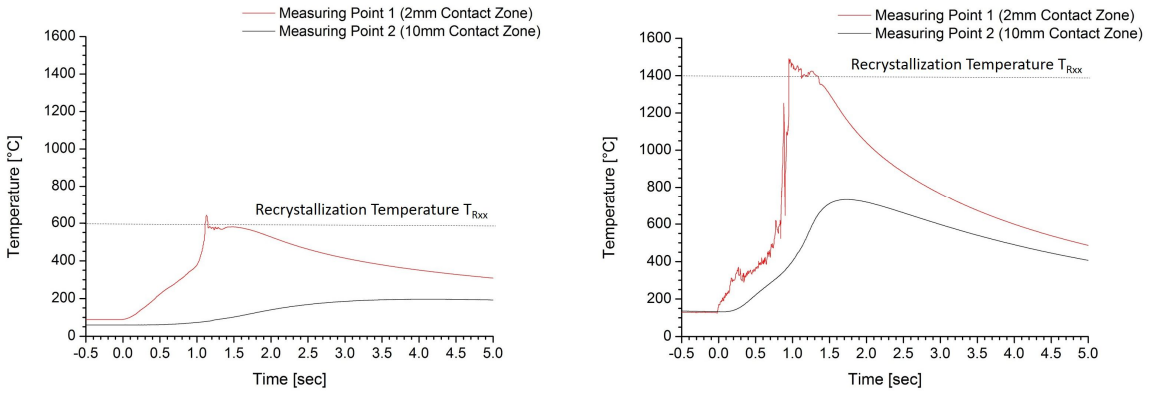

Figure 83: Recorded thermal cycles: (a) Low-carbon steel and (b) TZM

The logged temperature curves reveal a completely different temperature evolution within the molybdenum alloy and the low-carbon steel weld specimens, and prove the major impact of the thermophysical properties (tab. 12) on the friction welding process. The recorded maximum process temperatures are in the range of the particular material's recrystallization temperature T_{Rxx}. Further, considering the recorded temperature histories, it is assumed that the material's specific heat capacity c mainly determines the difference between the recorded temperature peaks, whereas the thermal conductivity λ defines the time shift between the recorded temperature peaks. The thermal diffusivity α combines these thermophysical properties and is considered as a measure for the heat transfer rate and thermal inertia. Molybdenum exhibits a nearly four times higher thermal diffusivity compared to the reference low-carbon steel.

Table 12: Selected properties of stress relieved molybdenum, stress relieved TZM and AISI 1000 series of low-carbon steels at room temperature [83]

	Molybdenum Stress Relieved	TZM Stress Relieved	AISI 1000 Series
Recrystallization temperature T_{Rxx} [°C]	1,000-1,200	1,400-1,500	600-700
Thermal conductivity λ [W/m K]	138	118	55
Specific thermal capacity c [J/g K]	0.255	0.250	0.511
Density ρ [g/cm^3]	10.22	10.16	7.85
Thermal diffusivity α [10^{-6} m^2/s]	53	47	14

In terms of direct drive friction welding and the observed vigorous plasticization behaviour of molybdenum metals, themophysical and thermomechanical properties could be linked and a reasonable principle was formulated: “The thermal diffusivity determines the manifesting temperature field. The temperature field governs plasticization, which starts when a certain temperature is exceeded. That means for Mo and TZM with their high thermal diffusivities, a large volume starts to plasticize suddenly, which may cause instable process conditions. As a consequence, friction welding of Mo and TZM requires the energy input to be rapid and thus the process time to be short to produce a high spatial temperature gradient in the weld specimen.” [89]

5 Summary

Rotary friction welding was performed on commercially pure molybdenum, Titanium-Zirconium-Molybdenum (TZM) and a reference low-carbon steel (LCS) by the means of a friction stir welding (FSW) device providing comprehensive parameter recording. The FSW device was adjusted to resemble a direct drive friction welding (DDFW) process and a general machine capability for rotary friction welding (RFW) was proven by the joining of a reference low-carbon steel.

For the low-carbon steel study, the established two level process design and technique "forging into the turning spindle" were applied and resulted in the generation of sound and defect free joints. Within the defined process parameter window, the amount of total upset was mainly determined by the amount of forge upset. An in-depth analysis of selected weld specimens was conducted in order to describe the material's behavior during processing. The maximum material displacement-rate (6.01 mm/s) in the friction phase is restricted by the maximum initial nominal torque and therefore power input. By passing the maximum power peak, the nominal torque input was stabilized and dropped to an equilibrium level. The observed friction phase indicated a self-regulation effect, which is represented by a quasi-steady-state material displacement-rate (3.85 mm/s) and stable upset. The subsequent forging phase was initiated by the start of spindle deceleration and simultaneous increase of pressure to the forge level. The introduced "power burst" resulted in a maximum overall upset-rate (27.67 mm/s) and mainly determined the final upset. Generated joints were characterized by a narrow weld seam and a for the process distinct microstructure. The temperature evolution within the material resulted in a non-uniform microstructure in transverse direction. Towards the center of the weld interface, the circumference of the weld interface presented a fully recovered/recrystallized microstructure in a wide range. Mechanical properties, characterized by means of hardness measurements, reflected the change in microstructure. The hardness evolution of the weldment increased from the unaffected parent metal (175 $\pm$ 12 HV1) toward the contact zone. The highest hardness levels was measured within the fully plasticized zone (265 $\pm$ 45 HV1).

The preceding pilot study revealed that friction welding of molybdenum metals is much more demanding than for the reference low-carbon steel. The susceptibility for brittle fracture at room temperature, the vigorous plasticization behavior (24.64 mm/s) within the friction phase, and an instable forging condition during the transition from friction to forging phase were the challenges to deal with. A general re-design of the so far established two level process was required. An additionally implemented in-situ pre-heating routine provided a sufficient level of initial operating temperature ($\approx$ 350 °C) in order to exceed the ductile-brittle transition temperature (DBTT) and enabled a continuous weld process. Short welding cycles were selected to oppose the heat dissipation and to keep the material's plasticization manageable. The transition stage was adjusted and additional input parameters were implemented to fine tune the process design.

The revised process design was applied for commercially pure molybdenum and TZM weld specimens. In order to achieve a nearly similar upset response, TZM required a two times higher pressure level (110 MPa / 200 MPa). To obtain a variety in plasticization, three different rotational speeds (2500 rpm, 2600 rpm, and 2750 rpm) were applied and their recorded output parameters analyzed. Within the conducted experiments, the molybdenum metals revealed a dynamic plasticization behavior and increased displacement-rates (molybdenum 13.69 mm/s, TZM 15.46 mm/s) especially close to the end of the spindle deceleration at a minimal power input. The derived upset over total energy courses indicated that at least a minimum amount of weld energy within a process time of approximately 1.6 s was needed to initiate the sudden and steep material plasticization. The generated molybdenum and TZM joints were assessed with respect to their integrity, microstructure, and microstructural changes. For the molybdenum weld specimens, a minimum maintained specific total energy of 71 J/mm^2 was required to produce a sound and defect free bond over the entire weld interface. That accounts to a maximum specific power peak of approximately 80 W/mm^2 within the weld cyle. In contrast, a presence of imperfections in all of the TZM weldments were observed. The mainly asymetric kissing bonds were attributed to the angular misalignment of the weld pin axes, caused by the heavier loading condition. The joints were characterized by an expanded HAZ and the formation of the for friction welding characteristic weld sections. Light optical microscopy (LOM) and scanning electron microscopy (SEM) examinations of the regions next to the weld interface center revealed the continuous re-alignment of the molybdenum metals' distinct hot-worked microstructure outwards in direction of the plastic flow in the partly deformed zone. The increased temperature, strain, and strain rate resulted in a complete annihilation of the prior microstructure and formed a new equiaxed, fine grained microstructure. The grain size within the fully plasticized zone was determined by the means of electron backscatter diffraction (EBSD) and returned an average value of 4.39 µm for molybdenum and 1.43 µm for TZM. It was concluded that the increased recrystallization temperature of TZM and occurring degrees of deformation inhibited an actual grain growth. The evolution of microstructure within the weldment was only partially reflected by the logged hardness distribution. While the molybdenum weld specimen revealed a homogeneous hardness distribution ($\approx$ 245 HV1) over the entire cross-section, TZM showed a slight increase of the fully plasticized (310 $\pm$ 8 HV1) compared to the other weld sections ($\approx$ 292 HV1).

Finally, the representative process design, related material displacement, and recorded temperature history of molybdenum metals and the reference low-carbon steel were opposed. Whereas the so far established two level process design was suited to generate sound low-carbon steel joints, an adjusted process design for rotary friction welding of molybdenum metals was mandatory. The related material displacements revealed a completely different plasticization behavior and increased displacement-rates of molybdenum metals compared to the reference low-carbon steel. In addition, the different material behavior during DDFW was also reflected by their logged typical thermal cycles. The recorded maximum temperature peaks at the initial plasticization were in the range of

the particular recrystallization temperature and the temperature evolution in the ongoing process was determined by the material's thermophysical properties specific heat capacity c and thermal conductivity λ. In case of molybdenum alloys, a larger volume was heated up in a shorter period, exceeded the critical shear strength, and started to plasticize.

6 Outlook

Based on the selected input parameters and derived technical information from the small-scale molybdenum experiments (113 mm^2), an adjustment of the established two level process design and an enhanced drive power of the machine (150 kW) is recommended to enable direct drive friction welding of large cross-sections (4,400 mm^2) [68]. By linear extrapolation of the previous determined values for specific total energy input (71 J/mm^2) and specific maximum power input ($\approx$ 80 W/mm^2), the application of at least a 350 kW RFW machine is needed in order to maintain a total weld energy input of $\approx$ 320 kJ without the observed spindle stall during plasticization. For the actual welding process, short welding cycles at high pressure levels are preferable to oppose the heat dissipation by a concentrated and controlled power input. Therefore, special attention should be paid on the transition from friction to forging phase and the mutual arrangement of the applied forging pressure to the continuously decelerated rotational speed. Further, an adaption of the process design is suggested and the implementation of an in-situ pre-heating routine recommended. Compared to common techniques (e.g. pre-heating in the furnace), the low-pressure pre-heating routine enables a continuous welding process and therefore reproducible pre-heating temperatures. For the future, to confirm the presented findings of this work and to verify the results of the small-scale experiment, additional welding experiments with varying cross-sections, e.g. medium-size samples (e.g. 1,200 mm^2) on the heavy-duty (150 kW) direct drive friction welding machine, are recommended.

Additionally to the conventional characterization by scanning electron microscopy (SEM) and light optical microscopy (LOM), the application of more sophisticated techniques i.e. electron backscatter diffraction (EBSD), transmission electron microscopy (TEM) and neutron diffraction (ND) would be beneficial to gather additional information especially from the fully plasticized zone considering the misorientation distribution, formation of precipitations, and residual stresses.

Furthermore, for a deeper understanding of the plasticization behavior of molybdenum and Titanium-Zirconium-Molybdenum (TZM), numerical simulation will be an important asset. A reliable numerical model would evaluate the particular influence of the input parameters on the upset response with a minimal effort. Still, a feasible heat source model and material properties, especially temperature- and strain-rate dependent flow curves over a wide temperature range (>1200 °C) are needed.

References

[1] E. M. Savitskii and G. S. Burkhanov. *Physical Metallurgy of Refractory Metals and Alloys.* Springer US, Boston, MA, 1970.

[2] J. A. Shields. *Applications of Molybdenum Metal and its Alloys.* International Molybdenum Association, 2013.

[3] W. Martienssen and H. Warlimont. *Springer Handbook of Condensed Matter and Materials Data*, Springer Berlin Heidelberg. 2005.

[4] Plansee SE. *Available: https://www.plansee.com/en/materials/molybdenum.html.* Accessed: Aug 2017.

[5] MolyMet. *Available: https://www.molymet.cl.en.* Accessed: Aug 2017.

[6] S. Primig, H. Leitner, A. Rodriguez-Chavez, H. Clemens, A. Lorich, W. Knabl and R. Stickler. *On the Recrystallization Behavior of Technically Pure Molybdenum.* International Journal for Refractory Metals and Hard Materials, vol. 28, pp. 703-708, 2010.

[7] W. C. Hagel, J. A. Shields and S.M. Tuominen. *Processing and production of molybdenum and tungsten alloys.* Refractory alloy technology for space nuclear power applications, vol. 15, pp. 98-113, 1984.

[8] I. Wesemann, A. Hoffmann, T. Mrotzek and U. Martin. *Investigation of Solid Solution Hardening in Molybdenum Alloys.* International Journal for Refractory Metals and Hard Materials, vol. 28, pp. 709-715, 2010.

[9] S. V. Nagender Naidu, A. M. Sriramamurthy and P. Rama Rao. *The Mo-W (Molybdenum-Tungsten) System.* Bulletin of Alloy Phase Diagrams, vol. 5, pp. 177-180, 1984.

[10] W. Hume-Rothery and H. M. Powell. *On the Theory of Super-Lttice Structures in Alloys.* Zeitschrift für Kristallographie - Crystalline Materials, vol. 91, pp. 23-47, 1935.

[11] W. Hume-Rothery, C. W. Haworth and R. E. Smallman. *The structure of metals and alloys.* Institute of Metals and the Institution of Metallurgists, 5th ed., 1969.

[12] V. T. Troshchenko, N. D. Bega, E. É. Zasimchuk and L. A. Khamaza. *Some features of work hardening and softening of molybdenum single crystals in cyclic strain.* Strength of Materials, vol. 11, pp. 163-168, 1979.

[13] H. W. Loesch Jr. and F.R. Brotzen. *Observation of dislocations in deformed molybdenum crystals.* Journal of the Less Common Metals, vol. 13, pp. 565-578, 1967.

[14] A. Luft and L. Kaun. *Electron Microscopic Investigation of the Dislocation Structure in Molybdenum Single Crystals Deformed in Tension at 293 and 493 °K.* physica status solidi, vol. 37, pp. 781-793, 1970.

[15] A. Luft. *Microstructural processes of plastic instabilities in strengthened metals.* Progress in Materials Science, vol. 35, pp. 97-204, 1991.

[16] M. M. Myshlyaev, I. I. Khodos, O. N. Sen'kov and Y. A. Romanov. *Dislocation structure of fragment boundaries in molybdenum and tungsten single crystals.* Physics of Metals and Metallography, vol. 11, pp. 1086-1098, 1979.

[17] G. Malakondaiah and P. Rama Rao. *Effect of Grain Size, Grain Shape and Subgrain Size on High Temperature Creep Behaviour.* Defence Science Journal, vol. 35, pp. 201-217, 1985.

[18] T. Mrotzek, A. Hoffmann and U. Martin. *Hardening mechanisms and recrystallization behaviour of several molybdenum alloys.* International Journal for Refractory Metals and Hard Materials, vol. 24, pp. 298-305, 2006.

[19] M. Nagae, T. Yoshio, J. Takada and Y. Hiraoka. *Improvement in Recrystallization Temperature and Mechanical Properties of a Commercial TZM Alloy through Microstructure Control by Multi-Step Internal Nitriding.* Materials Transactions, vol. 46, pp. 2129-2134, 2005.

[20] J. Warren. *The 700°C tensile behavior of Mo-0.5Ti-0.08Zr-0.025C (TZM) extruded bar measured transverse and parallel to the billet extrusion axis.* International Journal for Refractory Metals and Hard Materials, vol. 16, pp. 149-157, 1998.

[21] J. Warren and G. Reznikov. *A comparison of the microstructure and high temperature tensile properties of a novel P/M Mo-Hf-Zr-Ta-C alloy and TZM.* 15th International Plansee Seminar, vol. 4, pp. 79-94, 2001.

[22] T. Mrotzek,U. Martin and A. Hoffmann. *High temperature deformation behavior of the molybdenum alloy TZM.* Journal of Physics: Conference Series, vol. 240, 2010.

[23] T. Mrotzek,I. Wesemann, A. Hoffmann and U. Martin. *Investigation of Hardening Mechanisms in Powder-Metallurgical Molybdenum Alloys.* PM2010 Word Congress - Tungsten & Molybdenum Alloys, pp. 9-16, 2010.

[24] S. Majumdar, S. Raveendra, I. Samajdar, P. Bhargava and I. G. Sharma. *Densification and grain growth during isothermal sintering of Mo and mechanically alloyed Mo–TZM.* Acta Materialia, vol. 57, pp. 4158-4168, 2009.

[25] A.J. Mueller, R. Bianco and W. R. Buckman Jr.. *Evaluation of oxide dispersion strengthened (ODS) molybdenum and molybdenum–rhenium alloys.* International Journal for Refractory Metals and Hard Materials, vol. 18, pp. 205-211, 2000.

[26] R. Bianco,W. R. Buckman Jr. and C. B. Geller. *High-strength, creep-resistant molybdenum alloy and process for producing the same.* U.S. Patent 5868876A, issued May, 1997.

[27] G. Leichtfried and S. Wetzel. *Kriechfeste Molybdänwerkstoffe basierend auf verformbaren oxidischen Dispersoiden.* 12th International Plansee Seminar, vol. 1, pp. 1023-1046, 1989.

[28] M. Endo, K. Kimura, T. Udagawa, S. Tanabe and H. Seto. *The effects of doping molybdenum wire with rare earth elements.* 12th International Plansee Seminar, vol. 1, pp. 37-53, 1989.

[29] R. Bianco and W. R. Buckman Jr.. *Evaluation of oxide dispersion strengthened (ODS) molybdenum alloys.* ASM/TMS symposium on high-temperature materials, 1995.

[30] B. V. Cockeram and K. S. Chan. *In-Situ Fracture Studies and Modeling of the Toughening Mechanism Present in Wrought Low-Carbon Arc-Cast Molybdenum, Titanium-Zirconium-Molybdenum, and Oxide-Dispersion-Strengthened Molybdenum Flat Products.* Metallurgical and Materials Transactions A, vol. 39, pp. 2045-2067, 2008.

[31] G. Leichtfried. *Molybdenum Lanthanum Oxide - Special Material Properties by Dispersoid Refining during Deformation.* Advances in Powder Metallurgy & Particulate Materials, vol. 9, pp. 123-138, 1992.

[32] G. Leichtfried, G. Thurner and R. Weirather. *Molybdenum alloys for glass-to-metal seals.* International Journal for Refractory Metals and Hard Materials, vol. 16, pp. 13-22, 1998.

[33] R. Baranwal and M. G. Burke. *Transmission electron microscopy of oxide dispersion strengthened (ODS) molybdenum: effects of irradiation on material microstructure.* Philosophical Magazine, vol. 85, pp. 519-531, 2005.

[34] A. Kumar and B. L. Eyre. *Grain Boundary Segregation and Intergranular Fracture in Molybdenum.* Proceedings of the Royal Society of London. Series A, Mathematical and Physical Sciences, vol. 370, pp. 431-458, 1980.

[35] M. Oku and S. Suzuki. *Chemical states of oxygen segregated intergranular fracture surface of molybdenum.* Applied Surface Science, vol. 26, pp. 42-50, 1986.

[36] M. K. Miller and A. J. Bryhan. *Effect of Zr, B and C additions on the ductility of molybdenum.* Materials Science and Engineering: A, vol. 327, pp. 80-83, 2002.

[37] O. Lenchuk, J. Rohrer and K. Albe. *Cohesive strength of zirconia/molybdenum interfaces and grain boundaries in molybdenum: A comparative study.* Acta Materialia, vol. 135, pp. 150-157, 2009.

[38] D. Scheiber, R. Pippan, R. Puschnig, and L. Romaner. *Ab initio search for cohesion-enhancing impurity elements at grain boundaries in molybdenum and tungsten.* Modelling and Simulation in Materials Science and Engineering, vol. 24, 2016.

[39] H. Saage, M. Krüger, D. Sturm, M. Heilmaier, J. H. Schneibel, E. George, L. Heatherly, C. Somsen, G. Eggeler and Y. Yang. *Ductilization of Mo–Si solid solutions manufactured by powder metallurgy.* Acta Materialia, vol. 57, pp. 3895-3901, 2009.

[40] K. Leitner, D. Scheiber, S. Jakob, S. Primig, H. Clemens, E. Povoden-Karadeniz and L. Romaner. *How grain boundary chemistry controls the fracture mode of molybdenum.* Materials and Design, vol. 142, pp. 36-43, 2018.

[41] C. Gandhi and M. F. Ashby. *Fracture-Mechanics Maps for Materials Which Cleave: FCC, BCC and HCP Metals and Ceramics.* Acta Metall, vol. 27, pp. 1565-1602, 1979.

[42] S. Suzuki, H. Matsui and H. Kimura. *The effect of heat treatment on the grain boundary fracture of recrystallized molybdenum.* Materials Science and Engineering, vol. 47, pp. 209-216, 1981.

[43] K. Babinsky, S. Primig, W. Knabl, A. Lorich, R. Stickler and H. Clemens. *Fracture Behavior and Delamination Toughening of Molybdenum in Charpy Impact Tests.* The Journal of The Minerals, Metals & Materials Society (TMS), vol. 68, pp. 2854-2863, 2016.

[44] S. Tsurekawa, T.Tanaka and H.Yoshinaga. *Grain boundary structure, energy and strength in molybdenum.* Materials Science and Engineering: A, vol. 176, pp. 341-348, 2004.

[45] B. V. Cockeram, E. K. Ohriner, T. S. Byun, M. K. Miller and L. L. Snead. *Weldable ductile molybdenum alloy development.* Journal of Nuclear Materials, vol. 382, pp. 229-241, 2008.

[46] G. Liu, G. J. Zhang, F. Jiang, X. D. Ding, Y. J. Sun, J. Sun and E. Ma. *Nanostructured high-strength molybdenum alloys with unprecedented tensile ductility.* Nature Materials, vol. 12, pp. 344-350, 2013.

[47] A. J. Bryhan. *Joining of molybdenum base metals and factors which influence ductility.* WRC Bulletin Series, vol. 312, pp. 1-9, 1986.

[48] J. S. Hirschhorn. *Stacking faults in the refractory metals and alloys — A review.* Journal of the Less Common Metals, vol. 5, pp. 493-509, 1963.

[49] V. Guttmann. *Keimbildung bei der Rekristallisation von Molybdän.* Journal of the Less Common Metals, vol. 21, pp. 51-61, 1970.

[50] S. Primig, H. Leitner, W. Knabl, A. Lorich and R. Stickler. *Static Recrystallization of Molybdenum After Deformation Below 0.5*T_M (K).* Metallurgical and Materials Transactions A, vol. 43, pp. 4806-4818, 2012.

[51] S. Primig, H. Leitner, W. Knabl, A. Lorich, H. Clemens and R. Stickler. *Textural Evolution During Dynamic Recovery and Static Recrystallization of Molybdenum.* Metallurgical and Materials Transactions A, vol. 43, pp. 4794-4805, 2012.

[52] S. Primig, H. Leitner, W. Knabl, A. Lorich, H. Clemens and R. Stickler. *Orientation dependent recovery and recrystallization behavior of hot-rolled molybdenum.* International Journal for Refractory Metals and Hard Materials, vol. 48, pp. 179-186, 2015.

[53] R. Lison. *Schweißen und Löten von Sondermetallen und ihren Legierungen.* Fachbuchreihe Schweißtechnik, vol. 118, 1996.

[54] B. Tabernig and N. Reheis. *Joining of molybdenum and its application.* International Journal for Refractory Metals and Hard Materials, vol. 28, pp. 728-733, 2010.

[55] J. Wadsworth, G. R. Morse and P. M. Chewey. *The microstructure and mechanical properties of a welded molybdenum alloy.* Materials Science and Engineering, vol. 59, pp. 257-273, 1983.

[56] J. R. Stephens and W. W. Witzke. *Alloy hardening and softening in binary molybdenum alloys as related to electron concentration.* Journal of the Less Common Metals, vol. 29, pp. 371-388, 1972.

[57] R.Eck. *Molybdän-Rhenium Legierungen als schweissbare Hochtemperatur-Konstruktionswerkstoffe.* 11th International Plansee Seminar, vol. 1, pp. 39-57, 1985.

[58] A. J. Bryhan. *The Room Temperature Ductility of Molybdenum-Base Weldments.* The Journal of The Minerals, Metals & Materials Society (TMS), vol. 37, pp. 36-40, 1985.

[59] M. K. Miller, E. A. Kenik, M. S. Mousa, K. F. Russell and A. J. Bryhan. *Improvement in the ductility of molybdenum alloys due to grain boundary segregation.* Scripta Materialia, vol. 46, pp. 299-303, 2002.

[60] B. S. Yilbasa, M. Samia, J. Nickelb, A. Cobanb and S. A. M. Saida. *Introduction into the electron beam welding of austenitic 321-type stainless steel.* Journal of Materials Processing Technology, vol. 82, pp. 13-20, 1998.

[61] M. Stütz, D. Oliveira, M. Rüttinger, N. Reheis, H. Kestler and N. Enzinger. *Electron Beam Welding of TZM Sheets.* Materials Science Forum, vol. 879, pp. 1865-1869, 2016.

[62] M. Kolaříková, L. Kolařík and P. Vondrouš. *Mechanical Properties of Mo Weld Joint Produced by EBW and GTAW Methods.* International Journal of Science Commerce and Humanities, vol. 1, pp. 148-152, 2013.

[63] A. Chatterjee, S. Kumar, R. Tewari and G. K. Dey. *Welding of Mo-Based Alloy Using Electron Beam and Laser-GTAW Hybrid Welding Techniques.* Metallurgical and Materials Transactions A, vol. 47, pp. 1143-1152, 2016.

[64] Y. Zhang, T. Wang, S. Jiang, B. Zhang, Y. Wang and J. Feng. *Microstructure evolution and embrittlement of electron beam welded TZM alloy joint.* Materials Science and Engineering: A, vol. 700, pp. 512-518, 2017.

[65] T. Wang, N. Li, Y. Zhang, S. Jiang, B. Zhang, Y. Wang and J. Feng. *Influence of welding speed on microstructures and mechanical properties of vacuum electron beam welded TZM alloy joints.* Vacuum, vol. 149, pp. 29-35, 2018.

[66] T. Wang, Y. Zhang, S. Jiang, X. Li, B. Zhang and J. Feng. *Stress relief and purification mechanisms for grain boundaries of electron beam welded TZM alloy joint with zirconium addition.* Journal of Materials Processing Technology, vol. 251, pp. 168-174, 2018.

[67] D. de Pretis, N. Reheis, B. Tabernig, H. Kestler, L. S. Sigl and N. Enzinger. *Friction Welding of TZM Components.* Proceeding 2014 World Congress on Powder Metallurgy and Particulate Materials, vol. 8, pp. 51-58, 2014.

[68] M. Stütz, N. Enzinger, J. Wagner, N. Reheis, H. Kestler, E. Raiser. *Rotary Friction Welding of Large Molybdenum Tubes.* Proceeding 10th International Conference on Trends in Welding Research, pp. 153-156, 2016.

[69] A. Ambroziak. *Friction welding of molybdenum to molybdenum and to other metals.* International Journal for Refractory Metals and Hard Materials, vol. 9, pp. 462-469, 2011.

[70] *ASM Handbook: Welding, Brazing and Soldering.* vol. 6, 1993.

[71] M. M. Schwartz. *Metals Joining Manual.* 1979.

[72] W. Li, A. Vairis, M. Preuss and T. Ma. *Linear and rotary friction welding review.* International Materials Reviews, vol. 61, pp. 71-100, 2016.

[73] M. Maalekian. *Friction welding – critical assessment of literature.* Science and Technology of Welding and Joining, vol. 12, pp. 738-759, 2007.

[74] I. Bhamji, M. Preuss, P. L. Threadgill and A. C. Addison. *Solid state joining of metals by linear friction welding: a literature review.* Materials Science and Technology, vol. 27, pp. 2-12, 2013.

[75] M. B. Uday, M. N. Ahmad Fauzi, H. Zuhailawati and A. B. Ismail. *Advances in friction welding process: a review.* Science and Technology of Welding and Joining, vol. 15, pp. 534-558, 2013.

[76] A. R. McAndrew, P. A. Colegrove, C. Bühr, B. C. D. Flipo and A. Vairis. *A literature review of Ti-6Al-4V linear friction welding.* Progress in Materials Science, vol. 92, pp. 225-257, 2018.

[77] J. E. Gould. *Mechanisms of bonding for solid-state welding processes.* ASM Conference Proceedings: Joining of Advanced and Specialty Materials, pp. 89-97, 2001.

[78] P. K. Wright, D. A. Snow and C. K. Tay. *Interfacial conditions and bond strength in cold pressure welding by rolling.* Metals Technology, vol. 5, pp. 24-31, 1978.

[79] N. Bay. *Mechanisms producing metallic bonds in cold welding.* Welding Journal, vol. 62, pp. 137-142, 1983.

[80] H. A.Mohamed and J. Washburn. *Mechanism of Solid State Pressure Welding* . Welding Journal, vol. 54, pp. 302-310, 1975.

[81] Y. Takahashi and K. Inoue. *Recent void shrinkage models and their applicability to diffusion bonding.* Materials Science and Technology, vol. 8, pp. 953-964, 1992.

[82] Y. Takahashi, K. Inoue and K. Nishiguchi. *Identification of void shrinkage mechanisms.* Acta Metallurgica et Materialia, vol. 41, pp. 3077-3084, 1993.

[83] MatWeb Overview of materials for AISI 1000 Series Steel . *Available: https://www.matweb.com.* Accessed: Dez 2017.

[84] Thermocouple info. *Available: https://www.thermocoupleinfo.com/type-k-thermocouple.htm and https://www.thermocoupleinfo.com/type-s-thermocouple.htm.* Accessed: Dec 2017.

[85] M. Abramowitz and I. A. Stegun. *Handbook of Mathematical Functions: with Formulas, Graphs, and Mathematical Tables*, New York: Dover. vol. 9, p. 14, 1972.

[86] Merkblatt DVS 2909-5. *Reibschweißen von metallischen Werkstoffen; Bewertungsgruppen für das Rotationsreibschweißen.* issue 2005.

[87] G. Petzow. *Metallographisches, keramographisches, plastographiches Ätzen* . Materialkundlich-Technische Reihe, 1994.

[88] V. I. Vill. *Friction welding of metals.* New York American Welding Society, 1962.

[89] M. Stütz, F. Pixner, J. Wagner, N. Reheis, E. Raiser, H. Kestler and N. Enzinger. *Rotary friction welding of molybdenum components.* 19th International Plansee Seminar, 2017.

Appendix

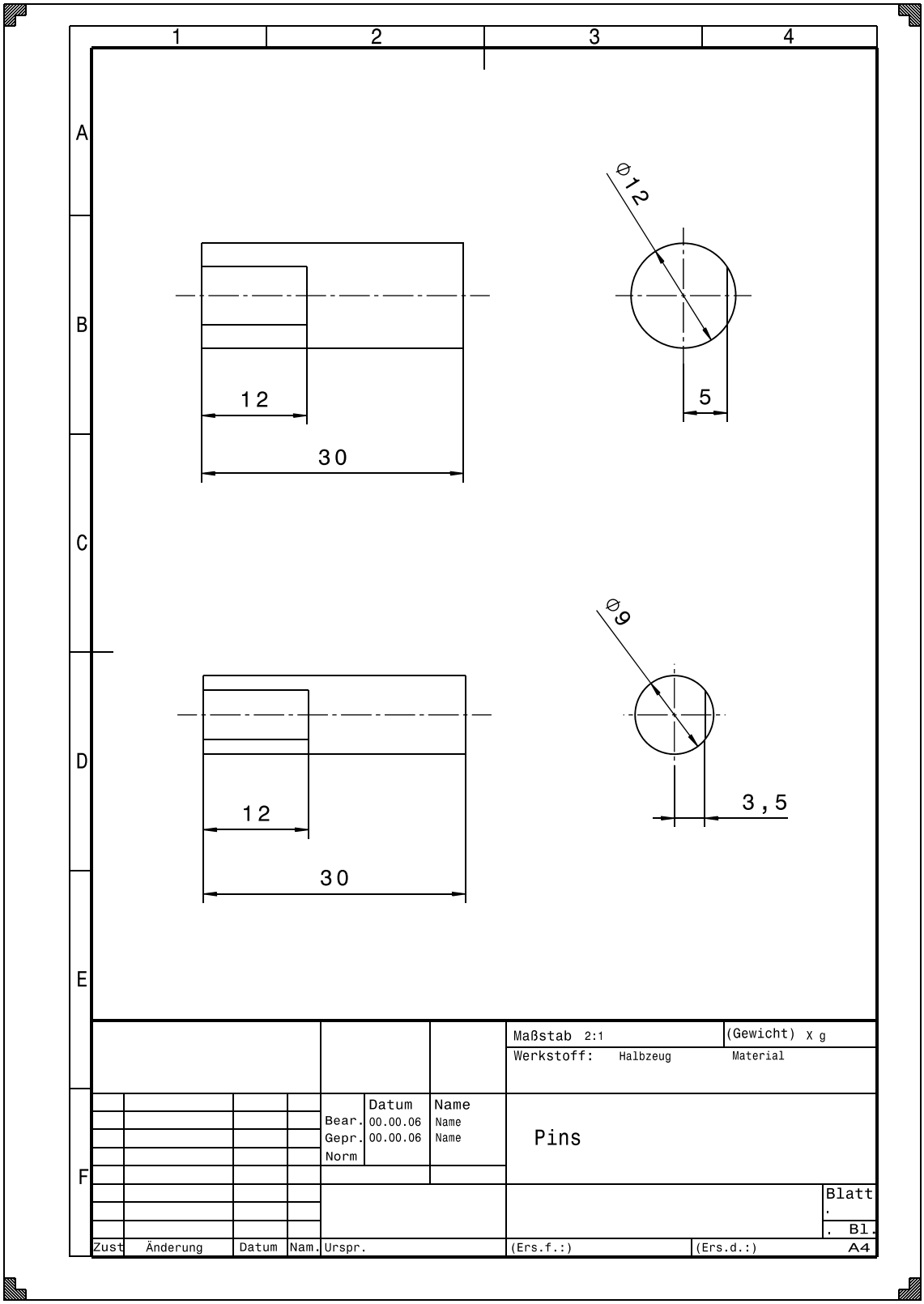
1
2
3
4
A
B
C
D
E
F
⌀12
12
30
5
⌀9
12
30
3,5
Maßstab 2:1
(Gewicht) X g
Werkstoff: Halbzeug Material
Bear. Datum Name
Gepr. 00.00.06 Name
Norm 00.00.06 Name
Pins
Blatt .
. Bl.
Zust Änderung Datum Nam. Urspr.
(Ers.f.:) (Ers.d.:) A4

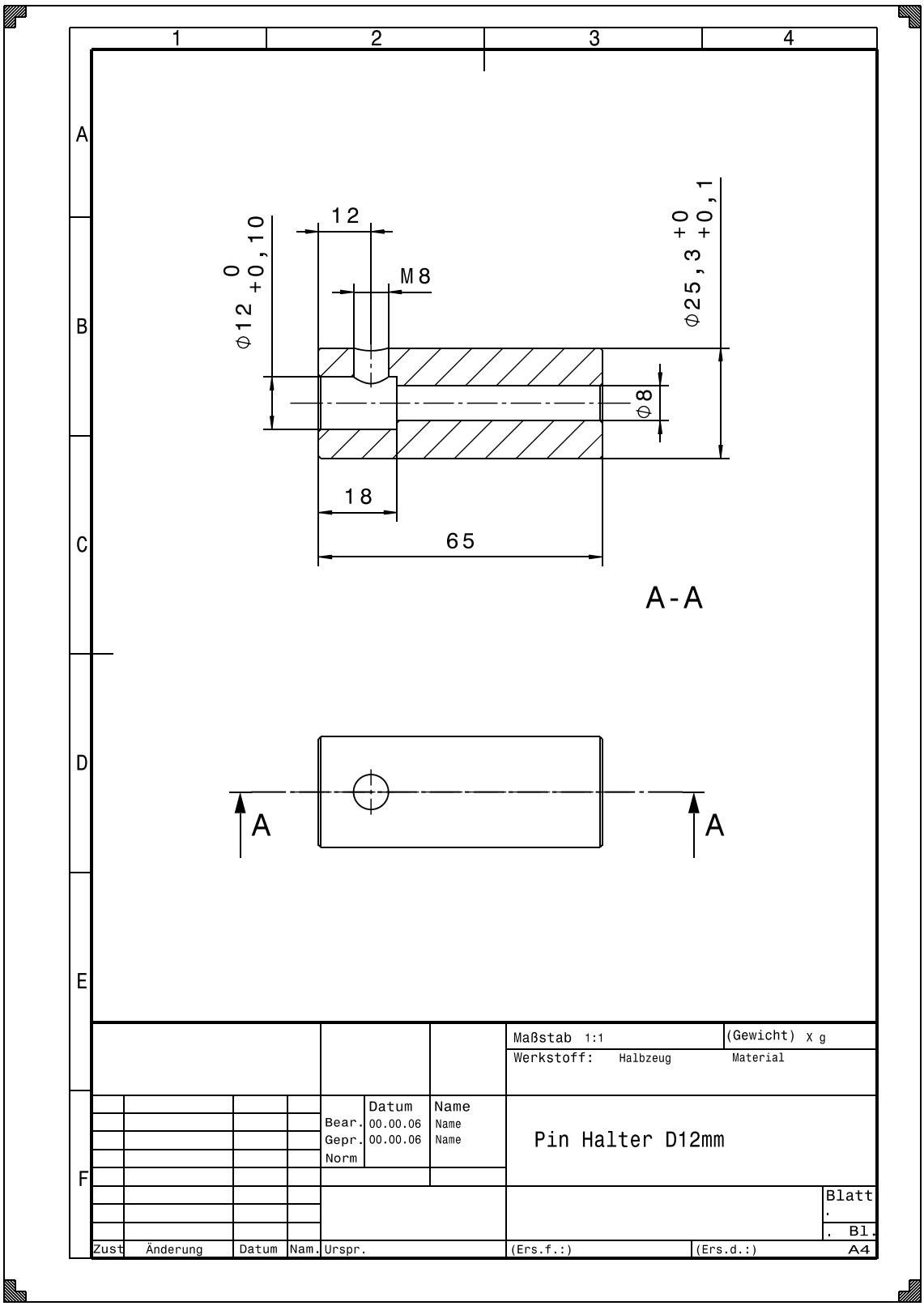
1
2
3
4
A
B
C
D
E
F
12
M8
Φ12 +0,10 0
Φ25,3 +0,1 +0
Φ8
18
65
A-A
A
A
Maßstab 1:1
(Gewicht) X g
Werkstoff: Halbzeug Material
Bear. Datum Name
Gepr. 00.00.06 Name
Norm 00.00.06 Name
Pin Halter D12mm
Blatt .
. Bl.
Zust Änderung Datum Nam. Urspr.
(Ers.f.:) (Ers.d.:) A4

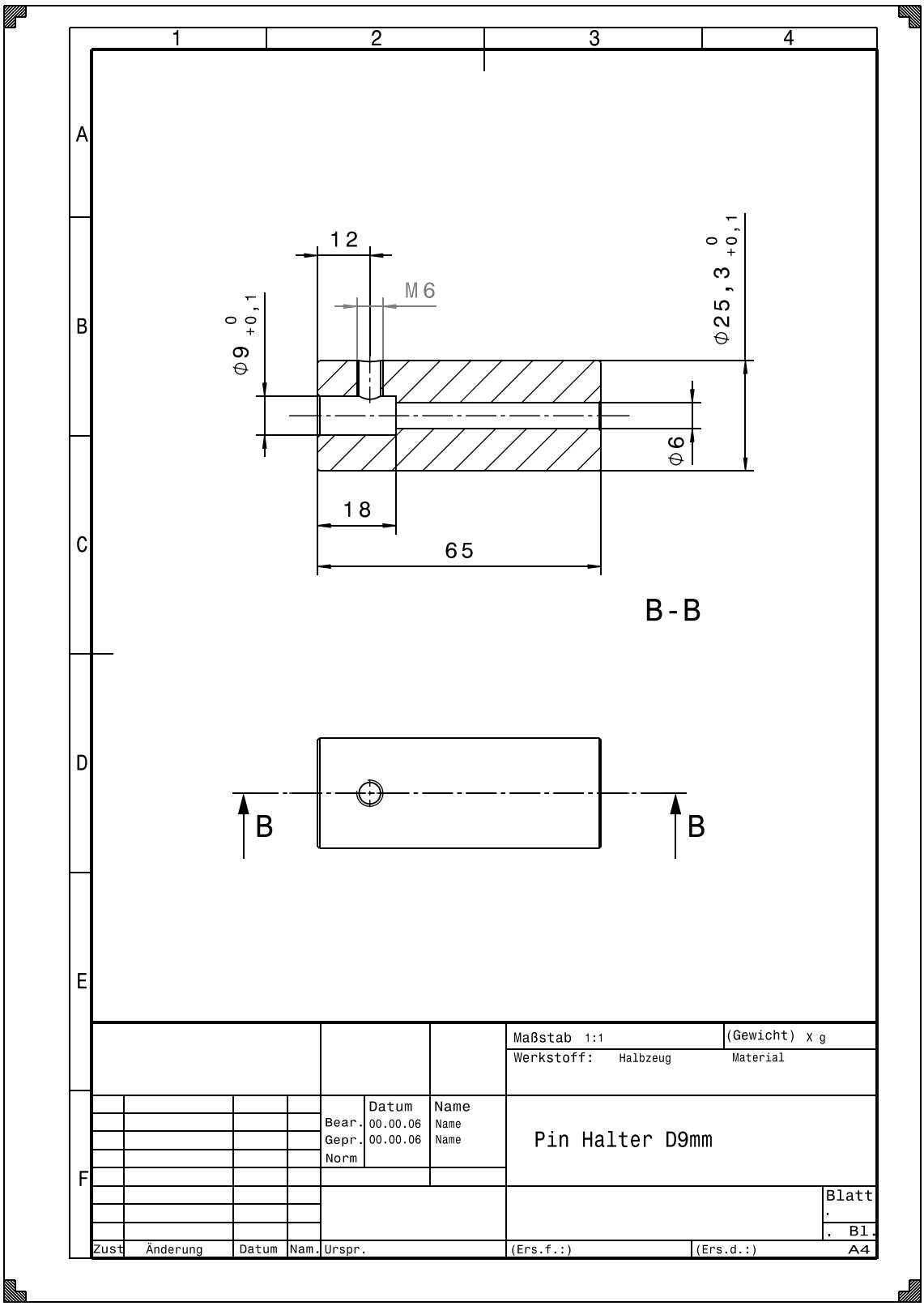
1
2
3
4
A
B
C
D
E
F
12
M6
ϕ9 0 +0,1
ϕ25,3 0 +0,1
ϕ6
18
65
B-B
B
B
Maßstab 1:1
(Gewicht) X g
Werkstoff: Halbzeug Material
Bear. Datum Name
Gepr. 00.00.06 Name
Norm 00.00.06 Name
Pin Halter D9mm
Blatt .
. Bl.
Zust Änderung Datum Nam. Urspr.
(Ers.f.:) (Ers.d.:) A4

Table 13: Factor levels, combination and results of FFD for reference low-carbon steel – all samples are welded

Diameter:	9 mm	Forge Pressure:	200 MPa	Material:	Low-Carbon Steel
Cross-section:	63 mm^2	Forge Time:	10 s		
Friction Pressure	Friction Time	Rotational Speed		Upset	Max. Upset-Rate
40 MPa	2 sec	1250 rpm		1.08 mm	11.26 mm/s
40 MPa	2 sec	1750 rpm		8.44 mm	27.67 mm/s
60 MPa	2 sec	1250 rpm		2.14 mm	10.93 mm/s
60 MPa	2 sec	1750 rpm		12.81 mm	29.93 mm/s
40 MPa	2.5 sec	1250 rpm		1.36 mm	11.92 mm/s
40 MPa	2.5 sec	1750 rpm		5.54 mm	20.01 mm/s
60 MPa	2.5 sec	1250 rpm		5.69 mm	23.01 mm/s
60 MPa	2.5 sec	1750 rpm		13.54 mm	30.89 mm/s

```
MTS Systems ISTIR Weld Data
================================================================================
Settings File : C:\Projects\3DOF_FSW\settings\Settings_Default.set
Tool Type     : Adjustable Tool
Tool Length   : 135.0
Pin OFfset    : 0.0
================================================================================
Part Coordinate Transform  :
   X, Y, Z Offset          : 362.624, 156.9368, -159.26
   Rz, Ry, Rx Rotation     : 0.0, 0.0, 0.0
Table Coordinate Transform :
   X, Y, Z Offset          : 0.0, 0.0, 0.0
   Rz, Ry, Rx Rotation     : 0.0, 0.0, 0.0
Table Mode                 : Disabled
Cylinder Diameter          : 125.0 mm
================================================================================
Operator           : Maintenance
================================================================================
DAQ File      : C:\Projects\3DOF_FSW\settings\DefaultDaqSignals.sig
Tuning        : C:\Projects\3DOF_FSW\settings\Tuning_no_pin.srv
Calibration   : C:\Projects\3DOF_FSW\settings\Calibration_Default.cal
================================================================================
Post Weld Comments :
================================================================================
Weld Program Listing:

COORDS/PART

FEEDRATE/RATE,2000,ACCEL,2000
GOTO/0.0,0.0,20.0
FORGEMOVE/POSITION,8.0,RATE,500,ACCEL,500
DELAY/SEC,1.0
FEEDRATE/RATE,1000,ACCEL,2000

GOTO/0.0,0.0,0.0

FORGEMOVE/TOUCH,0,FORCE,0.5,RATE,12,ACCEL,100
DELAY/SEC,0.1
FORGEMOVE/POSITION,0.2,RATE,6,ACCEL,6,RELATIVE
DELAY/SEC,0.1

SPINDLE/RPM,500,ACCEL,1500
DELAY/SEC,2.0
FORGEMOVE/POSITION,-0.15,RATE,10,ACCEL,10,RELATIVE
DELAY/SEC,0.1
FORGECONTROL/FORCE,0.1
DELAY/SEC,3.0
SPINDLE/RPM,2750,ACCEL,1500

FORGECONTROL/FORCE,0.15
DELAY/SEC,10.0
FORGECONTROL/FORCE,0.25
DELAY/SEC,10.0
FORGECONTROL/FORCE,0.35
DELAY/SEC,10.0
FORGECONTROL/FORCE,0.45
DELAY/SEC,10.0
FORGECONTROL/FORCE,0.55
DELAY/SEC,15.0

FORGECONTROL/FORCE,7.0
DELAY/SEC,0.80
SPINDLE/RPM,0,ACCEL,4000
FORGECONTROL/FORCE,12.5,RATE,7.5,ACCEL,10.0
DELAY/SEC,10.0

FORGECONTROL/FORCE,2.0,RATE,7.5,ACCEL,10.0
DELAY/SEC,30.0
FORGECONTROL/FORCE,0,RATE,7.5,ACCEL,10.0
DELAY/SEC,10.0
```